UNIVERSITY OF SOUTHAMPTON

FACULTY OF ENGINEERING AND THE ENVIRONMENT

Engineering Sciences

Revealing the Heterogeneity in Weld Microstructures Using the Thermomechanical Dissipative Heat Source

by

Palaniappan Jaya Seelan

Thesis for the degree of Doctor of Philosophy

May 2018

UNIVERSITY OF SOUTHAMPTON

ABSTRACT

FACULTY OF ENGINEERING AND THE ENVIRONMENT

Engineering Materials

Thesis for the degree of Doctor of Philosophy

REVEALING THE HETEROGENEITY IN WELD MICROSTRUCTURES USING THE THERMOMECHANICAL DISSIPATIVE HEAT SOURCE

Palaniappan Jaya Seelan

Mechanical deformation of a metal is accompanied by the dissipation of energy in the form of heat as a result of thermodynamically irreversible processes occurring at the microscale. This is applicable to deformation in both elastic and plastic regime so long as the thermodynamically irreversible processes are activated. It follows that there is a possibility of identifying the condition of the material microstructure by evaluating the heat dissipated during deformation. In the thesis, the continuous temperature rise due to the heat dissipation in a material under cyclic loading is obtained using an infrared (IR) detector. Most metals dissipate a very small amount of heat in their elastic range (few $mK.s^{-1}$). As a consequence, the temperature change is usually below the thermal resolution of the infrared detector used. To enable an accurate measurement to be made, the experiments were conducted in a specially designed setup which eliminated parasitic heat sources.

Spatial averaging was used to improve the signal to noise ratio and the dissipative heat source was extracted from the thermal data using the thermomechanical heat diffusion equation. The spatial averaging technique successfully provided a consistent detection threshold of just under 1 $mK.s^{-1}$. To demonstrate the effectiveness of the enhanced thermal resolution, the effect of material microstructure on the dissipative heat source was studied in 316L stainless steel. Different microstructures were produced by heat treating strip specimens to give a homogeneous field of observation over a large area of the IR detector. Monotonic tensile test and microhardness test were performed on each of the specimen to establish the change in properties resulting from the different microstructures. Micrographs were produced, which showed that the grain size only increased at the highest temperature, for the other heat treatment any difference in the dissipation would be mostly as a result of change in dislocation density. At equivalent stress levels, the microstructure had a significant effect on the dissipative heat source.

In the vicinity of welds, material microstructures are inhomogeneous over relatively small areas. To capture possible spatial heterogeneities in the heat source, a 3D (2D in space and time) least square

estimation of the temperature evolution was performed in place of the spatial averaging technique. The temperature data were fitted over a small window which is swept throughout the entire data set resulting in a spatial map of the dissipative heat source. The method was verified using a 'hole-in-plate' specimen under tensile cyclic loading which has an inhomogeneous stress field and hence dissipation. The approach was then used on the data collected from a welded 316L specimen exhibiting an inhomogeneous microstructure but tested in nominally uniaxial stress. It was shown that the region corresponding to the base metal had the highest dissipation followed by a gradual decrease in the heat source across the heat affected zone. The heat source increases subsequently as the centre of the fusion zone is approached. A modified procedure employing higher spatial resolution focusing on the fusion zone also revealed differences in the heat source between different weld passes. Strain measurements made on identical specimens using digital image correlation verified the material properties local to the weld. The work in the thesis clearly demonstrates that the dissipative heat sources associated with microstructural behaviour in welds can be identified successfully using IR thermography.

Table of Contents

Table of Tables

Table of Figures

Table of Figures

Table of Figures

Table of Figures

Academic Thesis: Declaration of Authorship

I, Palaniappan Jaya Seelan, declare that this thesis and the work presented in it are my own and has been generated by me as the result of my own original research.

Revealing the Heterogeneity in Weld Microstructures Using the Thermomechanical Dissipative Heat Source

I confirm that:

1. This work was done wholly or mainly while in candidature for a research degree at this University;
2. Where any part of this thesis has previously been submitted for a degree or any other qualification at this University or any other institution, this has been clearly stated;
3. Where I have consulted the published work of others, this is always clearly attributed;
4. Where I have quoted from the work of others, the source is always given. With the exception of such quotations, this thesis is entirely my own work;
5. I have acknowledged all main sources of help;
6. Where the thesis is based on work done by myself jointly with others, I have made clear exactly what was done by others and what I have contributed myself;
7. Part of this work has been published as: Please see List of Conference Papers

Signed: .....

Date: ...……

List of Conference Papers

[1] Seelan, P.J., Dulieu-Barton, J.M., and Pierron, F. “The effect of microstructure on energy dissipation in 316L stainless steel", In *Residual Stress, Thermomechanics & Infrared Imaging, Hybrid Techniques and Inverse Problems, Volume 9*, pp. 15-19. Springer International Publishing, 2017. (Also Proc. SEM XIII International Congress, Orlando, June 2016).

[2] Seelan, P.J., Dulieu-Barton, J.M., and Pierron, F. “The effect of microstructure on the dissipative heat source in 316L stainless steel”, 16th international conference on experimental mechanics, Sheffield, UK, 2017.

[3] Seelan, P.J., Dulieu-Barton, J.M., and Pierron, F. “Dissipative heat source distribution in a laser welded 316 L stainless steel”, Society for experimental mechanics conference, Greenville, SC, USA, 2018.

Acknowledgements

First and foremost I am extremely grateful to my supervisors, Professor Janice Barton and Professor Fabrice Pierron for giving me the opportunity to study for a PhD. I wish to thank them for their guidance, encouragement and support throughout the project. I am also very appreciative to Dr. Rian Seghir for lending me his expertise through many insightful discussions and suggestions about the project.

The experiments conducted in this work wouldn't have been possible without the help and advice of Dr. Andy Robinson who was always ready to assist. I would also like to acknowledge Dr. Wendell Bailey for his assistance in carrying out the heat treatments presented in Chapter 5. Thanks also goes to Dr. Nicholas O'Meara (formerly TWI) for his assistance in manufacturing the welded specimens at TWI, Dr. Geoff Howell, Dr. Elise Chevallier, Dr. Rachael Tighe, as well as to other RESIST project partners.

Special thanks to Dr. James Thatcher, Geir Olafsson, Irene Jiménez Fortunato, and to the rest of my colleagues for making this PhD experience enjoyable.

A big thanks to my family for their love and unfaltering support particularly during the time of this project.

Finally, I would like to acknowledge Innovate UK for funding the PhD.

Notations

Symbol	Meaning
Upper Case Roman Symbols	
B	Stefan-Boltzmann constant
C	Specific heat capacity at constant pressure
E	Young's modulus
E_k	Kinetic energy
$\dot{E}_k$	Rate of change of kinetic energy
K	Thermoelastic constant
N	Frame number
Q	Rate of heat transferred to the system
R	Radiant emittance
R_σ	Load ratio
S	Thermomechanical source
$\overline{S}$	Thermomechanical source averaged in x direction
$\overline{\overline{S}}$	Thermomechanical source averaged in x and y direction
$\overline{\overline{S}}_{conduction}$	Thermomechanical source due to conduction
$\overline{\overline{S_D}}$	Dissipative heat source averaged in the x and y direction
$\overline{\overline{S_{TE}}}$	Thermoelastic source averaged in the x and y direction
T	Temperature
T_{en}	The air temperature in contact with the specimen
T_{enrej}	The air temperature in contact with the reference specimen
T_m	Mean temperature
T_{ref}	Surface temperature of the reference specimen
T_0	Initial temperature
$\dot{T}$	Rate of change of temperature
U	Internal energy
$\dot{U}$	Rate of change of internal energy
W_{int}	Work done by internal forces
W_{ext}	Work done by external forces
Lower Case Roman Symbols	
b	Width of the specimen
c	Speed of light
d	Thickness of the specimen
e	Emissivity
g	Rate of heat generated per unit volume
h	Convective heat transfer coefficient
h_p	Planck's constant
k	Thermal conductivity
k_B	Boltzmann's constant.
l	Length of the gauge section
n	Smoothing window parameter
$\vec{n}$	Unit vector normal to the boundary
$\vec{q}$	Heat flux vector
r	External radiative source

$\bar{r}$	External radiative source averaged in *x* direction
$\bar{\bar{r}}$	External radiative source averaged in *x* and *y* direction
s	Specific entropy
t	Time
u	Specific internal energy
v	Poisson's ratio

Lower Case Greek Symbols	
α	Coefficient of thermal expansion
α_j	Internal state variable
ε	Strain
$\dot{\varepsilon}$	Rate of change of strain
f	Loading frequency
λ	Wavelength
θ	Temperature change
$\bar{\theta}$	Temperature change averaged in x direction
$\bar{\bar{\theta}}$	Overall temperature variation (spatially averaged)
$\tilde{\theta}$	Overall temperature variation (image processing)
$\bar{\bar{\theta}}_{TE}$	Thermoelastic temperature variation
$\bar{\bar{\theta}}_{D}$	Dissipative temperature rise
ρ	Density
σ	Applied stress
σ_m	Mean stress
$\sigma_{\max}$	Maximum stress
$\sigma_{\min}$	Minimum stress
σ_{kk}	First stress invariant
σ_x, σ_y	Normal stress in the *x*-direction and *y*-direction respectively
σ_{ij}	Stress tensor
σ_a	Stress amplitude
τ	Time constant for total heat exchange
$\tau_{convection}$	Convective heat exchange time constant
$\tau_{radiation}$	Radiative heat exchange time constant
$\vec{\upsilon}$	Velocity
ω	Loading frequency (angular)
ψ	Specific free energy

Subscripts	
spec	Specimen
ref	Reference specimen
t = 0	At time *t = 0*

1 Introduction

1.1 Background and Motivation

This PhD is part of an Innovate UK project entitled, 'Residual Stress and Structural Integrity Studies using Thermography (RESIST)'. The project completed in March 2017 and was successful in developing Thermoelastic Stress Analysis (TSA) [1] as a stress based non-destructive evaluation (NDE) tool for onsite use in the energy production industry [2]. RESIST also focused on developing TSA as a residual stress evaluation tool, which was the object of two other PhD projects [3, 4]. In [3], it was shown that TSA could identify regions of welding induced plastic strain and demonstrated the potential of TSA to be used as a bases for establishing residual stresses. In [4], it was shown that the thermoelastic response was sensitive to plastic straining and material microstructure. In the present PhD, the idea of using the dissipative heat source [5, 6] to identify microstructural changes in the vicinity of welds is explored. In essence, the distinct contribution of the PhD to the RESIST project is to extend the scope of using thermography for non-destructive assessment of materials further to microstructures. It shares common ground with the RESIST project in terms of the excitation and measurement technique used – cyclic loading and infrared thermography respectively. Also common is the material investigated – the 316L stainless steel. This is because of the widespread usage of the material in the energy production industry due to its excellent corrosion and creep resistance at relatively high temperatures.

It has long been recognized that a part of the mechanical work done on a material during deformation is converted to heat. The heat generated then causes the temperature of the material to increase. This phenomena was first observed by Farren and Taylor [7] in a material undergoing plastic deformation. While it is usually perceived to be a consequence of plasticity, this phenomena occurs even in the elastic range. Such behaviour is explained by the fact that dissipation originates from thermodynamically irreversible processes occurring at the microscale, which are activated only after a certain stress threshold. While it is difficult to determine the exact applied stress this threshold translates to, it is less than the macroscopic yield stress. As such, there is a possibility of utilizing heat dissipated by a material subjected to deformation to assess its own microstructural state – i.e. a non-destructive microstructural assessment tool.

As the heat source cannot be measured directly, the temperature rise due to heat source has to be measured to evaluate the heat source. Modern infrared (IR) cameras provide an accurate non-contact way to measure temperature variations. However, unlike plastic deformation, the temperature rise due to a single step of elastic loading is much lower than the thermal resolution of the infrared detectors. Hence, cyclic loading is required to generate continuous heat dissipation that leads to measurable temperature rise. The cyclic loading also leads to cyclic temperature variation in

conjunction with the dissipative temperature rise due to the thermoelastic effect [8], which has been developed into a well understood stress analysis technique known as Thermoelastic Stress Analysis (TSA) [1]. The thermoelastic response is not dissipative in nature as it results from the coupling between the mechanical and the thermal state of the material. Therefore, to identify the dissipative temperature rise it is necessary to eliminate the cyclic temperature variation resulting from the thermoelastic effect.

Assessing the material behaviour in the form of temperature rise is inaccurate since it is affected by heat exchanges between the specimen and the environment. A better approach is to derive the dissipative heat source from the temperature measurement using the thermomechanical heat diffusion equation [9]:

$$\rho C \frac{\partial \theta}{\partial t} - k\nabla^2\theta + \rho C \frac{\theta}{\tau} = S_D + S_{TE} \qquad 1.1$$

where S_D is the dissipative heat source, S_{TE} is the thermoelastic heat source [8], ρ is the material density, C is the specific heat, t is time, k is the thermal conductivity, ∇^2 is the Laplacian operator, θ is the local temperature change of the specimen due to the thermomechanical heat sources, and τ is a time constant characterizing the convection and radiation losses [10].

Using Equation 1.1 ensures that the effects of conductive, convective, and radiative heat transfer between the material and its environment can be taken into account. Additionally, if the temperature measurement is obtained using an infrared camera, the full-field, spatially and temporally rich data can be exploited in data processing to accurately determine the small temperature change associated with the dissipation. Most importantly, and the purpose of the PhD, is that the full-field nature of the infrared images provides the opportunity to identify any heterogeneity in the heat source resulting from microstructural changes over the region of interest.

In the RESIST project the main interest was in the structural integrity of welded structures such as the joints in piping systems used in power plants. The welding process uses high intensity heat sources to join parts together. The region that melts and solidifies is known as the fusion zone (FZ), where a range of different microstructures can form [11]. The heat that diffuses away from FZ does not melt the material, but rather modifies the material microstructure and this region is known as the heat affected zone (HAZ). Therefore, in the vicinity of the weldment, at least three types of microstructure can be observed: the unaffected base material (parent material), the HAZ, and the FZ (see Figure 1.1). Thus, the region close to a weld provides a particularly interesting structure to develop the idea of using the dissipative source to identify microstructural changes as these could provide an indication of the integrity of the weld and the technique could be used to assess different welding parameters and new processes.

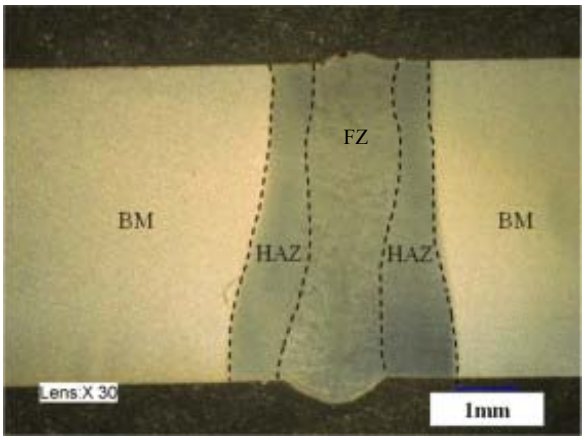

Figure 1.1 A macrograph section through the laser butt weld in 6 mm thick SA508 steel [12].

1.2 Aim and objectives

The aim of the PhD is to **identify the heterogeneity in microstructure in regions close to a weld using the dissipative heat source.** The most significant challenge in achieving the aim stems from the fact that the temperature change resulting from the dissipation is very small. Therefore, to achieve the aim and overcome the challenges, the following objectives must be addressed:

1. Devise an experimental procedure so that the temperature data collected by the infrared camera is unaffected by parasitic heat sources such as external radiation.
2. Use the thermomechanical equation (Equation 1.1) as the basis for deriving the dissipative heat source by developing and implementing a data processing procedure for the temperature measurements obtained from the IR camera by:
    a. using spatial averaging to extract the dissipative heat source
    b. devising an image processing approach based on spatio-temporal least square fitting that resolves the full-field dissipative heat source
3. Use heat treatments to create a set of specimens with known microstructures and demonstrate that the dissipative heat source is dependent on the microstructure using the procedure developed in 2 (a).
4. Develop a modified experimental procedure that allows imaging at higher spatial resolution.
5. Establish confidence in the ability of the procedure developed in 2 (b) to capture spatial heterogeneities in the heat source at high spatial resolution using a specimen with a non-uniform stress field that provides heterogeneities in the heat source.
6. Demonstrate that the verified procedure developed in 2 (b) can identify the different microstructures resulting from welding.

1.3 Novelty

The calculation of the heat source from temperature measurement using infrared thermography was introduced through the pioneering work of Chrysochoos and Dupre [9]. Since then, the dissipative heat source has been primarily used to investigate the fatigue behaviour of materials. However, no study has investigated the effect of different microstructure on the dissipative heat source. As such, for the first time in the current PhD, the dissipative heat source has been assessed with the intention of characterise the material microstructure. The focus of the current work is predominantly on the dissipation resulting from elastic cyclic loading since microstructural changes do not occur in this loading regime. The tests performed are also much shorter in duration compared to fatigue tests where the material microstructure changes as a result of the accumulation of fatigue damage.

Under the circumstances, the intensity of the heat source is low. Even with the relatively high thermal resolution of the current infrared detectors, measuring this small temperature rise poses a significant challenge. Building on the methodology proposed by Maquin and Pierron [13] to identify very small heat sources based on the novel use of a reference specimen to account for the fluctuation in environmental temperature and the spatial averaging method to increase the signal to noise ratio, a refined experimental procedure is developed for use in the present PhD. In particular, a chamber is specially designed to shield the specimen from parasitic heat sources that is both robust and easy to mount on the test machine. The spatially averaged data processing routine of [13] is adapted and implemented. It is confirmed that a very low detection threshold can be achieved using this methodology.

The procedure developed based on [13] requires that the specimen is homogeneous. This is used to investigate the link between microstructure and the energy dissipated, the novelty being that strip specimens with homogeneous microstructures were generated by a distinct heat treatment procedure. A range of heat treatments is specifically developed to modify the material microstructure, dislocation density in particular, as opposed to common heat treatment procedures that hardens a material or relieves residual stress. The results from this work show categorically that the dissipative source can be used to identify changes in microstructure.

The next step is the examination of the full-field distribution of the dissipative heat source in the vicinity of a weld joint. Although a few self-heating studies of welds exist in the literature [14-16], the current work is the first to identify the dissipative heat source distribution local to the weld. As such, this can be regarded as the main novelty of the PhD. To achieve this, the experimental procedure was modified so that it was able to image at high resolution while eliminating parasitic heat sources using the protective chamber. Additionally, the calculation of the full-field dissipative heat source required a dedicated image processing procedure as the spatial averaging method used in [13] was insufficient to identify the heat sources in a non-homogeneous field. Therefore an image

processing method proposed by Berthel *et al*. [17] was incorporated into the methodology developed in [13].

Other work on self-heating studies of weldments [14, 18, 19] has examined the temperature rise in the weld by imaging the welded surface during fatigue loading. This was sufficient considering that the aim of these works was to identify the fatigue limit of the weld. In this work, test specimens have been designed so that it is possible to image the cross section of the weld. This involves careful cutting through the weld, but allows access to the different microstructures in the vicinity of the weld. The specimen configuration has enabled the novel work, which demonstrates that the heat source can distinguish the major regions (base metal, heat affected zone, and fusion zone) and by using the high resolution imaging regions within the fusion zone of the multi-pass weld.

1.4 Overview of report

Chapter 2 presents the literature review on the thermal effects resulting from the application of mechanical loading to a material. The thermomechanical framework used to derive the heat diffusion equation is first presented. The adaptation of this framework that enables it to be applied to experiments is then presented. Subsequently, the two different heat sources activated by mechanical deformation are described: the thermoelastic source and dissipative source. The thermoelastic heat source is briefly discussed, after which a detailed review of the dissipative heat source is presented.

Chapter 3 begins with the introduction to infrared radiation which is used by an infrared detector (camera) to measure temperature. The calibration approach used in the PhD to convert infrared radiation to temperature values is then detailed. Subsequently, the thermal resolution of the infrared detector is re-examined, using a black body source. The challenges involved in measuring a very small temperature change are discussed. Then, the experimental setup is introduced where the design of the chamber, control of the test machine, and data acquisition parameters are detailed (Objective 1).

Chapter 4 begins with describing data processing methods based on the heat diffusion equation used in previous work [13] (Objective 2a), which is refined and implemented independently in the PhD. In the next section, the procedure involved in determining the detection threshold of the test set-up and processing approach is detailed. The chapter concludes with an evaluation of the heat sources, which are used to establish the detection threshold of the experimental set-up and the processing procedure.

In Chapter 5, a study is carried out to investigate the link between microstructure and energy dissipation which is intended to serve as a feasibility study of the evaluation of the full-field dissipative heat source in welds. The heat treatments undertaken (Objective 3) to realise different microstructures are detailed. The mechanical properties and micrographs of the resulting specimens

are also presented. After that, the outcome of the investigation into the effect of microstructure on energy dissipation is presented. The evolution of the heat source and plastic work obtained from simultaneous strain measurement during cyclic hardening is presented for the different microstructures.

Chapter 6 presents the new image processing procedure required to obtain the full-field dissipative sources in the weld (Objective 2b). A brief overview of the fundamentals of the spatio-temporal averaging technique that allows the calculation of both the full-field thermoelastic and dissipative source is given. After that, a study is carried out to determine the optimal parameters that offer the best compromise between spatial resolution and noise. The capability of this technique in capturing spatial heterogeneity was verified by studying the full-field dissipative heat source of a 'hole-in-plate' specimen where the inhomogeneous stress distribution leads to heterogeneity in the dissipation (Objectives 4 & 5).

Having established confidence in the image processing method, Chapter 7 explores the full-field dissipation in the vicinity of a weld (Objective 6). The design of the welded specimen and the mechanical properties and the microstructure of similarly produced weldments are discussed. The dissipative heat source distribution of the weld joint is then examined at different stress levels. Material properties local to the weld, obtained from strain measurement using digital image correlation are used to verify these results. Additionally, high resolution thermography (Objective 4) is employed to examine the fusion zone, the main region of interest, and then compared with micrographs of the weld region.

Chapter 8 provides the overall conclusion of the thesis and outlines the future work that could be undertaken.

2 Literature review: the thermomechanics of materials

2.1 Introduction

Mechanical deformation of material is usually accompanied by a temperature change. In particular, cyclic loading activates two different heat sources: (i) the thermoelastic source which is the result of thermomechanical coupling and (ii) the dissipative source which is the result of thermodynamically irreversible phenomena at the microscale such as movement of dislocations. The next section demonstrates that by using the thermodynamics of an irreversible process [9], the thermomechanical framework can be derived. The starting point is the first and second laws of thermodynamics, with a view to demonstrate that if the application of a mechanical load is included, the heat sources are activated. It is worth noting that the thermoelastic source is a few orders of magnitude larger than the dissipative heat source [20]. The following section describes the thermoelastic source and how this is used by the other two PhD projects in the RESIST project and justifies the alternative investigation of the dissipative source as the object of the present PhD. Therefore, the fourth section (Section 2.4) in the review describes in detail the nature of the dissipative source. It is demonstrated, with examples from previous works as to why analysing the dissipative temperature rise alone is less suited when it comes to characterising the microstructure. As such, an adaptation of the thermomechanical framework that allows the experimentally measured temperature rise to be converted to heat source is presented. The penultimate section describes attempts to capture different phenomena in a range of material types using the dissipative heat source. No cases are reported where the microstructural heterogeneity in a weld is studied.

2.2 Basic thermomechanical constitutive relationship

The principle of conservation of energy states that energy cannot be created nor destroyed but can only be transferred from one form to another. The first law of thermodynamics for a body with finite volume Ω and boundary $\partial\Omega$ is:

$$\frac{d}{dt}\left(U + E_k\right) = W_{ext} + Q \tag{2.1}$$

where

- U is the internal energy given by $U = \int_{\Omega} \rho u d\Omega$, u is the specific internal energy per unit mass and ρ is the density.

- E_k is the kinetic energy given by $E_k = \frac{1}{2}\int_{\Omega} \rho \vec{\upsilon} \cdot \vec{\upsilon} d\Omega$, $\vec{\upsilon}$ is the velocity
- W_{ext} is the work of the external forces
- Q is rate of heat transferred to the system given by $Q = \int_{\Omega} r d\Omega - \int_{\partial\Omega} \vec{q} \cdot \vec{n} d(\partial\Omega)$, r is the rate of heat generated per unit volume, $\vec{q}$ is the heat flux vector and $\vec{n}$ is the unit vector normal to the boundary, $\partial\Omega$.

The work - energy theorem states that the net force is transformed into the kinetic energy of the body:

$$\frac{d}{dt} E_k = \dot{E}_k = W_{ext} + W_{\text{int}} \tag{2.2}$$

where W_{int} is the actual work done by the internal forces. By eliminating W_{ext} and $\dot{E}_k$ in Equation 2.1 by using Equation 2.2 results in:

$$-W_{\text{int}} + Q = \dot{U} \tag{2.3}$$

Given that:

$$W_{\text{int}} = -\sigma : \dot{\varepsilon} \tag{2.4}$$

where σ is stress and $\dot{\varepsilon}$is the strain rate, the local form of the principle of conservation of energy can then be expressed as:

$$\rho \frac{du}{dt} = \sigma : \dot{\varepsilon} + r - div(\vec{q}) \tag{2.5}$$

The second law of thermodynamics states that the rate of entropy production is always greater than or equal to the rate of heating divided by the temperature, T [21]. This can be expressed as:

$$\rho \frac{ds}{dt} - \frac{r}{T} + div\left(\frac{\vec{q}}{T}\right) \geq 0 \tag{2.6}$$

where s is specific entropy. Substituting the expression for r from Equation 2.5 to Equation 2.6 eliminates r from Equation 2.6. Noting that $div\left(\frac{\vec{q}}{T}\right) = \frac{div\,\vec{q}}{T} - \frac{\vec{q} \cdot gradT}{T^2}$, this results in the local expression of the second law:

$$\rho\left(T\frac{ds}{dt} - \frac{du}{dt}\right) + \sigma : \dot{\varepsilon} - \frac{\vec{q}}{T} \cdot grad\left(T\right) \geq 0 \tag{2.7}$$

The specific free energy, ψ function is defined as:

$$\psi = u - Ts \ , \psi = \psi(T, \alpha_j) \tag{2.8}$$

where α_j , $j = (1,2,...,n)$ is an internal state variable. By noting that:

$$s = -\frac{\partial \psi}{\partial T} \tag{2.9}$$

and

$$\frac{d\psi}{dT} = \frac{\partial \psi}{\partial T}\dot{T} + \frac{\partial \psi}{\dot{\alpha}_j}\dot{\alpha}_j \ , \ j = (1,2,...,n) \tag{2.10}$$

where $\dot{T}$ and $\dot{\alpha}_j$ are the rate of change of temperature and internal state variable respectively, the Clausius-Duhem inequality is obtained from Equation 2.7:

$$-\rho \frac{\partial \psi}{\partial \alpha_j}\dot{\alpha}_j + \sigma : \dot{\varepsilon} - \frac{\vec{q}}{T} \cdot grad(T) \geq 0 \ , \ j = (1,2,...,n) \tag{2.11}$$

Given that u can be expressed as a function of ψ , T and s (Equation 2.8), and by using Equations 2.9 and 2.10, the expression for $\frac{du}{dt}$ can be obtained as follows:

$$\begin{aligned} \frac{du}{dt} &= \frac{d\psi}{dT} + T\frac{ds}{dt} + s\dot{T} \\ \frac{du}{dt} &= \frac{\partial \psi}{\partial T}\dot{T} + \frac{\partial \psi}{\partial \dot{\alpha}_j}\dot{\alpha}_j + T\left(\frac{\partial s}{\partial T}\dot{T} + \frac{\partial s}{\partial \dot{\alpha}_j}\dot{\alpha}_j\right) - \frac{\partial \psi}{\partial T}\dot{T} \\ \frac{du}{dt} &= \frac{\partial \psi}{\partial \dot{\alpha}_j}\dot{\alpha}_j - T\left(\frac{\partial^2 \psi}{\partial T^2}\dot{T} + \frac{\partial^2 \psi}{\partial \dot{\alpha}_j \partial T}\dot{\alpha}_j\right) \end{aligned} \tag{2.12}$$

Substituting the expression for $\frac{du}{dt}$ in the equation above to Equation 2.5 then results in:

$$\rho \frac{\partial u}{\partial t} = \rho \frac{\partial \psi}{\partial \alpha_j}\dot{\alpha}_j - \rho\left(T\frac{\partial^2 \psi}{\partial T^2}\dot{T} + \frac{\partial^2 \psi}{\partial \alpha_j \partial T}\dot{\alpha}_j\right) = \sigma : \dot{\varepsilon} + r - div(\vec{q}) \tag{2.13}$$

As $C = -T\frac{\partial^2 \psi}{\partial T^2}$, the energy balance results in:

$$\rho C\dot{T} + div\vec{q} = \left(\sigma : \dot{\varepsilon} + \rho T\frac{\partial^2 \psi}{\partial T \partial \alpha_j}\dot{\alpha}_j - \rho\frac{\partial \ \psi}{\partial \alpha_j}\dot{\alpha}_j\right) + r \tag{2.14}$$

The first term on the left represents the heat energy that causes the temperature rise and the second term on the left represents the heat that is lost by conduction. The $\rho T\frac{\partial^2 \psi}{\partial T \partial \alpha_j}\dot{\alpha}_j$ term on the right represents the thermomechanical term. It leads to different terms depending on the choice of internal

state variable, i.e. when $\alpha_j = \varepsilon^e$ (elastic strain), this results in the thermoelastic coupling $\rho T \frac{\partial^2 \psi}{\partial T \partial \varepsilon^e} \varepsilon^e$. The intrinsic dissipation is the difference between the mechanical work done, $\sigma : \dot{\varepsilon}$ and the stored energy, $\rho \frac{\partial \psi}{\partial \alpha_j} \dot{\alpha}_j$. The thermoelastic coupling leads to the thermoelastic source whereas the intrinsic dissipation leads to the dissipative heat source. These sources are described in further detail in the sections below. In particular, Section 2.4.2 details how the framework derived here is adapted to give the thermomechanical heat diffusion equation that allows the dissipative heat source to be calculated.

2.3 Thermoelastic Source

The thermoelastic coupling or thermoelastic effect was established by Lord Kelvin in the 1850s [22]. This is used as the basis of thermoelastic stress analysis (TSA). When a material is cyclically loaded, a cyclic temperature variation can be observed on its surface due to the strain induced. The thermoelastic temperature response ΔT is related to the change in the sum of principal surface stresses, $\Delta(\sigma_1 + \sigma_2)$ through the following equation [8]:

$$\Delta T = -KT_m \Delta(\sigma_1 + \sigma_2) \qquad 2.15$$

where K is the thermoelastic constant, and K is given by $\frac{\alpha}{\rho C_p}$, α is the coefficient of linear thermal expansion, ρ is the mass density, and C_p is the specific heat at constant pressure and T_m is the mean temperature of the material.

Equation 2.15 implies that at a fixed stress amplitude the temperature change is independent of applied mean stress, σ_m. However, Belgen [23] noticed deviations from linearity in the thermoelastic response. He proposed that this dependence of thermoelastic constant on mean stress was due to the effects of specific heat and Poisson's ratio. Machin *et al.* [24] confirmed the mean stress dependence for both aluminium and titanium alloys. This led Wong [25] to include the temperature dependence of material properties in the revised 'higher order' equation:

$$\dot{T} = \frac{T_m}{\rho C_p}\left[-\left(\alpha + \left(\frac{v}{E^2}\frac{\partial E}{\partial T} - \frac{1}{E}\frac{\partial v}{\partial T} \right)\sigma_{kk} \right)\dot{\sigma}_{kk} + \left(\frac{(1+v)}{E^2}\frac{\partial E}{\partial T} - \frac{1}{E}\frac{\partial v}{\partial T} \right)\sigma_{ij}\dot{\sigma}_{ij} \right] \qquad 2.16$$

where $\dot{T}$ is the rate of change of temperature, E is the Young's modulus of the material, v is the Poisson's ratio, and σ_{kk} is the first stress invariant, and σ_{ij} is the stress tensor.

For uniaxial cyclic loads:

$$\sigma_{11} = \sigma_{kk} = \sigma_m + \delta\sigma \sin \omega t$$
$$\sigma_{22} = \sigma_{33} = \sigma_{12} = \sigma_{13} = \sigma_{23} = 0 \qquad 2.17$$

where $\delta\sigma$ is the stress amplitude and ω is the loading frequency. Substituting this to Equation 2.16 results in:

$$\rho C_p \frac{\dot{T}}{T_m} = -\left(\alpha - \frac{1}{E^2}\frac{\partial E}{\partial T}\sigma_m\right)\delta\sigma \sin\omega t - \frac{1}{4E^2}\frac{\partial E}{\partial T}(\delta\sigma)^2 \cos 2\omega t \qquad 2.18$$

It can be seen that the thermoelastic response consists of two harmonic responses. The response at the loading frequency, ω depends on the mean stress and stress amplitude. The response at twice the loading frequency, 2ω depends on the square of the stress amplitude. Considering only the first harmonic and comparing it with Equation 2.15, the thermoelastic parameter is given as:

$$K = \frac{1}{\rho C_p}\left(\alpha - \frac{1}{E^2}\frac{\partial E}{\partial T}\sigma_m\right) \qquad 2.19$$

This shows that the mean stress dependence of the thermoelastic parameter is actually due to the temperature dependence of the Young's modulus of the material. For most materials (particularly the 316L stainless steel used in this work), the $\frac{\partial E}{\partial T}$ value is small and as such the second harmonic term is also small as detailed in the following section.

2.3.1 Applications of Thermoelastic Stress Analysis (TSA)

Applications of TSA include stress analysis of crack tips [26], composite materials [27] and structures [28] . In addition to the information regarding the stress state, it is also possible to obtain the phase angle of the temperature signals with reference to the load signals obtained by the infrared camera system from the test machine simultaneously with the thermal data. The phase information could be used to identify non-linearities in material behaviour. With the exception of [29], there hasn't been any article in the literature that explores TSA of welds. It was found that in a continuous fatigue test, the phase data can be a reasonable measure to track the accumulation of the plastic damage in welds. However, significant research has been done to assess residual stress state using TSA.

A primary part of the RESIST project is to investigate if residual stresses can be derived from the thermoelastic response of a welded structure. Three approaches have been proposed to evaluate the residual stress using TSA. The first two approaches are based on the mean stress effect and the revised higher order theory. In the first approach, the first and second harmonic frequencies of the thermoelastic response are measured. Equation 2.18 can then be used to estimate the mean stress and applied stress from these responses. The residual stress can be calculated from the mean and applied stress. This was validated by Wong *et al.* [30] using aluminium specimens. The disadvantage of this

approach is that it is difficult to be applied in materials which does not show mean stress dependence like stainless steel [31]. Also $\frac{\partial E}{\partial T}$ values for many materials are not available in the literature. Measuring this quantity is also difficult as it is very small. Another complication is that the second harmonic response is usually very small (2% of first harmonic as reported by Gyekenyesi [32]) and hence difficult to be measured.

The second approach uses the uncalibrated detector response as a whole and relates it to the principal stress. The resulting thermoelastic response is expressed as a function of applied mean and residual stress multiplied by elastic constants. The residual stress can then be found by identifying the Y-intercept of the graphical representation of the function. One of the major disadvantages of this approach is that thermoelastic response must be recorded over a range of mean stress all with the same detector and in a temperature controlled environment [33].

In the RESIST project the focus is on 316L stainless steel, where the elastic constants have been shown to have a negligible temperature dependence around room temperature [31]. This means that there will be little change in the thermoelastic response with changes in the mean stress resulting from residual stresses. Therefore, the third approach is based on the fact that the presence of plastic deformation alters the thermoelastic constant [34]. Since plastic deformation is related to residual stress, the residual stress could be quantified provided the relationship between the thermoelastic constant and plastic deformation is known. The other 2 PhD projects being conducted as part of the RESIST project are investigating this approach as a means for identify residual stresses [3, 4].

While relevant to the other two PhD projects, the thermoelastic response of the material is not examined in the current thesis. However, as the thermoelastic temperature variation is always present under cyclic loading, it has to be discarded when calculating the dissipative heat source. An overview of the dissipative heat sources is provided in the following section where its applications, particularly those related to welds, are discussed.

2.4 Dissipative Heat Source

2.4.1 Overview

Under mechanical deformation, a portion of the input mechanical work is converted to heat i.e. the material dissipates (generates) heat. This is applicable to deformation in both the elastic and plastic regime. In the case of elastic regime, at a macroscopic standpoint, this arises from the deviation of the material behaviour from linear elasticity (Hooke's Law). As a result, there is a phase lag between applied stress and the resulting strain [35]. This viscoelastic behaviour results in hysteresis as

illustrated in Figure 2.1. The heat energy generated is represented by the area within the hysteresis loop.

Microstructurally, the physical processes responsible for this behaviour stems from thermodynamically irreversible processes. As this is a form of friction occurring at the microscale, these phenomena are also collectively referred to as internal friction. Examples include the movement of atoms [36], viscous grain boundary sliding [37], and dislocation motion [38]. In the case of the movement of atoms, it is a result of movement of atoms from their equilibrium position caused by local defects in the lattice [39]. Energy is released when the atom goes back to its equilibrium position. However, the more significant contribution to dissipation is widely believed to be that of dislocation motion [40], which requires a certain stress level to be exceeded to overcome obstacles such as the atomic lattice, dislocation network, grain boundaries, and other external obstacles [39]. In the case of an anchored dislocation in a single crystal, a critical shear stress in the shear plane (Peierls-Nabarro stress threshold [41, 42]) is required to set the dislocations in motion. It is worth noting that this threshold is exceeded before the conventional yield stress is reached. One such mechanism of dislocation movement in elastic cyclic loading is the oscillation of pinned dislocations. Dislocations can be thought of as a string pinned to point defects. When stressed, the string bows out oscillating under cyclic loading (Figure 2.2 (A)-(F)). The thermodynamic irreversibility here arises due to the fact that the path taken by these oscillations are not the same.

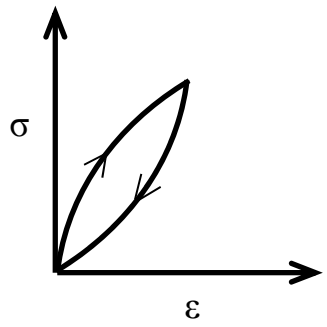

Figure 2.1 The stress strain response of a viscoelastic material that is loaded and unloaded forming a hysteresis loop.

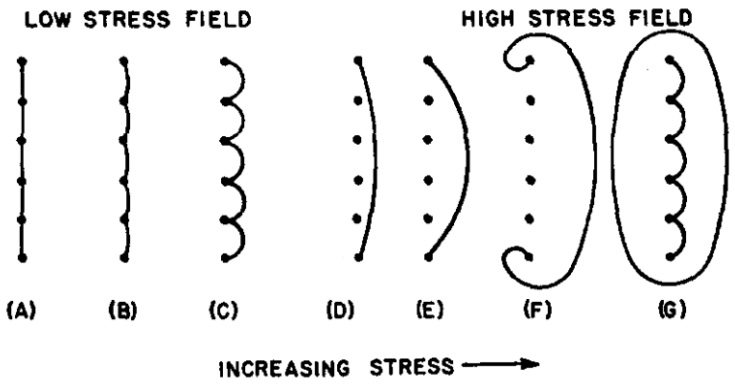

Figure 2.2 The bowing out of pinned dislocations at successively increasing applied stress from A to G [43].

When the stresses are increased further, new dislocations are created (Figure 2.2 (G)) which eventually leads to failure. The is due to the Frank Read mechanism [44] where dislocations multiply to allow slip to occur. In this mechanism, the applied stress causes the bowing of a dislocation pinned at two sites. As a result of the instability of the bowed dislocation, a new dislocation loop is formed and the original pinned dislocation is retained. The creation of new dislocations is generally associated to plasticity. Noting that this is not mechanically reversible, the thermodynamic irreversibility increases, hence the presumption is that in the presence of plasticity, dissipation is higher.

The heat energy generated due to dissipation causes the temperature of the material to increase. Some of the earlier work that documented the 'self-heating' phenomena under fatigue loading include that of Stromeyer [45] and Moore and Kommers [46]. The limitation in the thermal measurement equipment meant that the work was constrained to tools such as thermometer and thermocouples respectively. From then on there was this idea of correlating this temperature rise to endurance limit or fatigue limit of the material. The fatigue limit here is defined as the limiting value of stress at which failure occurs after an indefinitely large number of loading cycles. The advent of the infrared camera then brought about the examination of this phenomena at a more detailed level with the work of Charles *et al.* [47]. There was no further development in this field until the work of Luong [48]. It was only after that, that the estimation of the fatigue limit using the temperature evolution was attempted. Many including Luong [49], found that the temperature under fatigue loading evolved with a similar pattern (Figure 2.3), where the mean temperature of a material increases at the beginning and then reaches a plateau. The plateau temperature increases as the amplitude of applied load increases. For instance, La Rosa [50] used this as a basis to determine the fatigue limit of a material. Every applied stress amplitude has a corresponding plateau temperature. After a certain stress amplitude, the plateau does not exist anymore. A graph of stress amplitude against plateau temperature was plotted and the best fit line was extrapolated to zero to find the exact point where the plateau temperature ceases to exist. On the other hand, Luong [49] and later Cura [51] performed

separate set of tests for stress amplitudes above and below the expected fatigue limit. When these two data sets are plotted in the stress amplitude against plateau temperature graph they intersect at a point. This is identified as the fatigue limit. In spite of the success in identifying values of fatigue limit that matches the actual values from temperature measurements, it is the case that the link between microstructural changes that lead to fatigue failure and temperature evolutions is not fully understood [52].

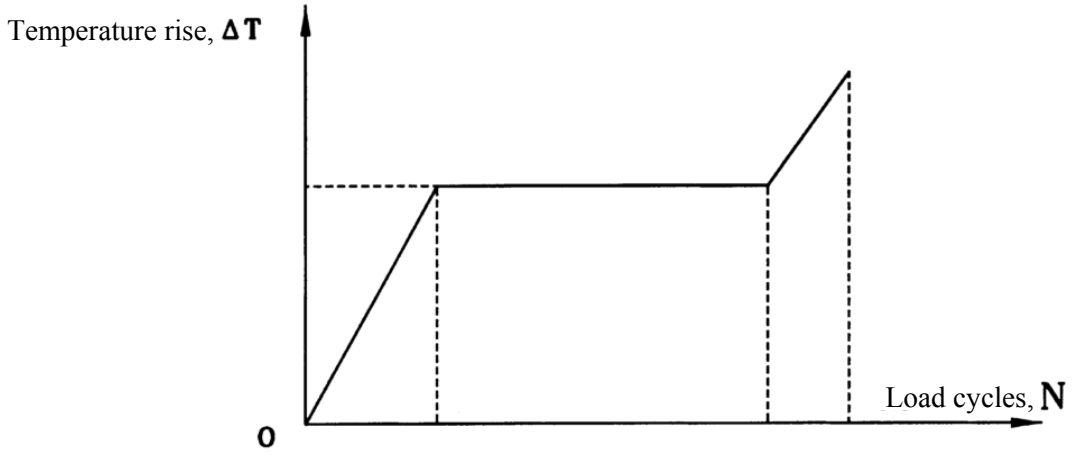

Figure 2.3 Temperature rise during a typical fatigue test against the number of load cycles [50].

The identification of the fatigue limit was also extended to heterogeneous materials such as welds. Self-heating phenomena in welds have been investigated by various researchers in the past [14-16]. One of the earliest studies by Crupi *et al.* [14] focused on identifying the fatigue limit of butt welded steel joints by using the rapid thermographic method established by Fargione *et al.* [50]. Crupi *et al.* [53] also conducted fatigue analysis on butt welded AH36 steel joints using the thermographic method. It was found that the thermographic method yielded a more conservative estimate of the S-N curve compared to the IIW (International Institute of Welding) Code. This was attributed to various different parameters (weld quality, welding technique etc.) that affect the strength of the welded structure that were not included in the code. Ummenhofer *et al.* [18], separated the linear and non-linear components of the temperature evolution during fatigue loading of welded joint. The non-linearities are thought to be caused by the energy dissipated. As a result, they were able to identify the existence and extension of plastic zones prior to crack initiation as well as the location and time of fatigue crack initiation in the weld toe.

The more recent investigation in this area was conducted by Calloch and co-workers on high cycle fatigue of lap welded [19] and seam welded [16] joints. In both cases the base material was ferrite-bainite phase steel in hot-rolled state whereas the welding process used was Gas Metal Arc Welding (GMAW). The weld joint in [16] is shown in Figure 2.4 (a) & (b). From the width averaged (1 D) temperature rise evolution observed under cyclic loading (see Figure 2.4 (c)), although no distinctive

regions were identifiable in the temperature field, some level of heterogeneity is present in that the temperature is highest at the weld centerline and gradually drops as the base metal is approached.

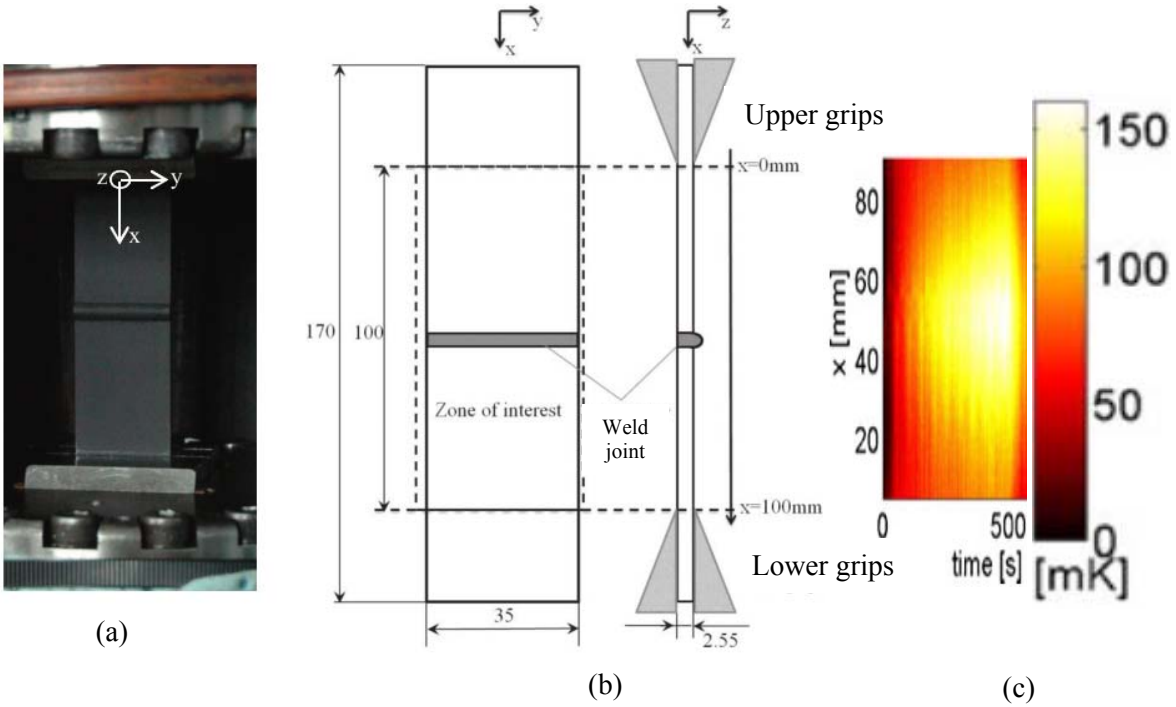

Figure 2.4 An example of a butt welded specimen: (a) clamped in a test machine (b) specimen dimensions (c) temperature rise observed under a maximum cyclic load of 10 kN at R_σ of 0.1 [16].

It can be seen that assessing microstructural changes from the temperature evolution alone is a significant challenge, as the evolution of the temperature of the specimen is not only affected by the microstructural heterogeneity but also by heat conduction within the specimen as well as heat exchanges with the surroundings. When compared to the evolution of the temperature alone, the heat source has the advantage of being intrinsic to the material behaviour. This is due to the fact that the dissipative heat source takes account of the heat exchanges through conduction, convection, and radiation. As such, it depends only on the stress amplitude and load ratio whereas the surface temperature could be affected by various factors such as specimen geometry and thermal boundary conditions [54]. Since this project explores the microstructural aspects of a weld, the extraction of the dissipative heat source from the temperature evolution has emerged as an approach to assess microstructural heterogeneity.

2.4.2 Obtaining the dissipative heat source from temperature measurement

Various approaches for calculating the dissipative heat source from the temperature rise exists in the literature [9, 17, 55], mostly developed to study the dissipative heat source over the entire fatigue life. However, these approaches are not suitable since the focus of this work is on the energy dissipated in the first few hundred load cycles. In particular, measurement of the small temperature rise during the first few hundred load cycles is a significant challenge in comparison to the extensive temperature rise over the entire fatigue life (refer Figure 2.3). As such, in the present PhD, the heat

sources are obtained using the refined methodology proposed by Maquin and Pierron [13] . In this approach, the heat diffusion equation was developed incorporating an additional reference specimen, made of the same material as the specimen, placed adjacent to the actual cyclically loaded specimen in the test. In addition to reducing the fluctuations in environmental temperature, the reference specimen also helps eliminate the effects of external radiation. This was possible due to the use of an insulation chamber designed to shield both the specimen and the reference specimen from parasitic heat sources that enables the assumption that the external radiative source is the same for both the specimen and the reference specimen. As demonstrated later in the following chapter, this then leads to the elimination of the radiative source term in the equation derived. Other assumptions that were made are as follows:

- Thermo-physical material properties are independent of temperature since the temperature variations are very low,
- The surface temperature is the average temperature across the thickness, so the specimen must be thin, enabling the application of the 2D heat diffusion equation (Equation 2.20),
- The heat transfer across the through-thickness side of the specimen is small and can be neglected.

The derivation of the equation is closely connected to the experimental setup. Hence, an illustration of the experimental setup is presented in Figure 2.5 to aid the derivation of the equation. The gauge section of the specimen and reference specimen within the insulation chamber are indicated by the red rectangle as shown in Figure 2.5. It should be noted that, in the actual setup (refer Chapter 3), the specimen extends all the way into the grips of the test machine where it is clamped. The formulation in [13] is presented in full detail here as this approach is used throughout the work described in the thesis.

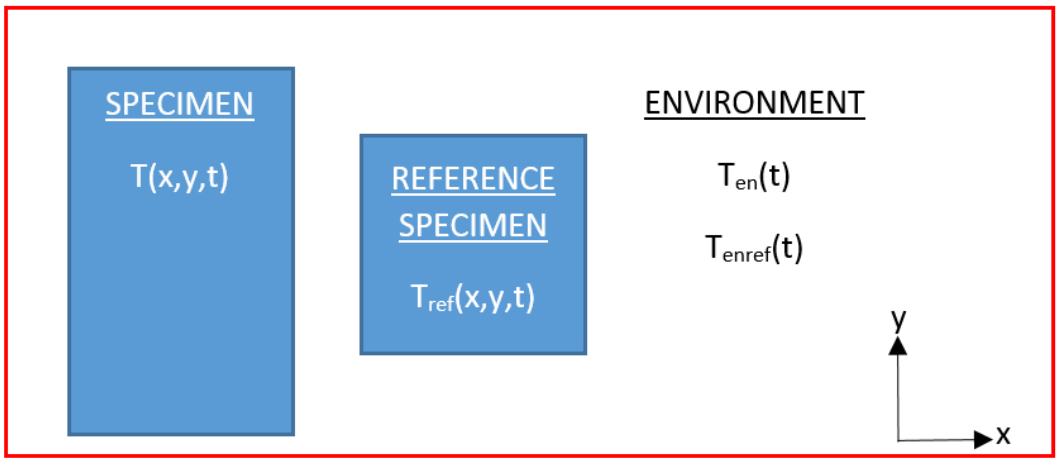

Figure 2.5 An illustration of the specimen and the reference specimen within the chamber (indicated by the red rectangle).

Figure 2.5 shows the environment in the chamber. $T(x,y,t)$ and $T_{ref}(x,y,t)$ are the surface temperature at any point (x,y) in the specimen and reference specimen respectively whereas $T_{en}(x,y,t)$ and $T_{enref}(x,y,t)$ are the corresponding air temperature in contact with any point (x,y) on the specimen and reference specimen respectively. There are three heat transfer routes:

- in-plane conduction at the end of the specimen (near the grips) : $-k\nabla^2 T(x,y,t)$
- radiation over the front and back surfaces of the specimen: $\frac{2BeT^4(x,y,t)}{d}$
- convection over the front and back surfaces of the specimen: $\frac{2h}{d}\left(T(x,y,t)-T_{en}(t)\right)$

where B is the Stefan-Boltzmann constant, k is the thermal conductivity of the material, d is the thickness is the specimen, h is the convective heat transfer coefficient and $\nabla^2 T$ is the 2D Laplacian of temperature which is given by $\frac{\partial^2 T}{\partial x^2}+\frac{\partial^2 T}{\partial y^2}$. The thermal energy balance per unit volume at any point (x,y) of the surface of the gauge section of the specimen can be written as [13]:

$$\rho C\frac{\partial T(x,y,t)}{\partial t}-k\nabla^2 T(x,y,t)+\frac{2BeT^4(x,y,t)}{d}+\frac{2h}{d}\left(T(x,y,t)-T_{en}(x,y,t)\right)=S(x,y,t)+r_{spec}(x,y,t) \quad 2.20$$

where ρ is the density of the material, C is the specific heat capacity of the material, S is the thermomechanical source which is the sum of thermoelastic source S_{TE} and dissipative heat source, S_D, and r_{spec} denotes all other external sources acting on the specimen.

Accurate calculation of the thermomechanical sources requires precise values of $T_{en}(x,y,t)$ and r_{spec}. These quantities are difficult to measure and it is not appropriate to assume that these quantities are

constant over time as will be demonstrated in a later section. Therefore, the reference specimen is introduced, located next to the gauge section of the specimen as shown in Figure 2.5, allowing the variation in $T_{en}(x,y,t)$ and r_{spec} to be taken into account without actually being measured. The reference specimen does not contact the specimen at any point, hence eliminating any possibility of heat conduction to and from the reference specimen. The thermal energy balance per unit volume at any point (x,y) of the surface of the reference specimen can be written as:

$$\rho C \frac{\partial T_{ref}(x,y,t)}{\partial t} + \frac{2BeT_{ref}{}^4(x,y,t)}{d} + \frac{2h}{d}\left(T_{ref}(x,y,t) - T_{enref}(x,y,t)\right) = r_{ref}(x,y,t) \qquad 2.21$$

where the subscript for T and r is *ref* indicating reference specimen. At time $t = 0$, just before the cyclic loading is started, thermomechanical sources are not yet activated. Hence, the thermal energy balance per unit volume of the specimen at $t = 0$ can be written as:

$$\rho C \frac{\partial T(x,y,t)}{\partial t}_{(t=0)} - k\nabla^2 T_0(x,y) + \frac{2BeT_0^4(x,y)}{d} + \frac{2h}{d}\left(T_0(x,y) - T_{en0}(x,y)\right) = r_{spec0}(x,y) \qquad 2.22$$

where the subscript zero denotes values at time $t = 0$ and $\frac{\partial T(x,y,t)}{\partial t}_{(t=0)}$ is the gradient of the temperature with respect to time at $t = 0$ just before the cyclic loading is applied. Similarly, the equation for the reference specimen at $t = 0$ is as follows:

$$\rho C \frac{\partial T_{ref}(x,y,t)}{\partial t}_{(t=0)} - k\nabla^2 T_{ref0}(x,y) + \frac{2BeT_{ref0}{}^4(x,y)}{d} + \frac{2h}{d}\left(T_{ref0}(x,y) - T_{enref0}(x,y)\right) = r_{ref0}(x, \qquad 2.23$$

By subtracting Equation 2.22 from Equation 2.20, the following expression is obtained:

$$\begin{aligned} &\rho C\left[\frac{\partial \theta_{spec}(x,y,t)}{\partial t} - \frac{\partial \theta_{spec}(x,y,t)}{\partial t}_{(t=0)}\right] - k\nabla^2\theta_{spec}(x,y,t) + \frac{2Be}{d}\left(T^4(x,y,t) - T_0{}^4(x,y)\right) \\ &+ \frac{2h}{d}\left(T(x,y,t) - T_0(x,y)\right) - \frac{2h}{d}\left(T_{en}(x,y,t) - T_{en0}(x,y)\right) = S(x,y,t) + r_{spec}(x,y,t) - r_{spec0}(x,y) \end{aligned} \qquad 2.24$$

where $\theta_{spec}(x,y,t) = T(x,y,t) - T_0(x,y)$ (i.e. $\theta_{spec}(x,y,t)$ is the temperature field of the specimen after subtraction of the initial image just before the start of the cyclic loading).

The temperature variations observed in this thesis is very low and hence T and T_0 values are very close. By assuming that $T \approx T_0$, the radiation term can be linearised in the same way as in [20]:

$$\begin{aligned} &T^4(x,y,t) - T_0{}^4(x,y) \approx \left(T^2 - T_0{}^2\right)\left(T^2 + T_0{}^2\right) \\ &\approx \left(T - T_0\right)\left(T + T_0\right)\left(T^2 + T_0{}^2\right) \approx \left(\theta_{spec}\right)\left(2T\right)\left(2T^2\right) \\ &\approx 4\theta_{spec}(x,y,t)T^3(x,y,t) \approx 4\theta_{spec}(x,y,t)T_0{}^3(x,y,t) \end{aligned} \qquad 2.25$$

The time constants of heat exchange through radiation and conduction could be written as follows by grouping all the constants in their respective term in the heat diffusion equation (Equation 2.20):

$$\tau_{radiation} = \frac{\rho C d}{8 B e T_0^3} \tag{2.26}$$

$$\tau_{convection} = \frac{\rho C d}{2h} \tag{2.27}$$

The time constant for the total heat exchange can then be obtained by using the relationship $\frac{1}{\tau} = \frac{1}{\tau_{radiation}} + \frac{1}{\tau_{convection}}$ which results in $\tau = \frac{\rho C d}{8 B e T_0^3 + 2h}$. Then Equation 2.24 then becomes:

$$\begin{aligned} &\rho C\left[\frac{\partial \theta_{spec}(x,y,t)}{\partial t} - \frac{\partial \theta_{spec}(x,y,t)}{\partial t}_{(t=0)}\right] - k\nabla^2 \theta_{spec}(x,y,t) + \rho C \frac{\theta_{spec}(x,y,t)}{\tau} \\ &- \frac{2h}{d}\left(T_{en}(x,y,t) - T_{en0}(x,y)\right) = S(x,y,t) + r_{spec}(x,y,t) - r_{spec0}(x,y) \end{aligned} \tag{2.28}$$

Similarly, the equation for the reference specimen is obtained by subtracting Equation 2.3 from Equation 2.1 and simplifying the convective and radiative term:

$$\begin{aligned} &\rho C\left[\frac{\partial \theta_{ref}(x,y,t)}{\partial t} - \frac{\partial \theta_{ref}(x,y,t)}{\partial t}_{(t=0)}\right] + \rho C \frac{\theta_{ref}(x,y,t)}{\tau} \\ &- \frac{2h}{d}\left(T_{enref}(x,y,t) - T_{enref0}(x,y)\right) = r_{ref}(x,y,t) - r_{ref0}(x,y) \end{aligned} \tag{2.29}$$

where $\theta_{ref}(x,y,t) = T_{ref}(x,y,t) - T_{ref0}(x,y)$ (i.e. $\theta_{ref}(x,y,t)$ is the temperature field of the reference specimen after subtraction of the last image before the start of the cyclic loading). Note that as the reference specimen is not subjected to loading, the thermomechanical sources are not activated and hence not present in Equation 2.29.

The heat diffusion equation for both the specimen and the reference specimen has been derived in this section. The next step will then be to subtract the influence of the reference specimen from the specimen. However, this is different with the different methods used. As such, they are presented separately for the spatial averaging method (Chapter 4) and the image processing (Chapter 6) method. It is after this that the equation becomes fully enabled to calculate the heat source from the temperature measured. Various processing approaches existing in the literature and their applications are reviewed in the following section.

2.4.3 Recent developments in the study of dissipative metals

The first study where an infrared camera was used to obtain the temperature evolution that occurs as a result of the dissipative heat source was the pioneering work of Chrysochoos and Dupre [9]. A

common approach in obtaining the dissipative heat source is to utilise the full-field nature of the infrared measurement by employing spatial averaging across the elements of the detector. This method is only useful when the temperature distribution within the averaged area is homogeneous. Hence, specimens with homogeneous stress fields are appropriate as detailed in Chapter 4. Some of the work that uses spatial averaging also known as the '0D approach' include [20, 56], where these works explored the fatigue behaviour of steels and aluminium respectively. Pierron and co-workers [5, 6, 13, 39] used spatial averaging to show that the dissipative heat source is sensitive to the microstructure. Maquin and Pierron [13, 39] investigated the intrinsic dissipation in the initial few cycles to explain the activation of different deformation mechanisms at the microscale. When the evolution of heat was considered cycle by cycle, it was seen that the dissipation per cycle was constant and this was attributed to viscoelastic behaviour (internal friction) resulting from reversible movement of dislocations. Above a certain stress level, an initial surge in the energy dissipated was also noticed and this was said to be caused by microplasticity or the creation of new dislocations. This can be seen in Figure 2.6. Subsequently, Connesson *et al.*[57] also found that, for low stress levels after a few hundred cycles (plastic work reduces to a negligible level), the viscoelastic work is responsible for the self-heating phenomena.

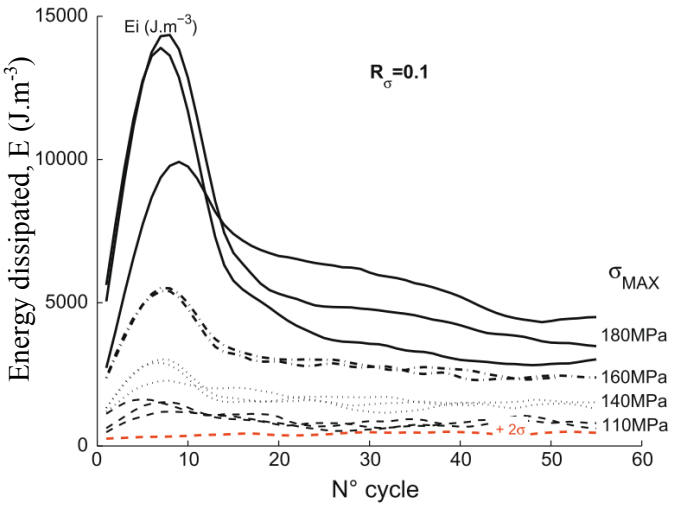

Figure 2.6 Energy dissipated per cycle for various stresses at a load ratio, R_σ of 0.1 for a steel specimen [39].

Additionally, Connesson *et al.* [5] found that, for 316L stainless steel, the energy dissipated increases with the cumulative plastic strain in a non-linear fashion (refer Figure 2.7). This further shows that the dissipative heat source is a sensitive indicator of microstructural evolution since it can be said that dislocation density increases with plastic strain. However, they found that, repeating the same test with a different specimen from the same batch of material showed significant scattering. This was attributed to inconsistencies in the cold rolling process that leads to heterogeneities in the condition of the material. This highlights the need for ensuring that materials of the same batch

produce consistent dissipation behaviour. It was also found that the room temperature recovery period does not influence the energy dissipation of 316L stainless steel which means that the specimen could be tested after a certain period to produce the same consistent values.

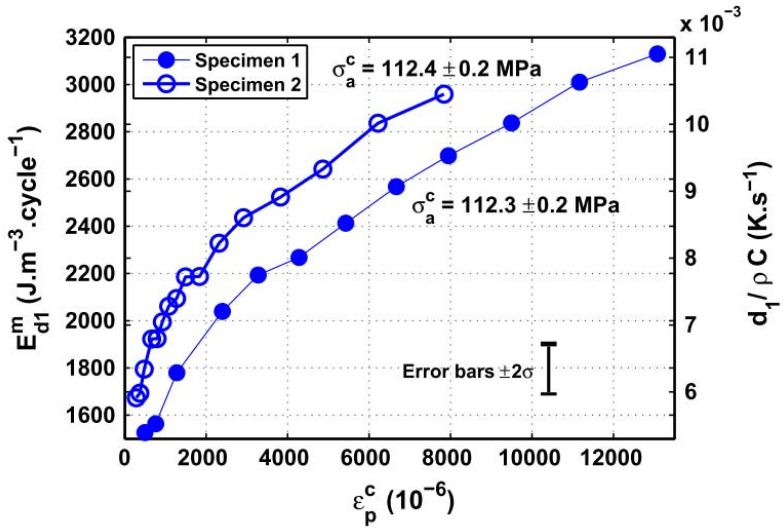

Figure 2.7 Energy dissipated by 316L cyclically loaded at the same stress amplitude at increasing levels of plastic strain for two different specimens of the same batch [5].

In [57], the energy dissipated by 316L was measured at different mean stresses, σ_m with a range of stress amplitudes (see Figure 2.8) .It was also found that the mean stress does not affect the energy dissipated by 316L. This implies that residual stress found in welded specimen is not likely to have an effect on the dissipative heat source.

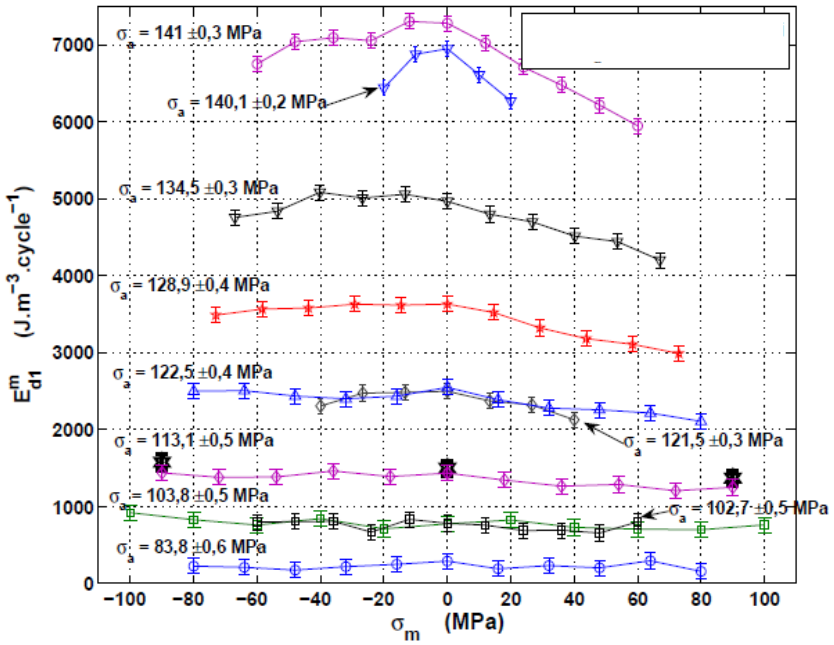

Figure 2.8 The effect of mean stress on the dissipative heat source of 316L at different stress amplitudes [57].

Another approach, first introduced by Chrysochoos and Louche [58] to calculate heat sources accompanying monotonic tensile tests, is to spatially resolve the data to obtain the full-field dissipative heat source – meaning spatial distribution of the heat source could be obtained as opposed to the spatial averaging method. The primary challenge associated with spatially resolving the heat source is the evaluation of the Laplacian term or spatial gradients (Equation 2.28). The Laplacian operator significantly amplifies noise and thereby has a deleterious effect when deriving the heat source. Subsequently, Berthel *at al.* [17] introduced a spatio-temporal approach to obtain the heat sources that accompany cyclic loading which enabled the direct evaluation of both the thermoelastic and dissipative heat source independently. This was done by least square fitting in space and time over a small window over the entire data set. The fitting function consisted of linear and trigonometric terms temporally whereas the spatial distribution is approximated using a second order polynomial. The window provides the much needed smoothing that is required to calculate the Laplacian term. Other more recent methods include the use of Proper Orthogonal Decomposition (POD) [59], Gaussian filter [60], and modal decomposition [61] to pre-filter the data before determining the dissipative heat source. There are also other methodologies which are intended for a more specific application such as that of Pottier *et al.* [62] , where a motion compensation technique was incorporated into the calculation in the procedure to take account of the large motions experienced by an elastomeric material. It was then shown that the dissipative heat source arising from rubber can be successfully identified.

In general, image processing procedures have mostly focused on identifying regions of cumulative plastic damage developed during fatigue loading [63], strain localisation phenomena in a monotonic tensile test such as Lüders band propagation [10] or Portevin-Le Chatelier effect [64] to name a few. Another domain of application is the study of the phase transformation behaviour in shape memory alloys. Delpueyo *et al.* [65] showed that the heat source is sensitive to stress induced phase transformation, that is, austenite to martensite transformation as shown in Figure 2.9 (red bands) where formation of martensite needles can be seen. The martensite grew at a macroscopic scale under cyclic loading since the Cu-Al-Be shape memory alloy used was a single crystal specimen. However, the heat source in this case is the combination of thermomechanical coupling, dissipation, and latent heat as opposed to just dissipation. Latent heat is in fact the dominant phenomena as shown in Figure 2.9, where the positive heat source corresponds to latent heat production whereas the negative heat source represents latent heat of absorption. There has not been any other microstructural characterisation attempt using dissipative heat source or the consideration of full-field dissipative heat source distribution of a weld.

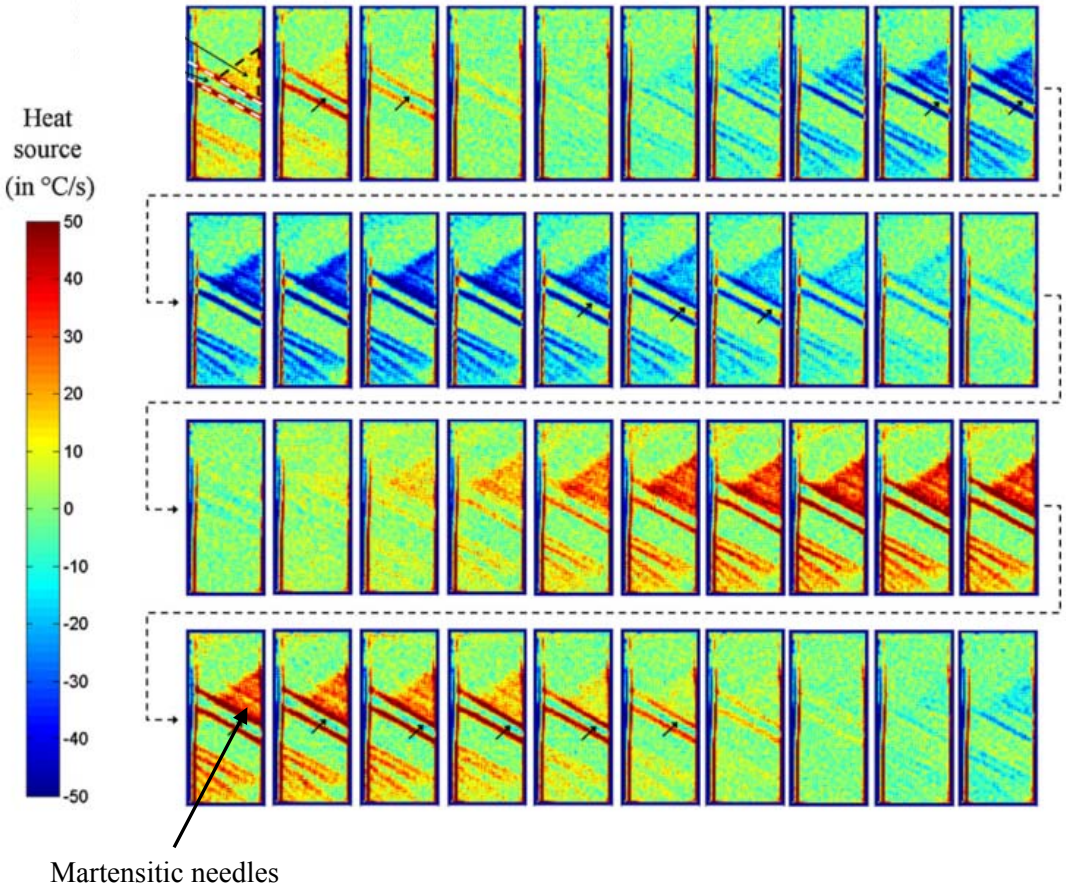

Figure 2.9 The heat source evolution of a Cu-Al-Be shape memory alloy in one load cycle showing the formation of martensitic needles in red [65].

2.5 Summary

The purpose of the review chapter is to explore the dissipative heat source behaviour of a material in response to mechanical loading to support the work carried out in the thesis. In the first part of the review, it was shown that, using the thermodynamics of irreversible processes involving the first and second laws of thermodynamics, the application of mechanical load on a material leads to the activation of two main heat sources: the thermoelastic source and the dissipative heat source. It is then explained that the thermodynamic irreversibility that is responsible for the dissipative behaviour originates at the microscopic scale. Thus, it is evident that there is a connection between the material microstructure and energy dissipation.

The difficulty in producing the dissipative heat source of material is that it cannot be directly assessed and has to be calculated from the resulting dissipative temperature rise. Therein lies the key challenge encountered in this work: the temperature rise in metallic materials and particularly under elastic loading is usually very low with respect to the temperature resolution of the currently available infrared cameras. Although many researchers have used the dissipative temperature rise alone to

analyse the fatigue behaviour of a material, the review has shown that this is unsuitable in the context of material characterisation. Therefore, it is proposed that these challenges are overcome by incorporating aspects of the methodology proposed by Maquin and Pierron [13] to assess very small heat sources. As discussed, this was possible due to the use of reference specimen that corrects for environmental temperature fluctuations and an insulation chamber that protects the specimen from external radiation.

It was also found that there are various ways to resolve the full-field heat source distribution of a material. Notwithstanding this, the heterogeneity of the heat source assessed was always in the form of phase transformation or plasticity associated phenomena. This presents a clear scope to resolve the full-field dissipative heat source distribution in a material that is microstructurally heterogeneous, which is the main research question addressed in the thesis.

3 Definition of experimental methodology

3.1 Introduction

To activate the heat sources it is necessary to apply a cyclic load, which in the present work is done using a servo-hydraulic testing machine. The cyclic loading activates both the thermoelastic source and the dissipative source. As described in detail in the previous chapter, the heat sources are not directly measurable and can only be obtained by measuring the temperature evolutions resulting from the heat sources. In the context of material characterisation, temperature variation is a less accurate way of studying material behaviour as it is affected by heat exchanges with the surroundings. As the calculation of heat sources involves the elimination of these heat exchanges with the surroundings, the heat sources can be considered intrinsic to the material behaviour. However, the only way to derive the heat sources is to obtain the temperature change; this is done using an infrared detector. Therefore the first section of the chapter explores the fundamentals of infrared radiation and then the following section explains how the infrared radiation is used to measure temperature. In particular, the typical thermal calibration procedure developed by the manufacturer is described, followed by the pixel-by-pixel calibration implemented in the PhD to measure the very small temperature evolutions associated with dissipation.

As any heat input from the surroundings will affect the detector response, the practical considerations and challenges involved in obtaining the temperature evolutions resulting from the mechanical loading alone are described. The extent of temperature rise due to dissipative heat sources depends on the applied stress level and strain rate (in this case the cyclic loading frequency). As the temperature variations of interest occur in the first few cycles of loading at stress levels below or just about the macroscopic yield stress, these are lower than the temperature resolution of the infrared detector. With a limited detector sensitivity, it is important to reduce background radiation, one of the main sources of noise. Therefore, it is necessary to conduct experiments in a chamber that eliminates spurious radiation from the environment. An unloaded reference specimen is also contained in the chamber, which is used to eliminate any fluctuations in temperature within the chamber. The design of the chamber and mounting of the reference specimen are presented in Section 3.6 alongside other aspects of the experimental setup such as specimen design and test machine control. Test machine control is particularly important as the cyclic load must be applied to a high degree of accuracy and stability to obtain a steady temperature rise. This is enabled by Proportional, Integral, and Derivative (PID) tuning and further fine tuning achieved using the Amplitude Control mode in the test machine system. These features of the test machine are described in Section 3.6.3.

3.2 Electromagnetic spectrum

Electromagnetic (EM) radiation is a stream of photons, which are particles exhibiting wave like properties that move at the speed of light. It is emitted over a continuous range of wavelengths by all matter at temperatures above absolute zero. The amount of EM radiation emitted by an object and its distribution with respect to the wavelength depends mainly on its temperature.

In 1900, Max Planck introduced an analytical equation which describes how radiated energy from a source varies as a function of temperature and wavelength for a black body (ideal emitter/absorber). The equation can be written as follows [66]:

$$M(\lambda, T) = \frac{2h_p c^2}{\lambda^5}\left(\exp\left(\frac{ch}{k_B \lambda T}\right) - 1\right)^{-1} \qquad 3.1$$

where M is the radiant emittance, λ is the wavelength, T is the temperature of the source, c is the speed of light in vacuum, h_p is Planck's constant and k_B is Boltzmann's constant.

When Planck's Law is represented as isothermal curves (see Figure 3.1), it can be seen that at temperatures close to the room temperature, the maximum radiant emittance is observed in the region with wavelengths from 0.7 μm to 14 μm. These wavelengths fall in the infrared region of the electromagnetic spectrum as illustrated in Figure 3.2. This makes the infrared radiation particularly ideal for non-contact and accurate measurement of temperature variations occurring close to room temperature. However, at a given temperature, all real objects do not emit maximum thermal radiation. The ratio of the amount of radiation from the surface of a real object to the radiation of a black body at the same temperature is known as emissivity, *e*. Metal surfaces, which are highly reflective, have emissivity values below 0.1 as opposed to blackbodies which have an emissivity value of one. The radiation from metallic surfaces also contains a high amount of reflected radiation originating from the surroundings. The next section explains the operation of the infrared detector and Section 3.6.1 provides details of how accurate temperature measurement for metallic specimens can be made.

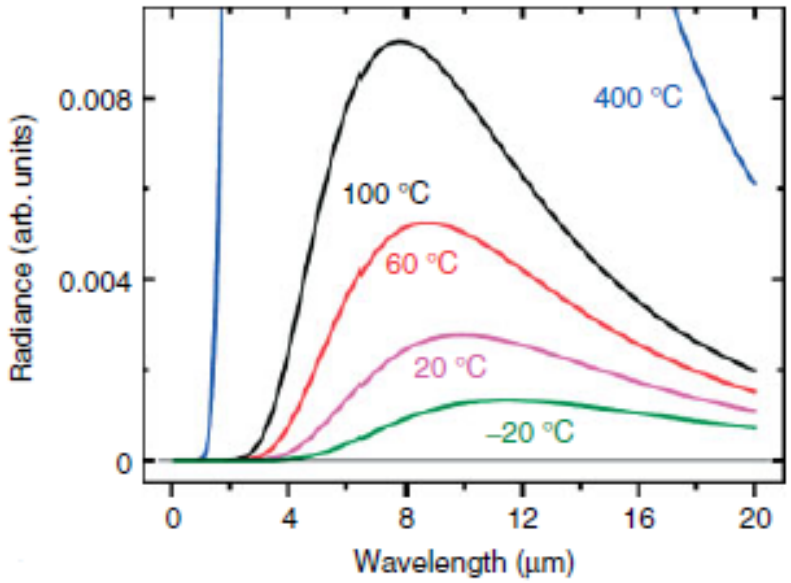

Figure 3.1 Radiance of black bodies at temperatures between -20 and 1000 ˚C according to Planck's law [66].

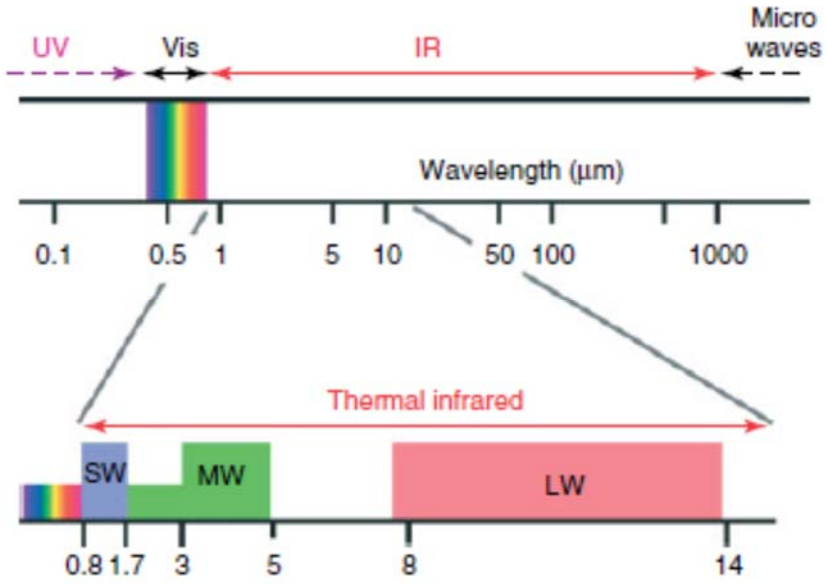

Figure 3.2 Partial Electromagnetic Spectrum showing the ultraviolet (UV), visible light, and the infrared (IR) spectral regions [66]. IR imaging systems typically utilise shortwave (SW), mid-wave (MW), or long wave (LW) sub-region of the IR region.

3.3 The Infrared Detector

The infrared camera used in the PhD is the SILVER 480M developed by Cedip Infrared Systems (now FLIR Systems). It comprises a photon detector which consists of two overlaid arrays of 320 x

256 elements made of Indium antimonide (InSb). The two overlaid arrays allows for sequential storage of data (new data can be captured while the captured data can be transferred to the internal buffer all at the same time) thereby enabling a maximum full frame rate of 383 Hz. The InSb detectors are only sensitive to the mid-wave (MW) sub-region of the infrared range (see Figure 3.2) which has wavelengths ranging from 3 to 5 μm. In this spectral range, the atmosphere, at imaging distances of up to 1 m, is almost transparent to the radiation [66]. The detector is cooled to about 77 K using a Stirling cooler because at higher temperatures, the thermal generation of charge carriers increases the noise level significantly.

In photon detectors, the change in electronic structure due to radiation absorbed by the detector produces an electrical signal described by the photoelectric effect. This signal is then digitised through an analog to digital converter (14 bits) and then sent to the computer in the form of digital signals in units of digital level, DL, stored in the Random Access Memory (RAM) of the computer. To obtain the temperature from the DL readings it is necessary to calibrate the system against a black body; in Section 3.3.1 the manufacturers recommended approach is described and in Section 3.4 an alternative in-house approach is described, which provides the necessary accuracy to conduct the experiments to identify the dissipative heat source.

Two types of lenses were used in the experiments conducted: the 27 mm lens and the G0.5 lens. The 27 mm inbuilt lens provides an angular field of view of 20˚ x 16˚. This lens has a minimum working distance of approximately 140 mm extending to infinity. At the minimum working distance (distance between the object and the front of the lens), the field of view (FOV) is limited to 54 x 44 mm translating to a maximum spatial resolution of 0.17 mm/pixel. The spatial resolution is increased further by using a specially designed magnifying/zoom lens that works with the 27 mm primary lens. One of the available magnifying lens is the G0.5 lens that increases the spatial resolution to 60 μm/pixel at a minimum working distance of approximately 46 mm; x 0.5 magnification results in 1 pixel having a resolution of two times the pitch size (30 μm). This corresponds to a FOV of 19.2 x 15.4 mm.

3.3.1 Manufacturers calibration of the infrared camera system

Traditionally, the DL signals are converted to temperature values using a procedure developed by the manufacturer. The method developed by Cedip is a two-step process, where the application of a calibration curve (produced by the manufacturer) is preceded by Non-Uniformity Correction (NUC) and Bad Pixel Replacement (BPR). As the detector array is made up of many individual sensor elements, each sensor produces a different signal for the same incident radiant power. This is due to the detector material and the sensor fabrication process used [67]. The NUC operation performed addresses this issue by unifying the response of all the detector element so that a single calibration curve could be used to convert DL to temperature. Typically, this is done by placing a high emissivity plate of homogenous temperature distribution in front of the lens, either at one temperature (single

point NUC) or two different temperatures (two point NUC). By assuming that the detector response is linear with respect to the incoming radiation, the offset and gain of every individual sensor is corrected so that that every sensor in the array has the same response to the incoming radiation. Subsequently, unresponsive sensor elements (known as 'bad pixels'), are identified and corrected. In this case the bad pixels are defined to be the pixels that show a significant deviation from the mean response of all the pixels in terms of the gain, offset, and noise (standard deviation) parameters [68]. A predefined threshold is then set for each of these parameters, and the sensor elements that fail to meet these thresholds are identified and replaced with the nearest responsive pixel. More details of the NUC and BPR method developed by Cedip can be found in [68]. The corrected DL values are then converted to temperature using calibration curves that are supplied by the manufacturer. These calibration curves depend on the integration time, akin to shutter speed in traditional photography, which controls the time available for the photons to impinge on the detector. An example of the calibration curve for an integration time of 1200 µs, provided by the manufacturer, is shown in Figure 3.3. This integration time was maintained throughout all the tests since it was found by Connesson in [57] that this integration time is ideal since it displays an almost linear behaviour around room temperature and does not saturate in the intended range of operation. Equally, this value is also close to the manufacturer's recommended value of 1332 µs.

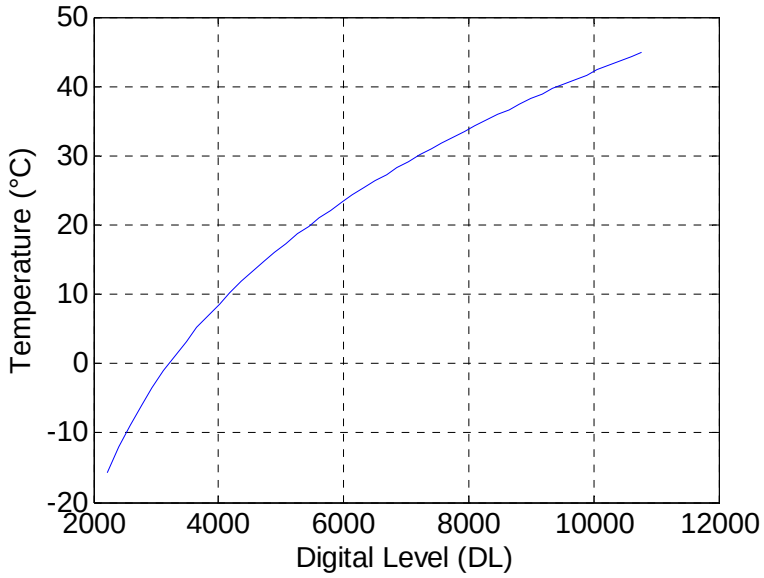

Figure 3.3 Calibration curve for an integration time of 1200 µs.

It is very important to understand that the application of such a simple calibration comes at the expense of a loss of accuracy. The underlying assumption of this method is that the response of each pixel is linear and this only holds true over a very small range of temperature (centred at the temperature at which NUC correction was performed). As such, the spatial distribution of the temperature, particularly outside this small temperature range, is less precise. Moreover, it is likely that some of the sensor elements that are not necessarily defective may be categorised as bad pixels [68]. This in turn makes the calculation of spatial gradients (Laplacian operator in Equation 2.28),

involved in the evaluation of the dissipative heat source, inaccurate, as noted in [69]. To obviate this and obtain a better accuracy, the following section describes the implementation of an in house procedure that provides a calibration curve for every sensor in the array, preserving the individual characteristic of every pixel.

3.4 In house pixel-by-pixel calibration

In essence, the implementation of the pixel-by-pixel calibration involves obtaining a calibration curve similar to the one given in Figure 3.3 for every pixel, fitting it to a polynomial function and then using the fitting parameters to calculate the temperature within that range. To conduct the calibration, it was necessary to set up an experiment so that the detector response in DL could be measured by viewing an object over a range of temperatures. A black body (IR – 2106/301 by Infrared Systems Development Corporation) was used as the test object. As shown in Figure 3.4, the black body consists of thermo-electrically cooled/heated solid copper emitter plate coated with a proprietary high emissivity black coating (emissivity, $e > 0.95$). The black body provided a constant and uniform source with a thermal resolution of 0.1 ˚C for the camera to observe. DL readings were then obtained over a temperature range of 17 °C to 55 °C in increments of 1 °C.

Figure 3.4 The IR - 2106/301 black body.

At each temperature, 350 frames was recorded at an integration time of 1200 μs (i.e. for a period of one second at a framerate of 350 Hz). To reduce the temporal noise, the 350 frames recorded were then temporally averaged which results in one frame at each temperature. The response of every pixel is then obtained as shown in Figure 3.5 where it is evident that each pixel has a slightly different response. Above 50 ˚C, the signals saturates while the inconsistent behaviour below 20 ˚C could be partially attributed to the decreasing thermal stability of the black body below room temperature. The constant response at all temperatures on the other hand indicate dead pixels.

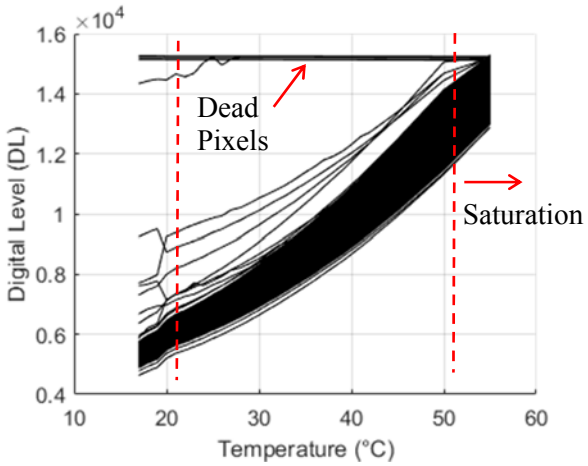

Figure 3.5 Detector response at different temperatures

Taking into account the upper and lower limits, as well as the fact that the temperature range encountered in this work is usually less than 5 ˚C starting from room temperature, the data points between 20 ˚C and 40 ˚C were selected for the polynomial fitting. At each pixel, the DL vs temperature response was fitted with a sixth order polynomial as shown in Figure 3.6 for one of the pixels. This is to ensure that even minor non-linearities in the pixel behaviour can be captured satisfactorily. The resulting seven coefficients for each of the pixels is stored in the form of a look up table, where the DL can be converted to temperature by using these coefficients.

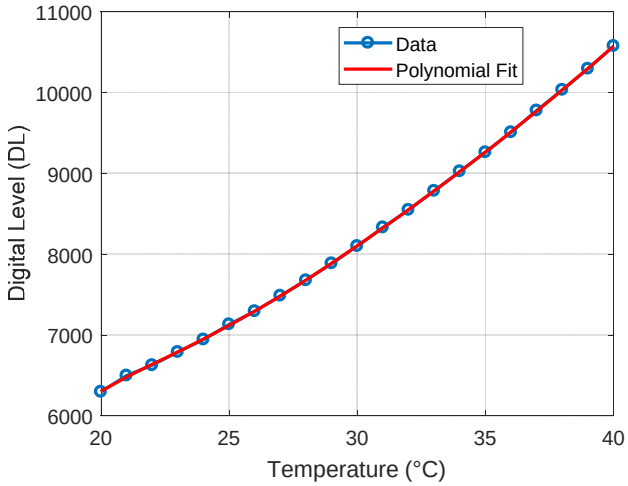

Figure 3.6 Polynomial fit for one pixel.

All previous work [17, 68, 69] employing a similar pixel-by-pixel calibration method have defined a certain threshold for both the mean and the standard deviation of the response to identify the dead pixels. As mentioned previously, doing so almost always overestimates the number of defective pixels. While defining a threshold helps in automating the identification of the dead pixels, some pixels that deviate significantly from the mean response but are still within the normal distribution

range are inevitably deemed as being defective. In view of this, the dead pixels are identified manually from each of the distributions of the coefficients of the polynomial. For instance, the distribution of the fifth order (x^5) coefficient is shown in Figure 3.7. The pixels that lie outside the normal distribution are identified and their location is stored. The locations of all of the dead pixels are shown in Figure 3.8; in total, 23 pixels were found to be defective and this represents approximately 0.03% of all the pixels in the detector array. The effectiveness of the identification of dead pixels was then evaluated by plotting the detector response, as in in Figure 3.5, without the response of the dead pixels. Figure 3.9 shows that all the dead pixels have been successfully removed. This implementation differs from the Bad Pixel Replacement (BPR) implemented by the manufacturers, in that the dead pixels here were replaced by the average of all the non-defective neighbouring pixels. In other words, if a neighbouring pixel is also found to be defective, it is not included when computing the average temperature. The implementation of the pixel-by-pixel calibration in Matlab is given in Appendix A.2.

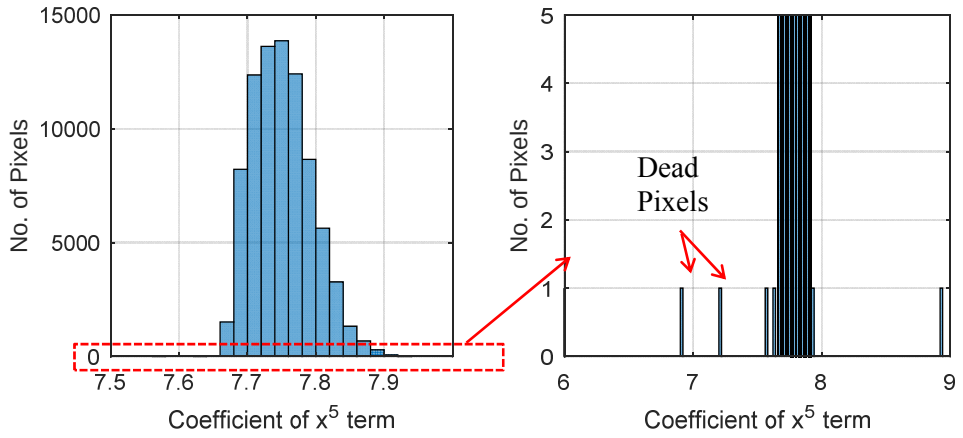

Figure 3.7 Identifying the dead pixels from the histogram of the polynomial coefficient.

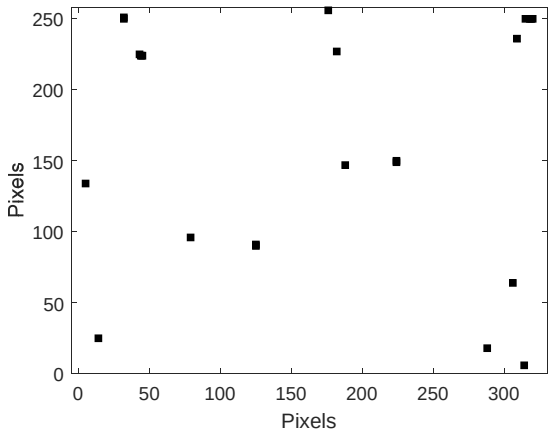

Figure 3.8 Location of the dead pixels in the detector array.

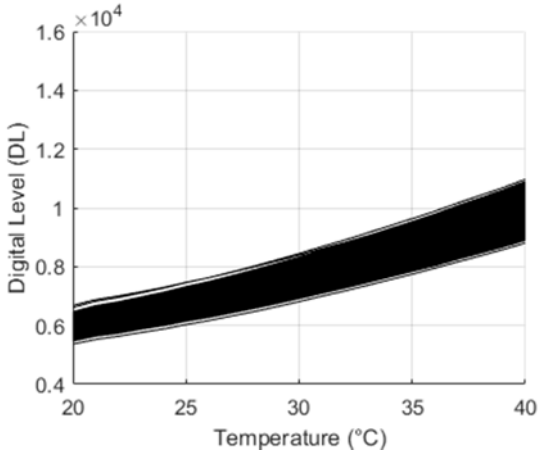

Figure 3.9 The detector response used for polynomial fitting.

3.5 Thermal resolution of the infrared camera system

The thermal resolution of the camera can be quantified using the Noise Equivalent Temperature Difference (NETD) of the detector. The NETD is the temperature difference which produces a difference in radiant power at the receiver input that is just equal to the electronic noise at the detector output [70]. Although a theoretical expression exists to calculate the NETD of the detector itself, a measured NETD for the whole system could be easily found by dividing the temporal noise (root mean square or standard deviation of the noise over a period of time) by the responsivity, R*, of the camera, which is defined as the detector output (DL) per unit temperature, usually in K. As the current work deals with temperature rise below the thermal resolution of the infrared detector, it is important to re-evaluate the NETD of the camera and compare it against the manufacturer's value of 20 mK given the age of the infrared camera (8 years at the time of writing). The temporal noise can be found by recording a constant and uniform source of temperature over a period of time. For this experiment, 100 images were captured at 350 Hz for 3 black body temperatures in a darkroom to avoid external reflections.

The temporal noise at 25 ˚C was evaluated by calculating the temporal standard deviation in each pixel over the 100 captured images, as shown in Figure 3.10. The responsivity of the camera was calculated for temperature values between 20 ˚C and 30 ˚C by obtaining the temporal average of the individual sensor responses in the detector array at black body temperatures of 20 ˚C and 30 ˚C. Then the responses were subtracted and divided by the temperature range (i.e. 10 K) to obtain R* (see Figure 3.11). Thus the map of NETD was produced as shown in Figure 3.12. The dead pixels mentioned in the previous section do not have an effect on the NETD since a constant response regardless of temperature means that the standard deviation is close to zero. Note that the NETD map shown is not indicative of the spatial noise present and is only a representation of the temporal NETD in each pixel [71]. This is due to the fact that fixed pattern/spatial noise has no effect on the

calculation of the standard deviation. However, the normal distribution of the NETD as seen in the histogram in Figure 3.13 suggests that there is no significant spatial noise.

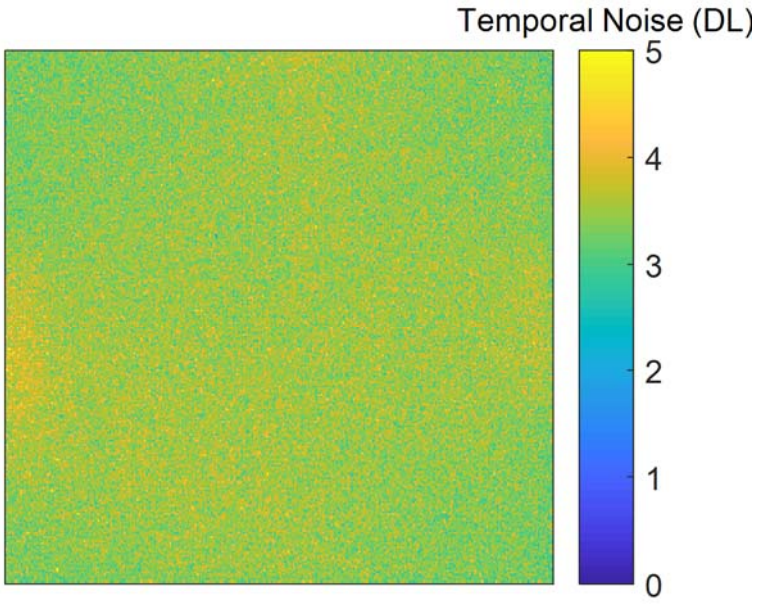

Figure 3.10 The temporal noise at 25 ˚C.

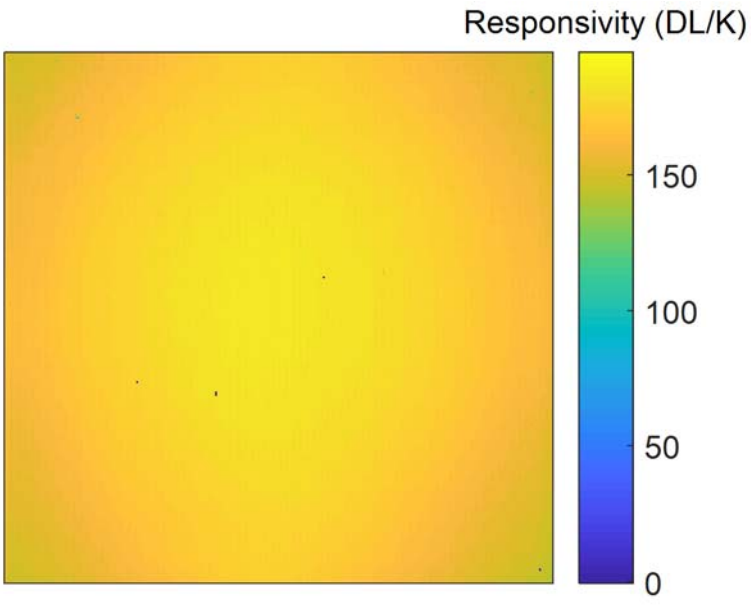

Figure 3.11 R* between 20 ˚C and 30 ˚C.

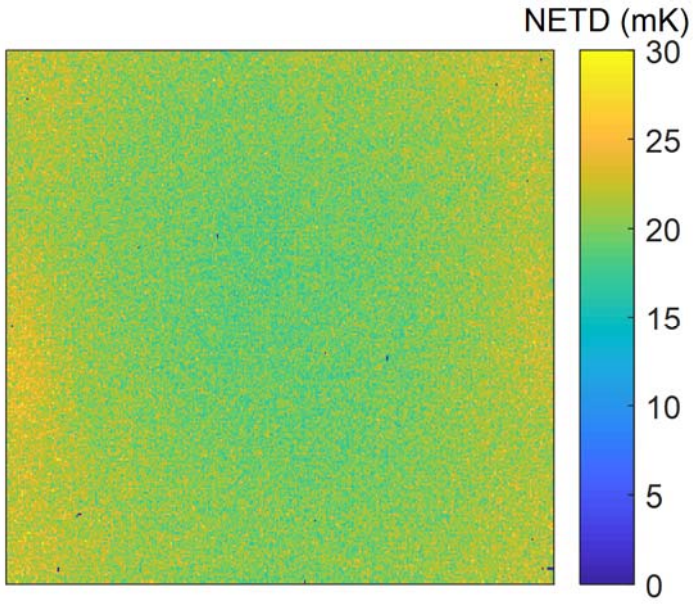

Figure 3.12 The NETD at 25 ˚C.

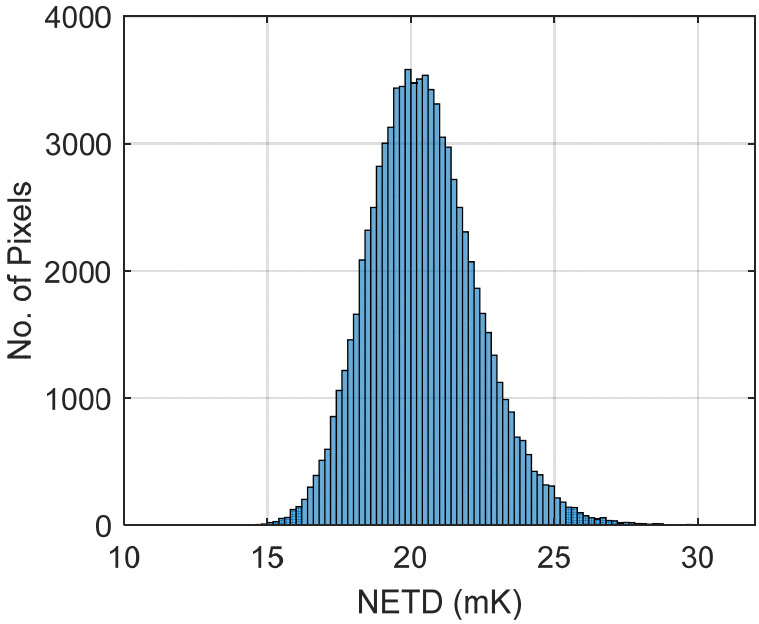

Figure 3.13 The NETD of all the pixels in the form of a histogram.

A single value for NETD was found by averaging across all pixels in the NETD map. The NETD at 25 ˚C was established to be 20 mK which shows that there is a real necessity for protective measures both experimentally and in data processing procedures, to enable accurate temperature measurement below this thermal resolution value.

3.6 Definition of experimental procedure

Figure 3.14 below shows an illustration of the experimental setup. The chamber has three openings, one at the top and the other at the bottom to allow the specimen to be inserted into the grips and a third one at the front side of the chamber for imaging the specimen. Adjacent to the specimen, a reference specimen is hung using tape. Curtains are hung around the test machine for further insulation in addition to the chamber. The different aspects of the experimental setup are discussed in detail below.

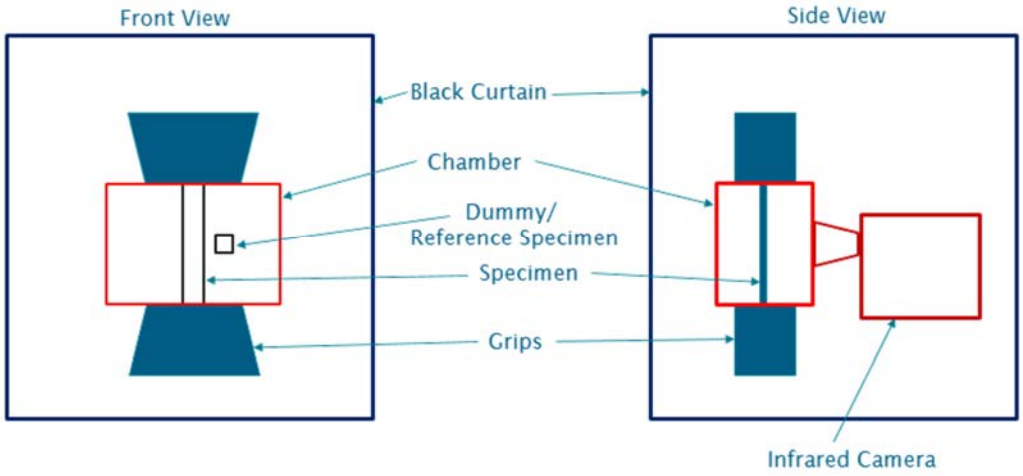

Figure 3.14 Schematic diagram of the experimental setup.

3.6.1 Specimen design

All specimens used throughout the PhD were manufactured from 316L stainless steel. In all the experiments conducted in this thesis, the thickness of the specimen, d, was chosen to be 2 mm to ensure that the temperature changes were homogeneous through its thickness. The length, l and width, b of the homogeneous strip specimen is shown in Figure 3.15 whereas the dimensions of the welded specimen are detailed in Chapter 7. For the 316L stainless steel used in this work, EN 10027 grade 1.4404, the thermal transport properties are listed in Table 3.1.

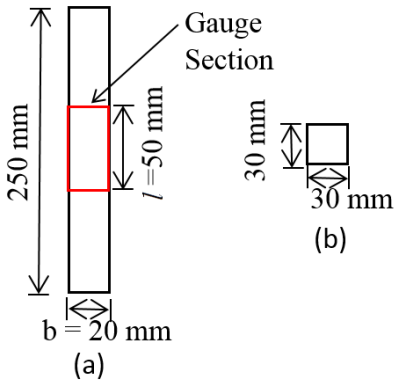

Figure 3.15 The dimensions of (a) the specimen and (b) the reference specimen.

Table 3.1 Thermal transport properties of 316L stainless steel [33].

Coefficient of linear thermal expansion, α (K^{-1})	**Density, ρ ($kg.m^{-3}$)**	**Specific heat capacity, C ($J.kg^{-1}.K^{-1}$)**	**Thermal conductivity, k ($W.m^{-1}.K^{-1}$)**
16×10^{-6}	8000	500	14

As metals generally have low emissivity, a thin layer of black paint (Electrolube EMB 400 matt black paint) was sprayed on both the specimen and the reference specimen to increase their emissivity. The thickness of the paint coating was measured using a paint thickness gauge (Elcometer 456 Coating Thickness Gauge) at different locations along the length of the specimen and was averaged. The average thickness was maintained to be approximately 25 µm with a standard deviation not exceeding 5 µm to ensure that the paint coating is uniformly distributed. This thickness is within the recommended paint coating thickness range of 15-25 µm [72]. Although the study in [72] was conducted for TSA, the results are still valid for the work performed here as both involve measurement of the temperature variation as a result of cyclic load.

3.6.2 Design of chamber

Although the specimen is coated with black paint, its emissivity is not exactly 1. This implies that the surface reflectance is not zero and hence reflections of external radiative sources could be incorporated into the measurement. If a parasitic heat source exists such that its reflection on the specimen is incorporated into the measurement whereas its reflection on the reference specimen is not, the reference specimen will no longer be able to account for the environmental temperature changes. Therefore, it is imperative that a chamber is placed around the specimen and the reference specimen to reduce the effect of parasitic heat source reflections from the surrounding environment. In other words, the chamber exists as a thermal barrier between the measurement space and the surroundings. The chamber was initially designed and constructed from polystyrene foam covered by aluminium foil on the outer side and black paper on the inner side. The shiny side of the aluminium

foil has a reflectivity of approximately 80 – 90%. This means that most of the external heat radiation is reflected so only a very small amount is absorbed. Polystyrene has a very low thermal conductivity which makes it a good heat insulator and prevents the passage of any absorbed radiation into the chamber. Black paper was used on the inner surface to reduce reflections of heat sources inside the chamber. It is important to note that the chamber was constructed so that the test machine hydraulic grips, which are a major source of radiated heat, are outside the chamber.

The experimental setup is shown in Figure 3.16. The necessity of the camera being able to view the specimen is enabled by an aperture in the chamber. The gap between the aperture and the camera lens is sealed using similar construction to that of the chamber. It should be noted that as the detector is cryogenically cooled; this introduces the possibility of reflections from the cold detector (77 K) onto the specimen to be recorded by the camera.

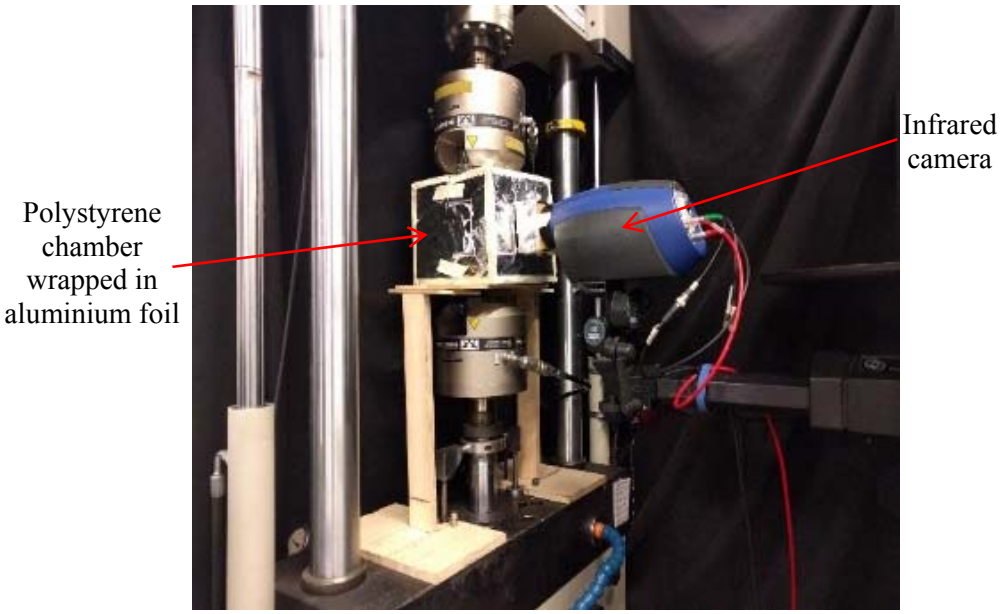

Figure 3.16 The initial experimental setup.

From the initial experiments carried out using the chamber shown in Figure 3.16, it was found that the thermal insulation provided by the chamber deteriorated with time as the chamber degraded. To improve the measurements and to simplify mounting the chamber on to the test machine a new wooden chamber was designed. This is shown in situ with the test machine in Figure 3.17 (a). The chamber consists of two halves: front and back and rests on the recess feature of the stand. The stand was secured to the test machine by screwing it to the screw holes in the test machine just below the grips. Although the specimen is not shown in Figure 3.17 (a), it is clamped to the grips of the test machine and the front and back halves of the chamber are positioned surrounding it. The primary advantage of the new chamber is that it is robust and easy to reuse for multiple experiments. As mentioned earlier, other new features include the stand (see Figure 3.17 (a)) which ensures that the chamber is stable and in the correct position and the recess feature on the connecting surface of the two halves of the chamber. The recess completely blocks all external radiation, is shown in the back

half and the front half of the chamber as shown in Figure 3.17 (b). The only gaps in the chamber are just the opening that enables the specimen to be inserted into the grips of the test machine. In some cases, the specimen was imaged at a higher spatial resolution using a magnifying lens. This required the camera to be closer to the specimen and as such, a provision to insert different types of front cover to the front half of the chamber was also made (see Figure 3.17 (b)). This was to ensure that when the camera needs to be brought closer to the specimen, only the front cover needs to be changed. An actual experimental set up involving the specimen is shown in Figure 3.18 (a) and the painted specimens are shown in Figure 3.18 (b).

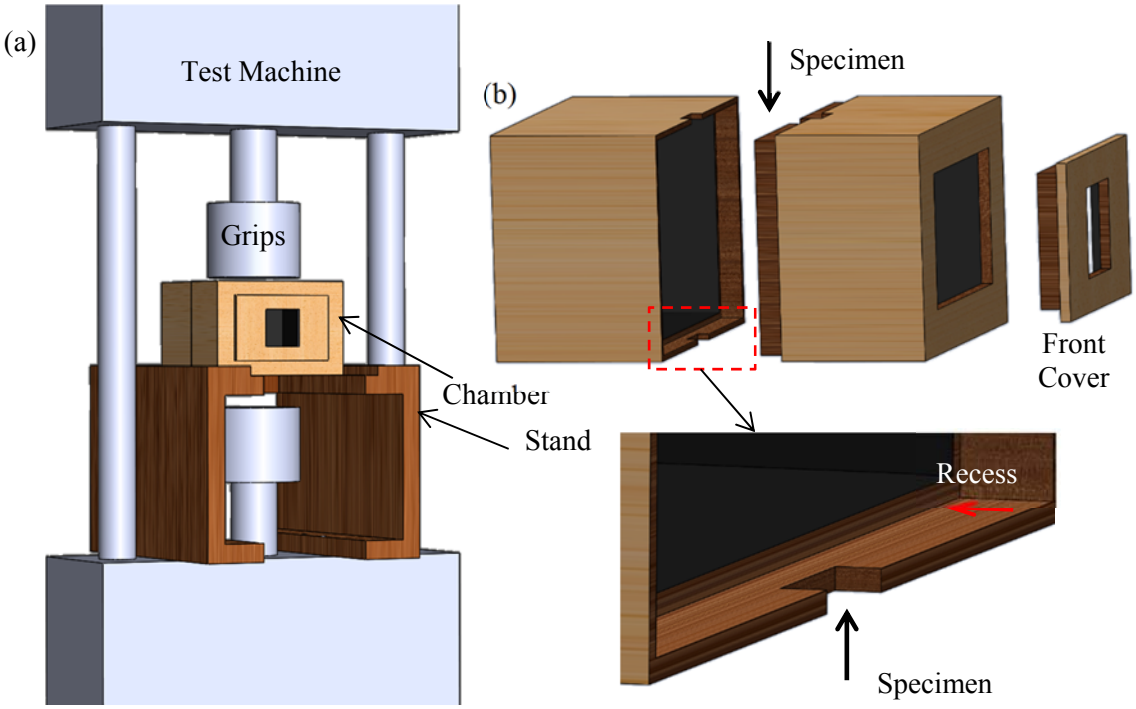

Figure 3.17 (a) Chamber in situ with the test machine (b) parts and feature of the chamber.

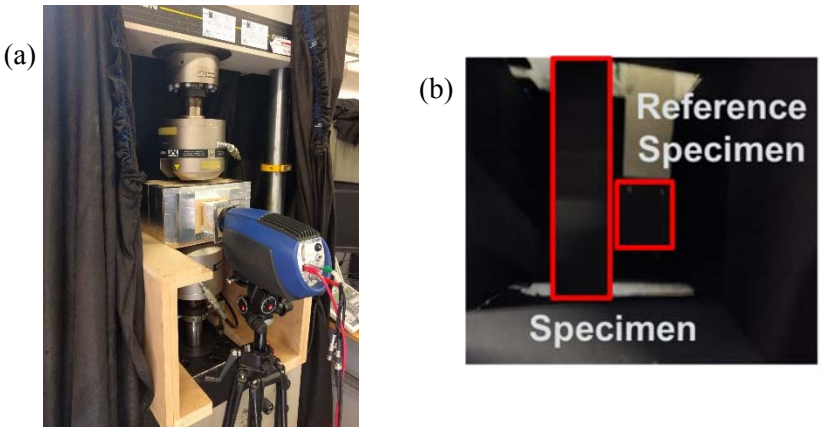

Figure 3.18 (a) Actual setup of the experiment (b) the position of the specimen and reference specimen within the chamber.

3.6.3 Test machine and loading

The cyclic load was applied using an Instron 8800 servo-hydraulic testing machine equipped with a 100 kN load cell (transducer that converts force into an electrical output). The cyclic stress was applied in the form of

$$\sigma = \sigma_m + \sigma_a \cos(2\pi f t) \qquad 3.2$$

where σ_m is the mean stress, σ_a is the stress amplitude, f is the frequency, and t is time. The load ratio, R_σ is given by the ratio of minimum stress, $\sigma_{\min}$ to maximum stress, $\sigma_{\max}$.

Throughout the PhD a load ratio of 0.1 was used for the cyclic loading. For example, at a maximum stress $\sigma_{\max}$ of 250 MPa the cyclic stress is given by 137.5 ± 112.5 MPa or 8.25 ± 6.75 kN for the specimen cross-sectional area of 40 mm^2. The specific load applied in each case is presented in the chapters dedicated to the results (Chapter 5 - 7). Note that the load is only applied to the specimen and the reference specimen is not loaded at all. The loading frequency used here was 14 Hz for all the tests. At this frequency, the temperature rise due to dissipation is detectable. In addition, the thermoelastic temperature variation can be removed. At a loading frequency of 14 Hz and camera frame rate of 350 Hz, the sampling frequency corresponds to 25 frames per cycle. The importance of having an exact number of frames in a load cycle is detailed in Chapter 6.

When using a servo-hydraulic test machine to obtain the required load it is necessary to use a closed loop control systems. This is to ensure that the load entered on the controller will closely be replicated on the specimen. A proportional-integral-derivative (PID) controller is usually employed in the servo-hydraulic test machines to do this. The PID controller measures the error given by the difference between the measured and the desired values and attempts to minimise this error by adjusting the control variable. The control variable is the sum of three terms: proportional, integral, and derivative. The proportional term is the product of the current error value and the proportional gain constant. The proportional gain constant indicates the level of error amplifier and is representative of the actuator piston displacement. The derivative term is the product of the rate of change of error and the derivative constant. The derivative action helps to predict the behaviour of the system by identifying how fast the error is approaching zero. This ensures that the system is stable. The integral term is the product of the accumulated error over time and the integral constant. The integral term facilitates the elimination of the residual steady state error and thereby brings the output to its desired set point. The PID constants can be obtained by tuning the control loop. Loop tuning is a complex process as different behaviour and requirements may exist for different systems. For example, when the test machine is used in load control, the specimen stiffness contributes to the error. This shows that, in addition to system behaviour, the stiffness of the specimen can also contribute to the complexity of the loop tuning process.

The Instron 8800 has an in-built function which allows the PID constants to be automatically tuned. Auto-tuning was performed every time the test machine was started. The maximum allowable frequency is 10 Hz during auto tuning. Although the desired frequency is 14 Hz, the auto-tuning was performed at 5 Hz as it produces a more stable constant amplitude load signal. During auto tuning the mean load is set to be the same as the actual mean load whereas the amplitude is taken to be ±10 % of the mean load i.e. for an actual load of 2.20 ± 1.80 kN, the test machine is auto tuned at 2.20 ± 0.22 kN at 5Hz. The stable load signal resulting from the auto tuning procedure is shown in Figure 3.19. However, it remains that the first 10-15 cycles (approximately 1s for a loading frequency of 14 Hz) is still required to reach the desired range.

At higher frequencies, the amplitude of the feedback waveform usually decreases. This is not ideal for constant amplitude tests. This is overcome by using an inbuilt function in Instron 8800 known as the 'Amplitude Control'. This function automatically increases the command signal amplitude as the frequency increases. Due to operation close to the system performance boundaries, this function also ensures that the mean load does not drift. In general, the stability of the temperature variation strongly depends on the stability of the applied load. Therefore correct tuning and setting of the PID parameters is required to produce a smooth temperature increase.

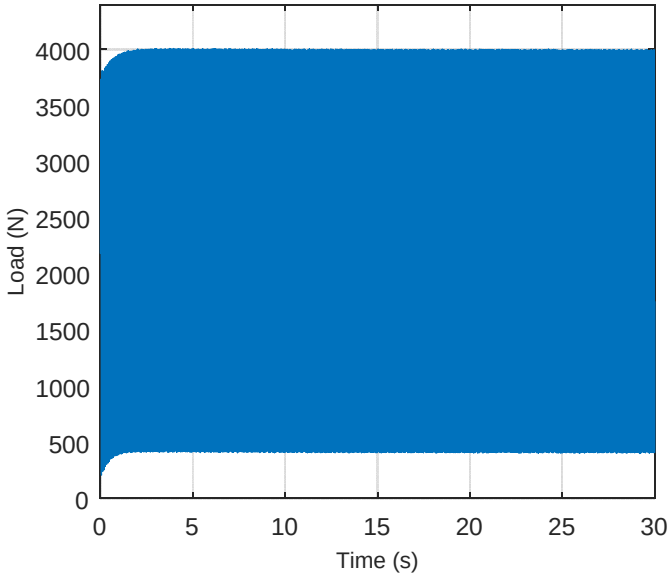

Figure 3.19 Load signal for an applied load of 2.2 ± 1.8 kN

3.7 Summary

To evaluate the small temperature changes that occur as a result of dissipation, the detector non-uniformity correction proposed by the manufacturers of the infrared camera was insufficient.

Therefore a pixel-by-pixel temperature calibration was successfully implemented to ensure that the spatial distribution of the temperature recorded is of sufficient accuracy for further data processing.

The age of the infrared camera warranted a re-examination of its performance. The NETD value of the infrared camera was experimentally determined to be 25 mK as reported by the manufacturers. Establishing the NETD was also essential in examining the effectiveness of the experimental procedure devised, as the noise could be caused by either ineffective experimental procedure or increased noise of the detector or both. The key aspects of the experimental setup required to enable accurate temperature measurement are the introduction of a reference specimen to account for the fluctuations in the environmental temperature and the use of an insulation chamber designed especially to block parasitic heat sources from being incorporated into the measurements. These features were successfully incorporated into the experimental setup enabling an accurate measurement of the temperature evolution of the specimen unaffected by parasitic heat sources. In addition, steady temperature rise could only be achieved when the applied loading is stable and as such, it was also ensured that the loading applied is accurate by using the 'Amplitude Control' functionality of the test machine system along with PID tuning.

Nevertheless, the intensity of the heat source and hence the magnitude of the temperature rise encountered in this work is very small and in some cases below the thermal resolution of the infrared detector (20 mK). It is therefore necessary to apply specialised data processing procedures to enhance the signal to noise ratio. One of the data processing methods developed in this work is the spatial averaging method which is presented in Chapter 4. As detailed later in Chapter 4, this method is limited to situations where the dissipative heat source distribution is uniform across the specimen. As such, image processing procedure was also developed to study inhomogeneous dissipative heat source distribution such as that encountered in a weld, as detailed in Chapter 6.

4 Determining the heat sources by spatially averaging the image data

4.1 Introduction

The specially designed experimental setup described in Chapter 3 eliminates many of the effects that would mask the accurate measurement of the temperature evolution associated with dissipation. However, the experimental setup alone does not facilitate the required thermal resolution. It should be noted that the setup cannot account for the heating effect of the test machine actuator, as there is a direct connection to the specimen through the test machine jaws. Also, as the detector is cryogenically cooled, there will be a reflection of the cold detector on the specimen which is also included in the image data. To account for both these effects, a common image processing procedure is simply to subtract the first image in the data set from all the others; here the image that is subtracted is the one captured just before the cyclic loading is applied. When the initial image subtraction procedure has been carried out and the data has been corrected for environmental effects from inside the chamber using the reference specimen data, all the external factors have been eliminated from the response. However, even when all the external factors have been removed, the NETD of the system is still 20 mK, as described in Chapter 3. Hence data and image processing approaches, such as those used in [6], are required to improve the detection threshold by reducing the effect of detector noise to achieve the required thermal resolution.

A simple approach to implement is spatial averaging where the average of all the pixels in an image frame is obtained to provide a single data point reading from each frame in an image sequence. This approach is only applicable for situations where the temperature data is nominally uniform across the frame. In addition, smoothing and least squares fitting were also used to reduce the noise. This chapter presents the data processing procedures adopted to obtain spatial averaged data which can be used in conjunction with Equations 2.28 and 2.29 to extract the dissipative heat source. These equations, in 2D form, are developed into the spatially averaged form progressively, detailing the data processing procedure involved at every stage. To demonstrate that the procedure is effective, the chapter is concluded with an example of the resulting dissipative heat source evolution and the detection threshold is established for the experimental set-up and the data processing based on spatial averaging. Finally, typical examples of the evolution of the dissipative heat source under elastic and elastic-plastic cyclic loading are presented and they are explained in terms of dislocation motion.

4.2 Overview of data processing

The raw data from the infrared camera is obtained in the form of an 2D image sequence of temperature fields of the reference specimen $T_{ref}(x,y,t)$ and the specimen $T(x,y,t)$. The data processing steps revolve around the derivation of the spatially averaged heat diffusion equation from the 2D form of the heat diffusion equations (Equations 2.28 and 2.29). These data processing steps are illustrated in Figure 4.1 and are as follows:

1. Image subtraction; the first image (before the start of the cyclic loading) is subtracted from the subsequent images – this eliminates the undesirable temperature gradient in the specimen resulting from heat transfer through the test machine jaws and the reflection of the cold detector.
2. Spatial averaging; it is assumed that the spatial mean of the temperature change in the test specimen and the reference specimen frame by frame are representative of the local thermomechanical sources.
3. The spatial mean of the reference specimen temperature variation is subtracted from the spatial mean of the specimen temperature variation – to account for variation in environmental temperature within the chamber.
4. Extracting mean temperature rise - the thermoelastic temperature variation, $\overline{\overline{\theta}}_{TE}$ is subtracted from the overall temperature change, $\overline{\overline{\theta}}$ to extract dissipative temperature rise, $\overline{\overline{\theta}}_D$.
5. Obtaining dissipative heat source, S_D - other quantities needed to calculate the dissipative heat source such as the time constant of heat exchange, τ and the Laplacian of the vertical temperature profile, $\nabla^2\overline{\theta}$ are evaluated.

These steps along with the derivation of the equations are detailed in the following sections.

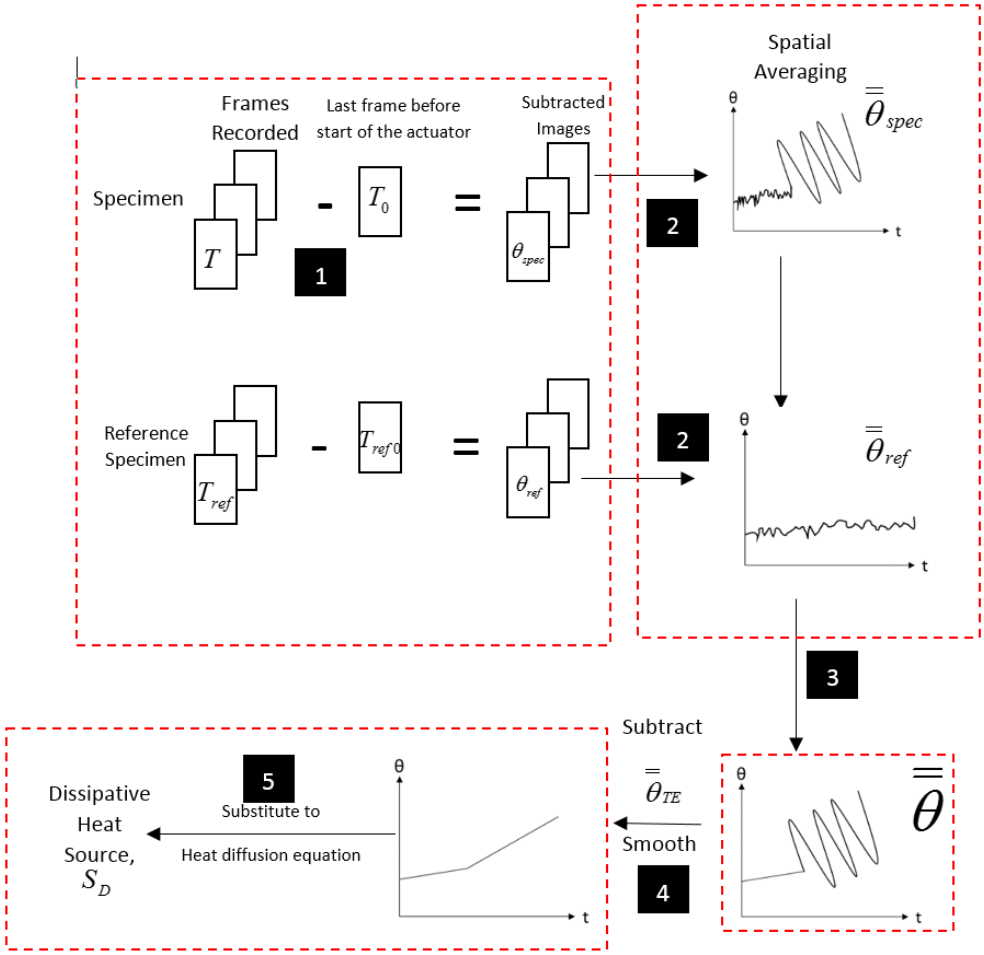

Figure 4.1 Summary of the data processing procedure.

4.3 Image subtraction

The initial condition (Equation 2.22) was subtracted from the 2D heat diffusion equation of the specimen (Equation 2.20) that resulted in Equation 2.24 and Equation 2.29 for the reference specimen. To reflect this subtraction, the initial image just before the start of the cyclic loading, $T_0(x, y)$ is subtracted from all recorded frames, *T (x,y,t)*. The subtracted frames are denoted θ and the subscript *ref* and *spec* are used to differentiate the reference specimen and the specimen respectively. The significance of this step is that the temperature gradient seen in the recorded frames of the specimen (Figure 4.2 (a)) due to the difference in the grip temperature and detector reflection is eliminated (Figure 4.2 (b)).

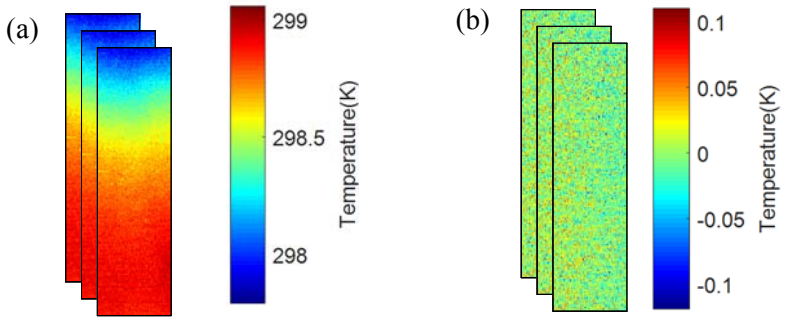

Figure 4.2 The specimen (a) before and (b) after initial image subtraction.

4.4 Spatial averaging

To derive the spatially averaged heat source the heat diffusion equation is integrated in the *x* and then the *y* direction. Integrating Equation 2.28 in the *x* direction gives:

$$\rho C\left[\frac{\partial \bar{\theta}_{spec}(y,t)}{\partial t}-\frac{\partial \bar{\theta}_{spec}(y,t)}{\partial t}_{(t=0)}\right]-k\nabla^2\bar{\theta}_{spec}(y,t)+\rho C\frac{\bar{\theta}_{spec}(y,t)}{\tau}-\frac{2h}{d}\left(\bar{T}_{en}(y,t)-\bar{T}_{en0}(y)\right) = \bar{S}(y,t)+\bar{r}_{spec}(y,t)-\bar{r}_{spec0}(y) \quad 4.1$$

where the bar represents spatial mean in one direction (*x* in this case). Integrating equation 4.1 in the *y*-direction results in:

$$\rho C\left[\frac{\partial \bar{\bar{\theta}}_{spec}(t)}{\partial t}-\frac{\partial \bar{\bar{\theta}}_{spec}(t)}{\partial t}_{(t=0)}\right]-\frac{k}{l}\int_{-l/2}^{l/2}\nabla^2\bar{\theta}_{spec}(y,t)dy+\rho C\frac{\bar{\bar{\theta}}_{spec}(t)}{\tau}-\frac{2h}{d}\left(\bar{\bar{T}}_{en}(t)-\bar{\bar{T}}_{en0}\right) = \bar{\bar{S}}(t)+\bar{\bar{r}}_{spec}(t)-\bar{\bar{r}}_{spec0} \quad 4.2$$

where the double bar represents spatial mean of both directions. Applying the integration in the *x* and *y* direction on the reference specimen (Equation 2.29) results in:

$$\rho C\left[\frac{\partial \bar{\bar{\theta}}_{ref}(t)}{\partial t}-\frac{\partial \bar{\bar{\theta}}_{ref}(t)}{\partial t}_{(t=0)}\right]+\rho C\frac{\bar{\bar{\theta}}_{ref}(t)}{\tau}-\frac{2h}{d}\left(\bar{\bar{T}}_{enref}(t)-\bar{\bar{T}}_{enref0}\right)=\bar{\bar{r}}_{ref}(t)-\bar{\bar{r}}_{ref0} \quad 4.3$$

Accordingly, each subtracted frame (θ_{spec} *and* θ_{ref}) is then averaged horizontally and then vertically. This converts the 2D maps of temperature values into a temperature – time curve. The result of spatial averaging on specimen temperature variation, $\bar{\bar{\theta}}_{spec}(t)$ and reference specimen temperature variation, $\bar{\bar{\theta}}_{ref}(t)$ are shown in Figure 4.3 (a) and Figure 4.3 (b) respectively. The spatial averaging, a form of signal averaging, increases the signal to noise ratio – i.e. reduces the noise. The evolution of the specimen temperature variation, $\bar{\bar{\theta}}_{spec}(t)$ in response to the cyclic loading is detailed in the following Section 4.6.

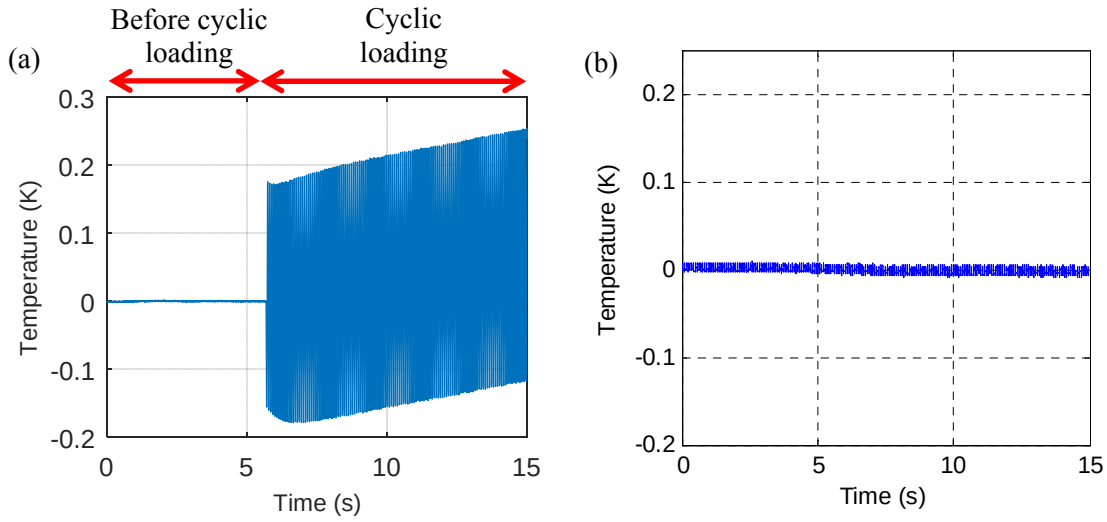

Figure 4.3 (a) spatial average of the specimen temperature variation, (b) spatial average of the reference temperature variation for $\sigma_{max} = 250$ MPa.

4.5 Correcting for environmental temperature fluctuation within the chamber

Since the evolution of the temperature of the specimen is influenced by the fluctuation in environmental temperature within the chamber, it is necessary to eliminate the effect of these fluctuations using the reference specimen temperature evolution. Subtracting Equation 4.3 from Equation 4.2 and assuming that the spatially averaged environmental temperature variation is the same on the specimen and the reference specimen (i.e. $\bar{\bar{T}}_{en}(t) - \bar{\bar{T}}_{en0} \approx \bar{\bar{T}}_{enref}(t) - \bar{\bar{T}}_{enref0}$) and the effect of the radiative reflection from the environment is also the same on the specimen and the reference specimen ($\bar{\bar{r}}_{spec}(t) - \bar{\bar{r}}_{spec0} \approx \bar{\bar{r}}_{ref}(t) - \bar{\bar{r}}_{ref0}$) results in:

$$\rho C\left[\frac{\partial \bar{\bar{\theta}}(t)}{\partial t} - \left(\frac{\partial \bar{\bar{\theta}}(t)}{\partial t}\right)_{(t=0)}\right] - \frac{k}{l}\int_{-l/2}^{l/2} \nabla^2 \bar{\theta}(y,t)dy + \rho C\frac{\bar{\bar{\theta}}(t)}{\tau} = \bar{\bar{S}}(t) \qquad 4.4$$

where $\bar{\bar{\theta}}(t)$ is the overall temperature difference between the spatial average of the specimen temperature variation and the reference specimen temperature variation given by $\bar{\bar{\theta}}(t) = \bar{\bar{\theta}}_{spec}(t) - \bar{\bar{\theta}}_{ref}(t)$.

This process is implemented in the data by subtracting the temperature variation in Figure 4.3 (b), ($\bar{\bar{\theta}}_{ref}(t)$) from Figure 4.3 (a), ($\bar{\bar{\theta}}_{spec}(t)$) to give the overall temperature variation, $\bar{\bar{\theta}}(t)$ as seen in Figure 4.4. This reduces the fluctuation and helps produce a steady temperature rise. This can be clearly observed in Figure 4.4 where the fluctuations present in Figure 4.3 (a) are eliminated.

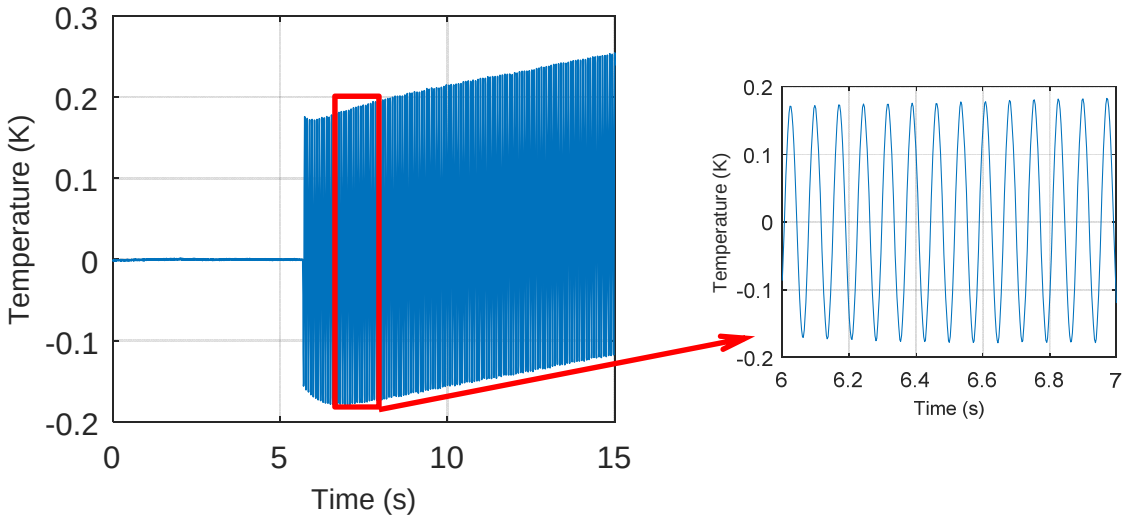

Figure 4.4 The overall temperature difference.

4.6 Extracting dissipative temperature rise

The thermomechanical heat source comprises both the thermoelastic heat source and the dissipative heat source. As mentioned earlier the thermoelastic temperature variation is cyclic and proportional to the principal stresses whereas the dissipative heat source increases the mean temperature. The overall temperature variation is the sum of both these temperature variations (Equation 4.5) i.e. $\overline{\overline{\theta}}(t)$ consists of the thermoelastic temperature variation, $\overline{\overline{\theta}}_{TE}$ and the dissipative temperature rise, $\overline{\overline{\theta}}_D(t)$ as follows:

$$\overline{\overline{\theta}}(t)=\overline{\overline{\theta}}_{TE}(t)+\overline{\overline{\theta}}_D(t) \qquad 4.5$$

This is also seen in Figure 4.4 where the overall temperature evolution consists of cyclic temperature variation superimposed on an increasing mean temperature. As the current work focuses on the dissipative heat source, the dissipative temperature rise has to be extracted from the overall temperature variation.

To obtain the dissipative temperature rise, $\overline{\overline{\theta}}_D(t)$, first the thermoelastic temperature variation, $\overline{\overline{\theta}}_{TE}(t)$ must be determined so that it can be subtracted from the overall temperature variation, $\overline{\overline{\theta}}(t)$. The thermoelastic temperature change can be obtained from the thermoelastic equation as follows:

$$\overline{\overline{\theta}}_{TE}(t)=-KT_m(\sigma(t)-\sigma_m) \qquad 4.6$$

where $\sigma(t)$ is the instantaneous stress given provided by the loading at a given point in the load cycle and σ_m is the mean stress of the loading cycle.

It is possible to obtain the load signals directly from the test machine alongside the thermal data using the camera system. However, the load signal is recorded in units of DL as opposed to N or kN. As the DL signals are proportional to the stress, $\sigma(t)$ and hence the thermoelastic temperature variation, $\overline{\overline{\theta}}_{TE}(t)$, it is sufficient to determine the constant of proportionality between the load signal and $\overline{\overline{\theta}}(t)$ instead of determining the thermoelastic constant, *K*. There is also another complication in obtaining $\overline{\overline{\theta}}_{TE}(t)$: $\overline{\overline{\theta}}(t)$ and $\sigma(t)$ do not occur concurrently, which results in a phase difference between the two quantities. The difference in phase and amplitude is illustrated in Figure 4.5 where the phase difference is labelled in the diagram and the amplitude difference can be seen from the scale of both the vertical axes. Both the load signal and $\overline{\overline{\theta}}(t)$ are fitted by using Fourier series to give the amplitude and phase of each of the signals. The ratio of the amplitude values obtained is used to calculate the constant of proportionality, whereas the phase difference is used to perform the phase correction between these signals. Once the amplitude and phase of $\overline{\overline{\theta}}_{TE}(t)$ match that of $\overline{\overline{\theta}}(t)$, $\overline{\overline{\theta}}_{TE}(t)$ can be subtracted from $\overline{\overline{\theta}}(t)$. The result of the subtraction – the dissipative temperature rise can be seen in Figure 4.6. This can then be used to calculate the dissipative heat source by using Equation 4.7.

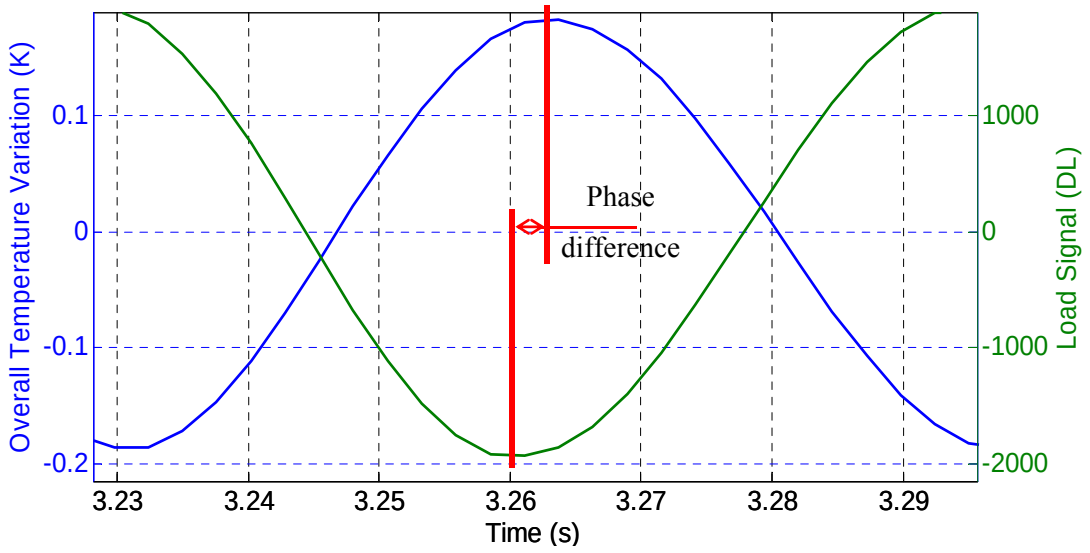

Figure 4.5 The phase difference between the load signal and overall temperature variation.

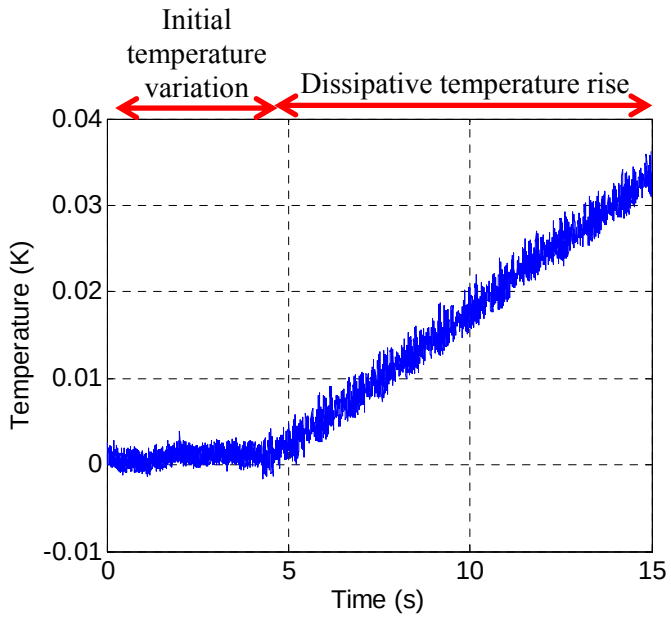

Figure 4.6 Dissipative temperature rise.

4.7 Obtaining the dissipative heat source

The dissipative heat source is determined by using the heat diffusion equation in the same way as Equation 4.4 by replacing the overall temperature variation with the dissipative temperature rise, $\overline{\overline{\theta}}_D$:

$$\rho C\left[\frac{\partial \overline{\overline{\theta}}_D(t)}{\partial t}-\left(\frac{\partial \overline{\overline{\theta}}_D}{\partial t}\right)_{(t=0)}\right]-k\int_{-l/2}^{l/2}\nabla^2\overline{\theta}(y,t)dy+\rho C\frac{\overline{\overline{\theta}}_D(t)}{\tau}=\overline{\overline{S_D}}(t) \qquad 4.7$$

where $\overline{\overline{S_D}}(t)$ is the dissipative heat source.

To obtain $\overline{\overline{S_D}}(t)$ it is necessary to evaluate the three terms on the left hand side of Equation 4.7, namely the heat rate term, the conduction term, and the convective and radiative term, as described in the following sections. The implementation of the spatial averaging method covered in the previous section and this section in Matlab can be found in Appendix A.1.

4.7.1 Heat rate term

The heat rate term is given by $\rho C\left[\frac{\partial \overline{\overline{\theta}}_D(t)}{\partial t}-\left(\frac{\partial \overline{\overline{\theta}}_D}{\partial t}\right)_{(t=0)}\right]$. The gradient of temperature rise

at time $t = 0$ (at the start of the cyclic loading), $\left(\frac{\partial \bar{\bar{\theta}}_D}{\partial t}\right)_{(t=0)}$ is subtracted from the time derivative of the dissipative temperature rise, $\frac{\partial \bar{\bar{\theta}}_D(t)}{\partial t}$ so that initial conditions such as pre-existing temperature rise could be taken into account. The time derivative of the temperature rise is obtained by performing numerical differentiation (centered finite difference) whereas the initial temperature gradient is obtained by fitting a linear least square fit of the temperature variation before the start of cyclic loading. The initial temperature gradient is evaluated this way due to the fact that there is a sharp increase in the gradient at this point and the gradient of the first five seconds would serve as a more accurate representation of the initial condition. Numerical differentiation of the temperature rise on the other hand enables the temporal evolution of the heat source to be captured. Note that the temperature change before loading has not been smoothed whereas the dissipative temperature rise has been smoothed beforehand as illustrated in Figure 4.7. Linear least square fit smoothing ensures that the noise does not affect the gradient, whereas smoothing was employed to reduce noise as numerical differentiations are highly sensitive to high frequency noise. The smoothing process acts as a low-pass filter which reduces high frequency noise. A moving average was performed on the signal three times with a window size of $2 \times n + 1$. A data point that undergoes the smoothing process is replaced by the average of the window, which consists of neighbouring n data points on both sides of the current point. This window then moves through the entire data, hence referred to as mobile window. The size of n was determined by trial and error. It was found that at $n = 75$ the noise was reduced significantly without losing accuracy. However, for the initial data points, it is not possible to apply this particular window size. The window size was gradually increased until it reaches the first n points. The effect of smoothing is also shown in Figure 4.7.

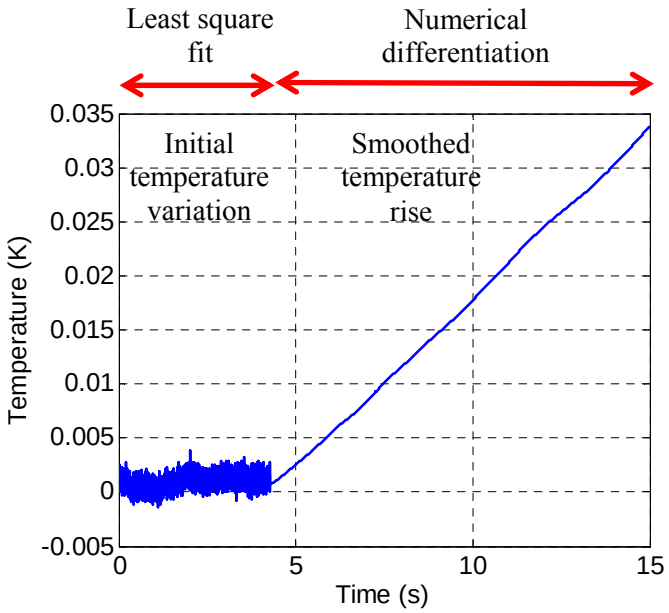

Figure 4.7 The evolution of the initial temperature variation and the smoothed temperature rise

4.7.2 Conduction term

The extent of conduction in the specimen during the experiment is taken into consideration by evaluating the level of curvature of the vertical temperature profile of the specimen. This vertical temperature variation is obtained by averaging the specimen temperature variation in the *x*-direction (see Figure 4.8). The evaluation of the Laplacian term of the vertical temperature profile gives the level of curvature. This is done by a least square approximation of the vertical profile of the temperature of the specimen using a second order polynomial. Then, the following equation is obtained:

$$\bar{\bar{S}}_{conduction}(t) = -\frac{k}{l}\int_{l}\frac{\partial^2\theta}{\partial x^2}dy = -kY_{dy^2} \qquad 4.8$$

where Y_{dy^2} is the second derivative of the second order polynomial.

The vertical temperature profile is affected by both spatial and temporal noise. The spatial noise was reduced when the previous spatial curve fitting was performed (Figure 4.8) whereas the temporal noise was reduced by smoothing the Laplacian terms of each frame plotted against time (Figure 4.9). The smoothing parameters are exactly identical to the procedure described in the 'Heat rate term' section.

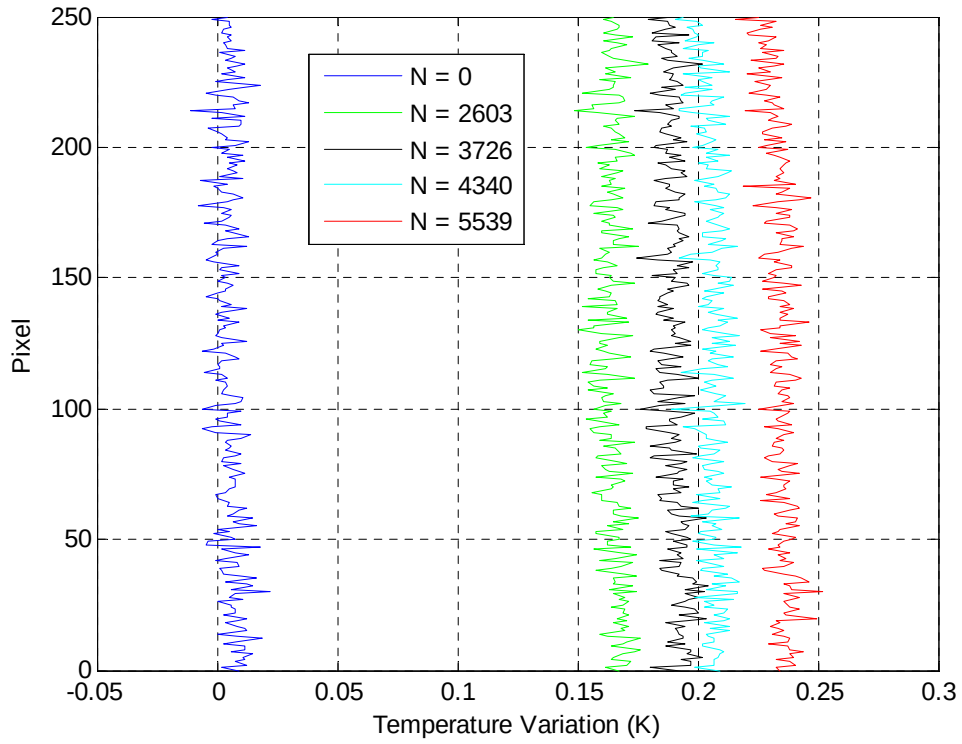

Figure 4.8 Vertical temperature profile of the specimen at different frames during the experiment.

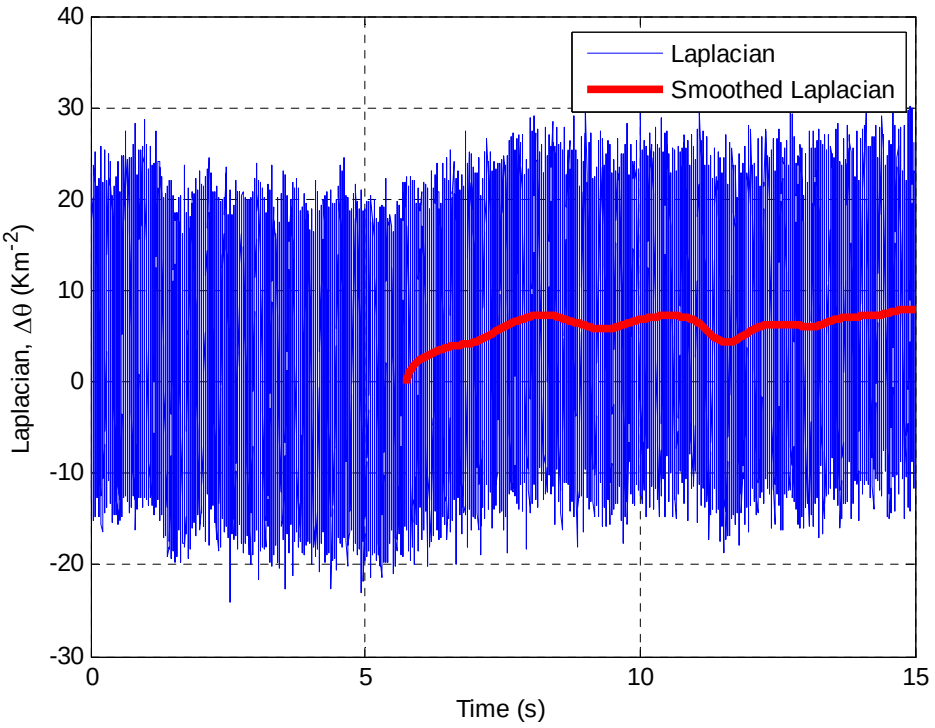

Figure 4.9 Temporally smoothed Laplacian operator.

4.7.3 Convective and radiative term

Calculating the time constant for convective and radiative heat exchange from Equation 2.24 is difficult as quantities like the convective heat transfer coefficient are difficult to measure. Instead, τ (from Equation 4.7) can be estimated from a cooling curve of the reference specimen. By assuming that the radiative reflections are zero and that there is no change in the air temperature, the energy balance of the reference specimen can be written as:

$$\left[\frac{\partial \bar{\bar{\theta}}_{ref}(t)}{\partial t} - \frac{\partial \bar{\bar{\theta}}_{ref}(t)}{\partial t}_{(t=0)}\right] + \frac{\bar{\bar{\theta}}_{ref}(t)}{\tau} = 0 \qquad 4.9$$

which has the following solution:

$$\bar{\bar{\theta}}_{ref}(t) = \tau\left[\frac{\partial \bar{\bar{\theta}}_{ref}(t)}{\partial t}\right]_{(t=0)}\left(1-\exp\left(\frac{t}{\tau}\right)\right) = A\left(1-\exp\left(\frac{t}{\tau}\right)\right) \qquad 4.10$$

where A and τ are constants. By fitting the cooling curve to an exponential function of the above form, τ can be found.

The cooling curve of the reference specimen was obtained by heating the reference specimen to about 50 ˚C in an oven and recording its temperature drop as soon as it is placed in the chamber (see Figure 4.10). The recording was done at 5 Hz for 400 s. The resulting cooling curve was then fitted

by an exponential function. The time constant was then determined as the coefficient of the exponential decay function. This time constant depends on the material used as well as the environmental temperature. While 316L stainless steel is used throughout this work, the experiments were conducted at different times of the year and hence different room temperatures, so the time constant is evaluated once each day the experiments are performed. The time constant typically ranges from 180 s to 220 s for the experiments conducted since the environmental

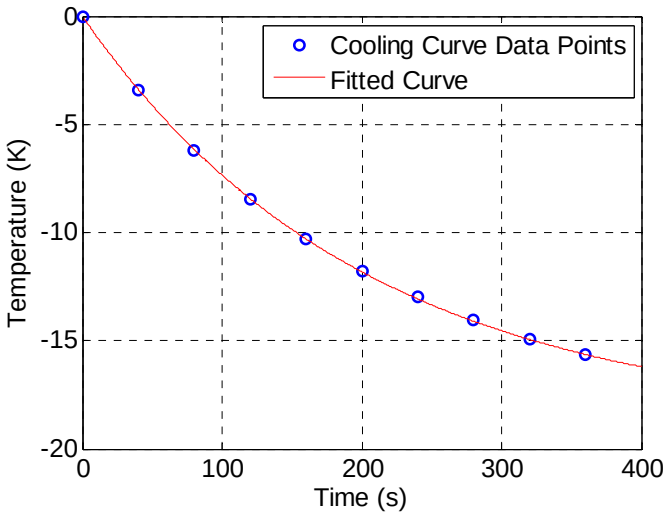

Figure 4.10 The cooling curve fitted by an exponential function.

4.8 Detection threshold

In this study, the detection threshold or noise floor is defined as the threshold above which the results have a confidence level of 95%. Various factors affect the detection threshold like: the assumptions made, the noise from the infrared detector, background radiation and etc. Therefore, the detection threshold is identified in such a way that all these factors are taken into account in a single measurement.

Using the experimental set-up described in the previous chapter and a homogeneous strip specimen, the detection threshold was determined by recording the data without applying the cyclic load. Here, the dissipative heat source is not activated so any temperature variation is caused by the detector noise or thermal exchanges with the surroundings. In the experimental set-up it is assumed that both the specimen and the reference specimen experience the same thermal exchanges with the surroundings, so in subtracting one from the other in theory the temperature variation is zero. However, an ineffective setup (i.e. gaps in the chamber, significant fluctuation in environmental temperature) will invalidate the assumption. Figure 4.11 shows a comparison between a poor and good set-up. In Figure 4.11 (a) the data was obtained from a set-up where there were gaps in the chamber which means the reference specimen and the actual specimen are exposed to different levels of thermal radiation from outside the chamber. It can be seen that the subtraction of the specimen

temperature variation from the reference specimen temperature variation in this case does not result in a zero value and although the scatter is reduced the final result is a decrease in temperature with time. With a better setup (i.e. no gaps in the chamber), a result very close to zero can be obtained as shown in Figure 4.11 (b).

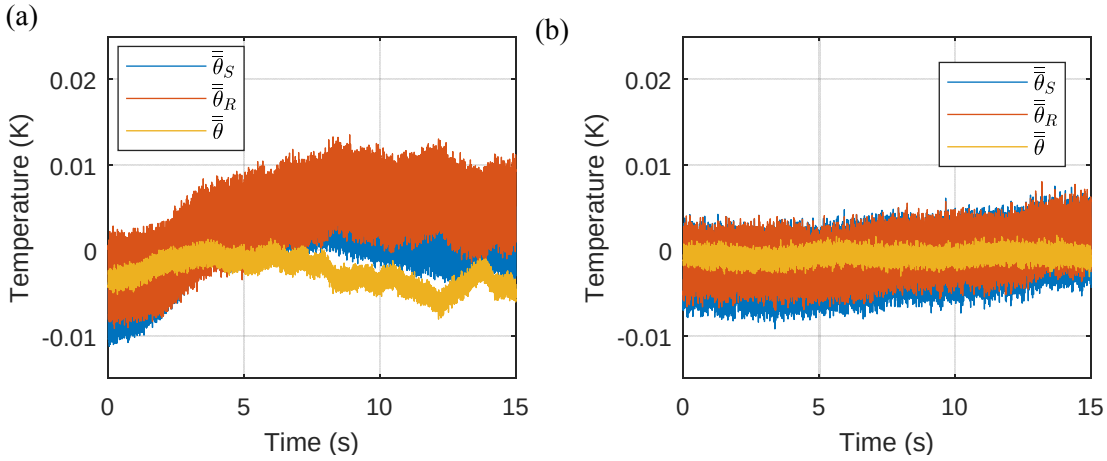

Figure 4.11 Temperature variations observed in a: (a) poor setup (b) good setup.

These temperature variations shown in Figure 4.11 (b) were subsequently processed with the same method detailed in Section 4.3 to Section 4.8. The mean and the standard deviations of the resulting heat source was calculated for the three sets of data collected and is shown in Figure 4.12. The two standard deviations give the detection threshold above which all measurements have a confidence level of 95%. The red lines show the two standard deviation level. As the heat source computed is random, positive and negative two standard deviations are calculated. Since the standard deviation is not time dependent it was averaged to provide a single value. Any heat source value that lies above this level has a confidence level of 95%. When divided by ρC (density and specific heat capacity), a detection threshold is obtained in terms of heating rate. The detection threshold in terms of heating rate corresponds to 0.72 mKs^{-1}. This implies that, in a period of one second, the combination of the thermographic measurement and data processing method has a noise equivalent to 0.72 mK.

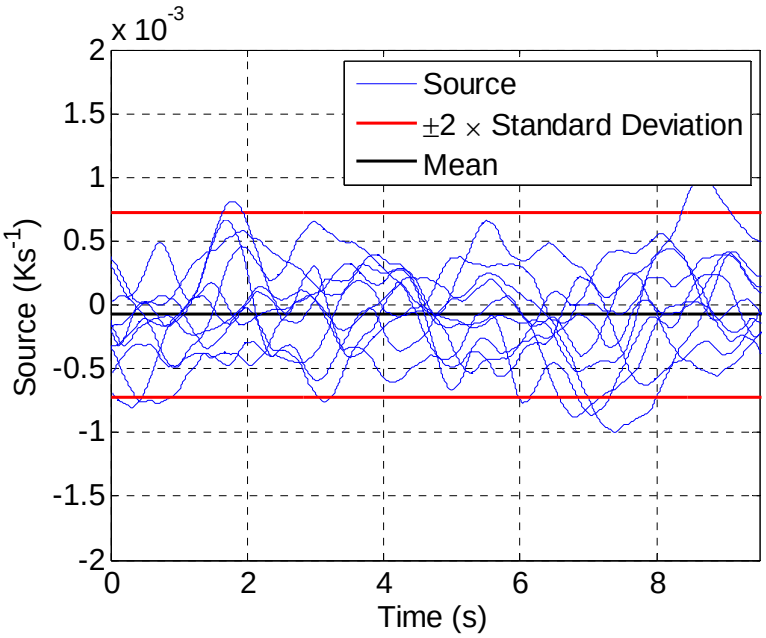

Figure 4.12 Heat source evolution due to noise.

4.9 Verification of the heat sources

The evolution of the heat source is dependent on the cyclic loading regime and as such it can be grouped into two general categories: the fully elastic cyclic loading and the elastic plastic cyclic loading. Knowing that the 0.2% offset yield strength of the 316L stainless steel is approximately 290 MPa [73], fully elastic (σ_{max} = 205 MPa) and elastic plastic cyclic (σ_{max} = 350 MPa) loading was applied on a homogeneous strip specimen at a loading frequency of 14 Hz. To demonstrate further the validity of the technique, strain measurements were also acquired along with the thermal data using a strain gauge rosette with three gauges (0/45/90) mounted on the back surface of the specimen. It is noteworthy that, in [6] it was established that the use of strain gauges does not affect the detection threshold of the thermal measurement. Even if there is a heating effect caused by the strain gauge, it is likely to be consistent throughout the test and hence eliminated by the initial image subtraction process.

Under completely elastic cyclic loading, the temperature rise that is observed is shown in Figure 4.13 (a). The temperature rise is simply linear, with minor non-linearity observed at the start of the test. The heat source shown in Figure 4.13 (b) is obtained by substituting the temperature rise to the heat diffusion equation while the detection threshold is also obtained using the same data processing procedure detailed at the beginning of this chapter. It can be seen that the heat source is essentially the gradient of the temperature rise. The non-linearity observed at the start of the test is reflected in the heat source as a sharp increase in the heat source. At lower loads, this could be attributed to the time taken for the actuator to reach the given amplitude as mentioned in Chapter 3, which typically

takes about one second. On the other hand, at moderate to high loads, micro-plastic cyclic adaptation (microscopic plasticity in the first few cycles) is thought to be the reason behind this sharp increase. The heat sources then rapidly stabilises. This constant heat source is caused by viscoelastic behaviour, i.e. reversible movement of anchored dislocations. The variation of the dissipative heat source observed is also similar to the results obtained by Maquin and Pierron [13]. This is also evident from the fact that the size of the hysteresis loop is almost constant, as seen in the stress strain data recorded simultaneously (Figure 4.14). However, attempts to compute the mechanical work, W_m or the area of the hysteresis either through direct numerical integration or measuring the phase shift have been unsuccessful due to the uncontrolled bias in the phase shift [6].

It is important to note that the magnitude of the heat source in such cases are generally very small. In this case, some of the heat source is within the detection threshold. The fact that the evolution is constant allows the heat source to be temporally averaged to obtain a higher thermal resolution. Figure 4.12 shows that the thermal resolution can be reduced to 0.05 mK.s^{-1} as indicated by the black line which is the mean of all the noise signal. Hence, the temporally averaged heat source of Figure 4.13 (b) is 1.2 ± 0.05 mK.s^{-1}.

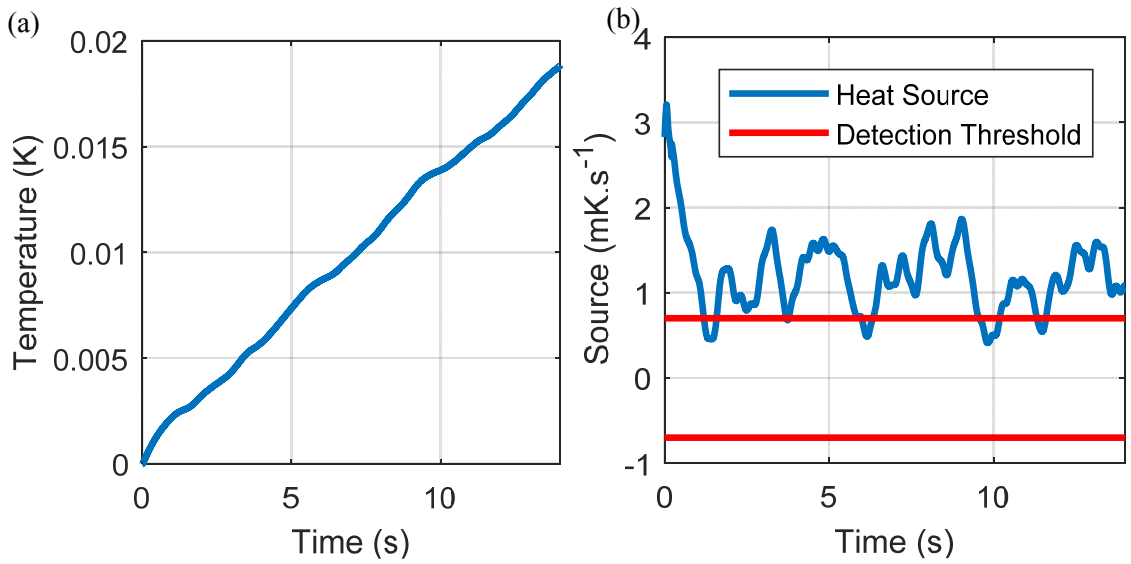

Figure 4.13 (a) Temperature rise and its corresponding heat source (b) under fully elastic cyclic loading (σ_{max} = 205 MPa).

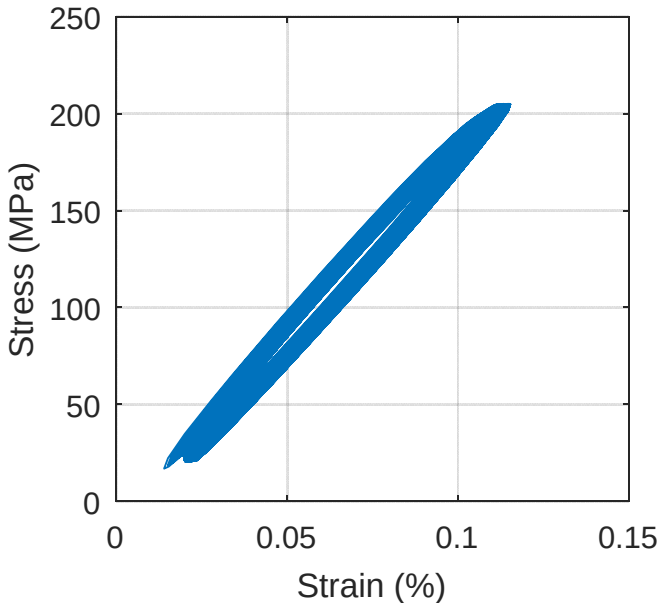

Figure 4.14 The simultaneously recorded stress strain curve of the fully elastic loading (σ_{max} = 205 MPa).

The cyclic loading applied in the case of elastic plastic loading consists of a cyclic load that has a maximum stress that is above the initial yield strength of the material. The temperature rise and the heat source evolution under elastic plastic cyclic loading is shown in Figure 4.15 (a) and Figure 4.15 (b) respectively. It can be observed that the heat source first peaks and then decreases approaching a plateau. The peak here is caused by plasticity in that the thermodynamic irreversibility arising from the creation of new dislocations increases the heat source significantly. The eventual decrease and plateauing is attributed to the hardening of the material. Once it hardens, i.e. when the yield strength increases to the value of the maximum stress applied, the material returns to the viscoelastic behaviour.

The hardening behaviour is confirmed by the corresponding simultaneous stress strain curve (see Figure 4.16). The increasing plastic strain opens up the hysteresis loop and as the material hardens the size of the loop decreases. The evolution of the source during plasticity and the eventual hardening can be verified by calculating the plastic work from the recorded stress strain evolution.

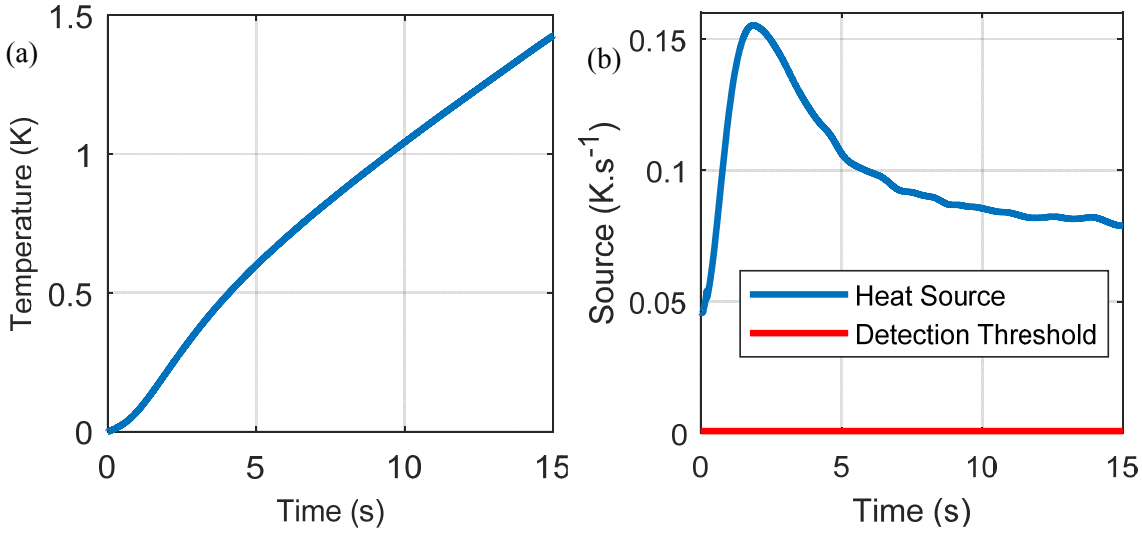

Figure 4.15 (a) Temperature rise and it's corresponding heat source (b) under elastic plastic cyclic loading (σ_{max} = 350 MPa).

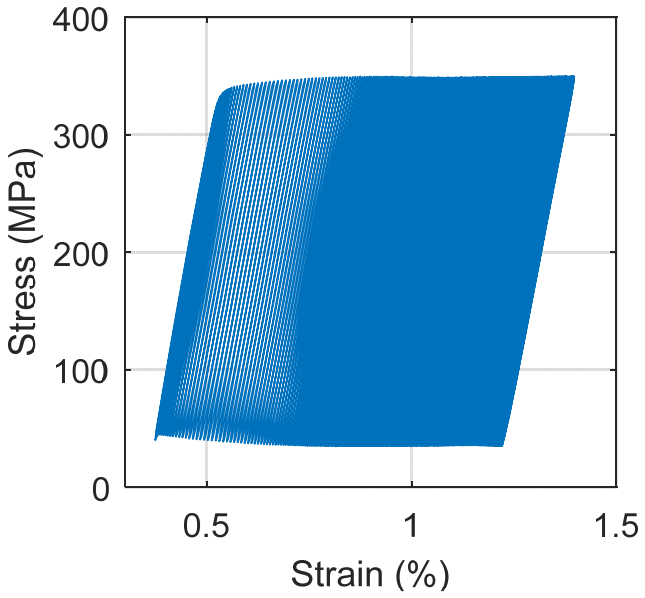

Figure 4.16 The simultaneously recorded stress strain curve of the elastic plastic loading (σ_{max} = 350 MPa).

While calculating the area under the hysteresis loop is further complicated by the fact that the loop is not closed at the beginning, the approximate plastic work per cycle can still be obtained as follows:

$$W_P^i = \int_{t_i}^{t_i+t_p} \sigma \dot{\varepsilon} dt \approx \sigma_{\max}^i \Delta\varepsilon_P^i \qquad 4.11$$

where W_P^i the plastic work in a cycle, i is the cycle number, t_i is the time at the start of every cycle, t_p is the duration or period of every cycle, $\sigma_{\max}^i$ and $\Delta\varepsilon_P^i$ are the maximum stress and increment plastic strain for that cycle respectively. The minimum strain at every is cycle is marked on the evolution

of the strain as seen in Figure 4.17 (a) and the corresponding increment of plastic strain is shown in Figure 4.17 (b). The maximum stress is indicated in the overall evolution of stress as shown in Figure 4.18 (a), and is separately shown in Figure 4.18 (b). To be able to compare the plastic work in a cycle to energy dissipated, the energy dissipated per cycle has to be first found:

$$E_D^i = \int_{t_i}^{t_i+t_p} S_D dt \qquad 4.12$$

where E_D^i is the energy dissipated per cycle. Both E_D^i and W_P^i are expressed in units of J.m^{-3}.cycle^{-1}.

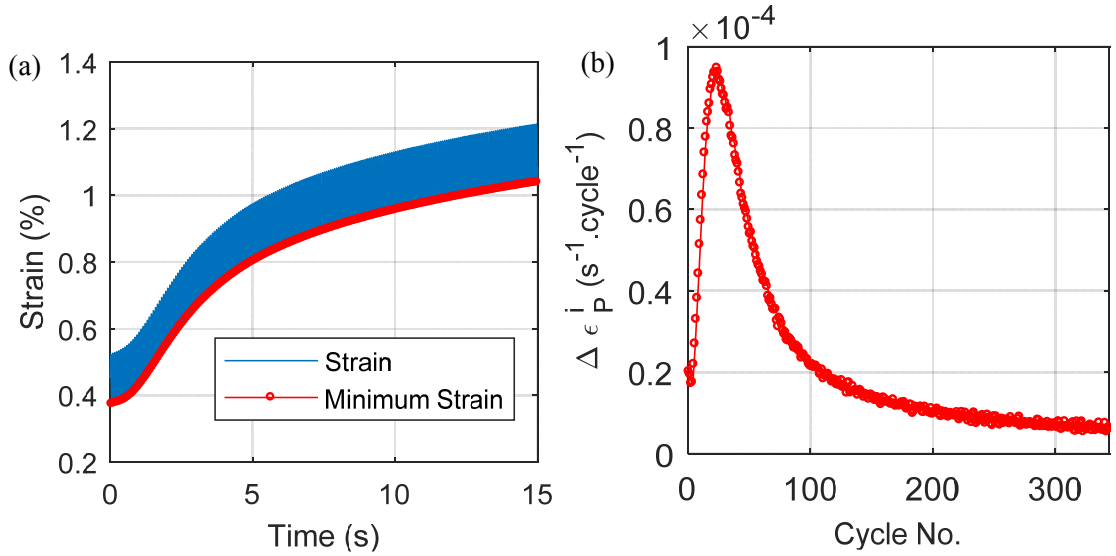

Figure 4.17 (a) the evolution of strain (b) minimum strain in a cycle.

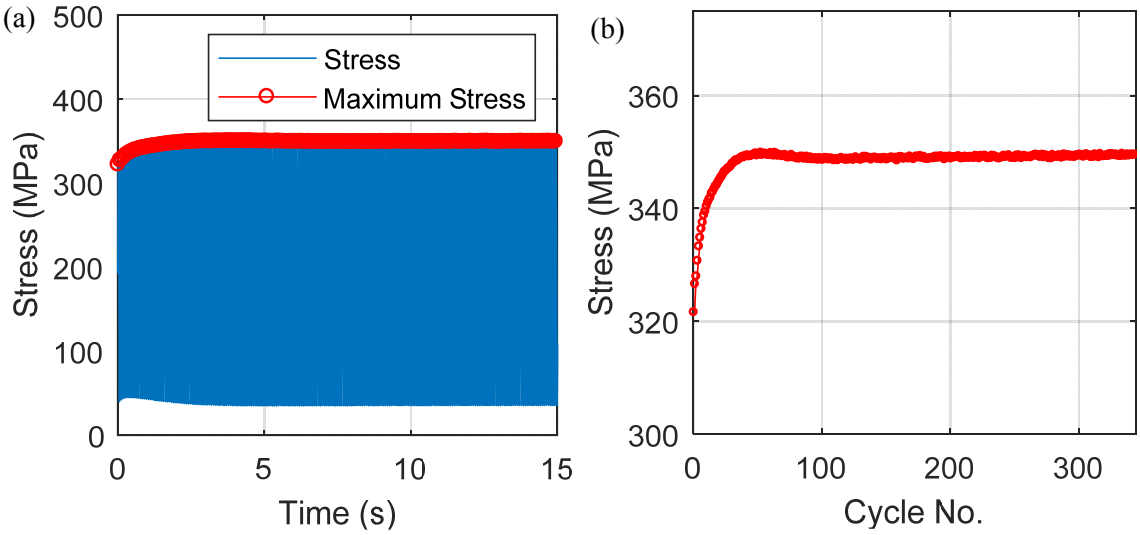

Figure 4.18 (a) The evolution of stress (b) maximum stress in a cycle.

This then enables the comparison of plastic work and the energy dissipated (see Figure 4.19). In comparing these quantities, it is important to be aware of the wider context of energy balance:

$$W_M^i = W_{VE}^i + W_P^i = E_D^i + E_S^i \qquad 4.13$$

where W_M^i is the input mechanical work. It is the sum of viscoelastic work, W_{VE}^i and plastic work, W_P^i. Equally, it is also the sum of dissipated energy, E_D^i and stored energy, E_S^i. The stored energy here refers to the energy used to modify the material microstructure, i.e. the energy used to create new dislocations. It follows that this term is only present when there is plasticity.

Figure 4.19 shows that the evolution of the plastic work and the energy dissipated is the same. This confirms that plasticity is the reason why the heat source increases rapidly. Also, it could be said that the plastic work at the start of the test and at the end of the test is very small (see Figure 4.19). As such, the amount of energy that is stored is also small. Hence, the energy dissipated at the points could be attributed to purely viscoelastic work. This then implies that the final viscoelastic work is much higher compared to the initial viscoelastic work. This increase reflects the fact that the dislocation density has increased from its initial level due to plastic straining.

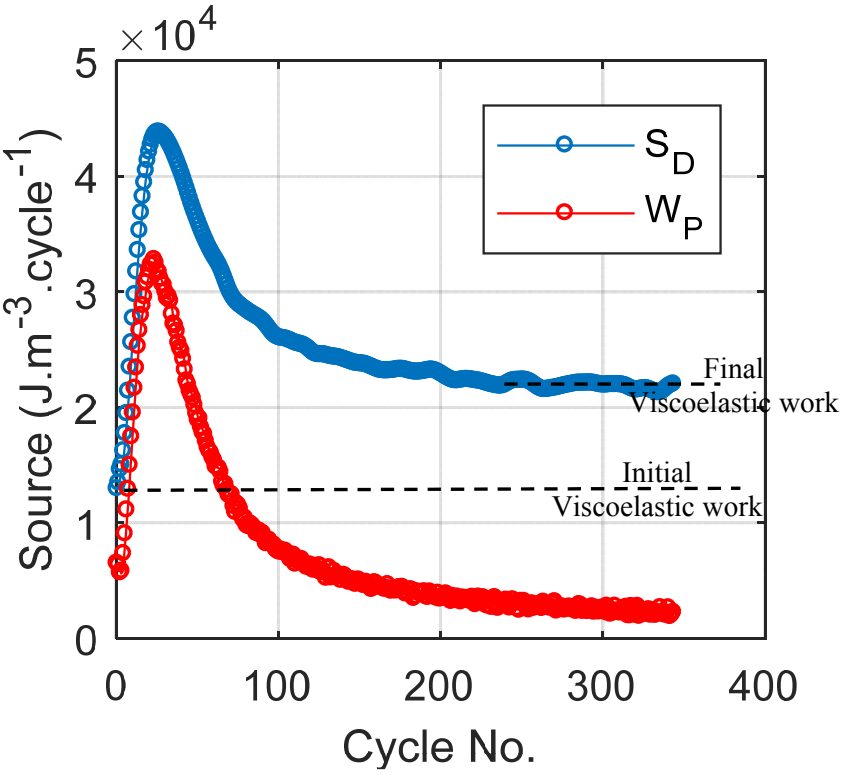

Figure 4.19 Comparison of energy dissipated and plastic work.

4.10 Summary

As highlighted in Chapters 2 and 3, the main hindrance to the calculation of the dissipative heat source stems from the fact that the intensity of the heat source is low and therefore the temperature rise is also low leading to measurement challenges. Several data processing steps are necessary to be able to extract this small heat source in conjunction with the experimental procedures detailed in Chapter 3. The work in Chapter 4 demonstrates that the data processing method described can be used successfully to obtain the spatially averaged dissipative heat source for a 316L stainless steel specimen subjected to cyclic loading.

The primary data processing step that reduces noise drastically is spatial averaging. In addition several other key steps performed as part of this procedure include smoothing and least-square fitting. These steps were all derived from the development of the spatially averaged heat diffusion equation from the 2D form of the heat diffusion equation (Equation 2.28 and 2.29). The temperature variation obtained from the experiment is subjected to data processing methods discussed above to give a smooth temperature rise. This temperature rise is then used to calculate the spatially averaged dissipative heat source using the spatially averaged heat diffusion equation.

In achieving a low detection threshold of 0.7 $mK.s^{-1}$, it was confirmed that the combination of experimental setup and data processing procedure were indeed effective, which enabled the identification of very small dissipative heat sources. The effectiveness of the procedure was demonstrated using two examples of dissipative heat source under fully elastic and elastic plastic cyclic loading. It was found that the dissipative heat source under fully elastic cyclic loading caused by the reversible movement of dislocations was of low intensity, almost comparable to the detection threshold established. However, the dissipative heat source, under elastic plastic cyclic loading caused by the irreversible movement of dislocations, was generally much higher in intensity. The work described in the present chapter enables the investigation of the effect of microstructure on the dissipative heat source described in the following chapter.

5 Effect of microstructure on energy dissipation in 316L stainless steel

5.1 Introduction

While it has been shown that the dissipative heat source is sensitive to microstructural evolution [5], it does not necessarily mean that the dissipative heat source can identify different microstructures. In other words, it has been shown that the energy dissipated can detect the evolution of microstructure (i.e. increase in energy dissipated with dislocation density) within a single specimen but it is yet to be established whether energy dissipated could also differentiate specimens of different initial microstructural state. This can only be established by obtaining the dissipative heat source from a range of known microstructures. Therefore an experimental investigation was carried out to demonstrate the possibility of detecting different microstructural states through the measurement of energy dissipation. It was established in Chapter 4 that the spatial averaging procedure allows very small heat sources to be measured in specimens subjected to a uniform stress. Hence strip specimens of the type described in Chapter 3 and used in Chapter 4 were produced with a range of different microstructures using heat treatments. It is envisaged that the understanding of the effect of individual microstructures on dissipative heat source will serve as a precursor to the use of dissipative heat source as tool for microstructural assessment of heterogeneous microstructures, i.e. a weld joint.

A range of different microstructures of 316L stainless steel were generated by heat treatment, which mainly modified the dislocation density in the materials. The heat treatment method and the resulting microstructure and mechanical properties are detailed in Section 5.2. The only existing similar work is that of Fan *et al.* [74] where the fatigue strength of the heat treated FV520B stainless steel was assessed by the evolution of its temperature measured using infrared thermography. It was found that the fatigue life of the material improved after a series of heat treatments. As the slope of the initial temperature rise was different for different specimens, it could be inferred that the energy dissipated is also different. However, a range of microstructures need to be tested to fully establish this. Also, the main difference here is that the heat treatments in this work were conducted to modify the microstructure as opposed to residual stress relief or hardening. While their results show that different microstructures produce different temperature rise, the exact extent of the effect of microstructure on energy dissipation is unclear. As such, the effect the microstructure has on the dissipation has been the focus and more than just one alternative microstructure was produced for the work described in the chapter.

As the dissipative source is activated at stress levels approaching and above the yield strength of the material an important part of the study is to determine how the heat treatment affects the mechanical properties, so a section is devoted to this. The dissipative heat source for a range of cyclic loading

below the macroscopic yield strength of the respective microstructure was examined. These specimens were then cyclically hardened after which the same cyclic loading was applied again. The effect of the cyclic hardening is also presented.

5.2 Heat treatment procedure

The aim of the heat treatment in this work is to modify the microstructure of the as received 316L specimens, and the dislocation density in particular. These heat treatments were carried out in a Carbolite Gero TZF 1200 tube furnace connected to a vacuum pump. The vacuum was essential in preventing the surface from oxidising as oxide layers can hinder imaging. To generate a range of microstructures, AISI 316L stainless steel strip specimens of dimension 250 mm × 20 mm × 2 mm (described in chapter 3) were heated to different maximum temperatures. The specimens were heated at a heating rate of 200 ˚C.hour^{-1} to a certain elevated target temperature. From the elevated temperature the specimens were control-cooled to room temperature so as to avoid shape distortions in such thin specimens. One of the limitations of the tube furnace is that only the central zone (approximately 300 mm in length) along the length of the tube is heated. Moreover, the diameter of the tube is only 50 mm. As such, the specimens were heat treated one at a time.

The temperature calibration and the accuracy of the heating and cooling operation performed in the furnace was monitored using a thermocouple placed at the central zone of the tube. The furnace was heated at a constant rate of 200 ˚C.hour^{-1} to a target temperature of 1050 ˚C and cooled at two different cooling rates: 200 ˚C.hour^{-1} and 100 ˚C.hour^{-1}. It was found from the temperature recorded during these heat treatments (see Figure 5.1) that the heating rate was accurate, as well as the target temperature remaining stable. However, at higher cooling rates, owing to the design of the control system that seeks to stabilize the temperature along the length of the furnace tube, the cooling rate was unintentionally slowed down. Therefore, the cooling rate was maintained at 100 ˚C.hour^{-1}. It is important to note that inconsistencies in heating and cooling rate could alter the exposure time at elevated temperatures which can then cause variation in microstructure. By ensuring that the target temperature was stable and the heating and cooling rate consistent, the variability in heat treating one specimen at a time is minimised.

The dislocation density of the as received material was reduced by heating the material to elevated temperatures for a duration of time. Two mechanisms exist when metallic materials are annealed. The first mechanism, called recovery, occurs at lower temperatures and results in dislocations with opposite signs being annihilated and subsequently rearranged into a lower energy configuration [75]. Recovery is responsible for only a minimal reduction in dislocation density leading to only a partial residual stress relief [76]. As the material is exposed to temperatures exceeding the recrystallisation temperature, new dislocation-free grains are formed, replacing old ones. The recrystallized specimens have a dislocation density that is much lower than the original cold-rolled specimen that

has undergone the recovery process, resulting in complete residual stress relief [76]. However, the exact temperature to attain these states is difficult to determine because it is strongly dependent on the initial state. As shown by Donadille *et al.* [77], the 316L stainless steel can recrystallize at a temperature as low as 800 °C when subjected to a cold work of 40 % whereas at a lower level of cold work, i.e. 10%, a higher recrystallization temperature is required. Due to the variability in the cold rolling process [78] the exact extent of the previous deformation is difficult to determine. Hence, the temperature and dwell time of the heat treatment performed were adjusted to obtain the desired microstructure.

In the preliminary stages of this work [73], it was found that significant grain growth occurred at a temperature of 1050 °C in just 2 minutes of dwell time. This implies that recrystallisation could take place without significant grain growth at a lower temperature, i.e. 950 °C at a dwell time of 30 minutes. Grain growth was induced by elevating the target temperature further to 1050 °C. A much lower temperature of 450 °C and 650 °C with a dwell time of one hour in each case were used for the recovery process. A set of specimens having the same initial condition (referred to as 'as received' condition) was obtained. The heat treatment was then applied on these as received specimens. The heat treatment procedure is summarised in Table 5.1. Two specimens were produced at each heat treatment temperature – one for mechanical property and microstructure assessment whereas the other is used to assess the dissipative heat source. For the specimen in the as received condition, an additional specimen was used to test the repeatability of the dissipative heat source assessed.

Table 5.1 Parameters of the heat treatment for different specimens.

Heat treatment	**Temperature (°C)**	**Dwell time (hours)**	**No. of specimens**
A	As Received	-	3
B	450 °C	1	2
C	650 °C	1	2
D	900 °C	0.5	2
E	1050 °C	1	2

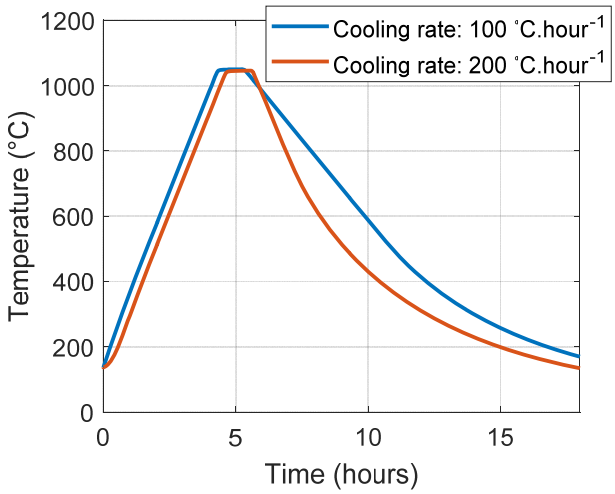

Figure 5.1 The evolution of the temperature under two different cooling rates: 200 ˚C.hour^{-1} and 100 ˚C.hour^{-1}.

5.2.1 Microstructure and mechanical properties

The microstructure and mechanical properties of specimen A – E were first established. To produce the micrographs, a small piece was cut out from each of the specimen and mounted in Bakelite resin. The mount was then ground at grit levels of 800, 1200, and 4000 on silicon carbide grinding paper and then polished using diamond paste at 6 µm and then to 1 µm finish according to ASTM E407-07 [79]. The polished specimens were then etched using a mixture of nitric acid and hydrochloric acid in a mixing ratio of 1:3 to reveal its grain structure.

The mechanical properties of the specimens listed in Table 5.1 were obtained by performing monotonic tensile tests using an Instron 8880 test machine. Strain gauge rosettes with three gauges (0/45/90) were used for strain measurement to ensure that precise measurement unaffected by strain gauge misalignments could be obtained. The strain gauge was attached to the front and back surface of the specimen. The specimens were loaded in displacement control at a strain rate of 0.0005 s^{-1} using a servo-hydraulic test machine. By averaging the front and back strains, the stress-strain curves were then plotted. As some of the stress-strain curves do not have a well-defined yield strength, the 0.2% offset yield strength was taken to be the yield strength for consistency. Young's modulus was found by a least square fit of the points between 0.1% and 0.4% of the estimated yield stress. Subsequently, the 0.2 % offset yield strength was found from the stress strain curves. It should be noted that the specimens were not tested to failure since only the yield stress and the initial hardening behaviour are of interest. Additionally, as hardness is very sensitive to both recovery and recrystallization, microhardness values were also obtained. The Vickers hardness values were measured under a 50 g load with 10 s dwell time using Matsuzawa Seiki MHT - 1 micro hardness tester. The average and standard deviation of the hardness values of 10 indents per specimen is shown in Table 5.2.

Micrographs of the resulting microstructure in each case and their respective average grain sizes are shown in Figure 5.2. As expected, the grain sizes after exposure to recovery temperatures (heat treatments B and C) were similar to the as received specimens as shown in Figure 5.2 (b) and (c). While the recovery process was not expected to alter the 0.2% offset yield strength nor the hardness, it was found from the stress-strain curves (see Figure 5.3 (a)) that the transition between elastic and plastic behaviour becomes sharper at higher annealing temperatures. This confirms that any change in microstructure is likely to originate from a change in dislocation density.

As can be seen in the micrograph (see Figure 5.2 (d)) no change in grain size has occurred after heat treatment D at 900 ˚C but the stress strain curve of the same specimen (see Figure 5.3 (b)) shows that it has a very sharp transition from elastic to plastic behaviour suggesting recrytallisation has occurred. The grain size more than doubled after heat treatment E at 1050 ˚C. Consistently the yield strength has reduced. The hardness values (see Table 5.2) confirm the reduction in strength by reducing significantly from the as received to the recrystallized states and even further in the specimen in which grain growth had occurred.

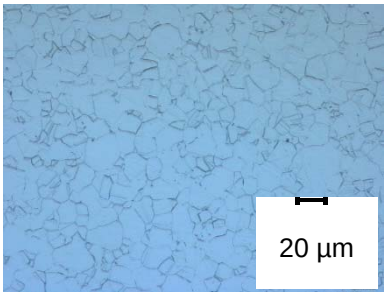

(a) A - 20.0 ± 1.8 µm

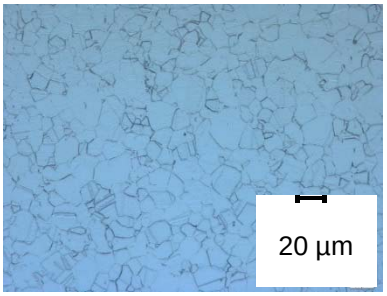

(b) B (450 °C) - 21.2 ± 5.1 µm

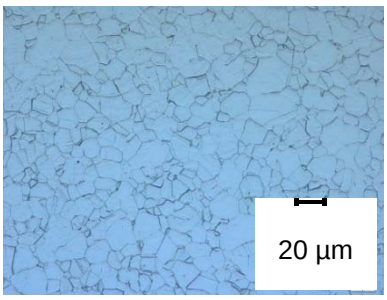

(c) C (650 °C) - 21.3 ± 5.4 µm

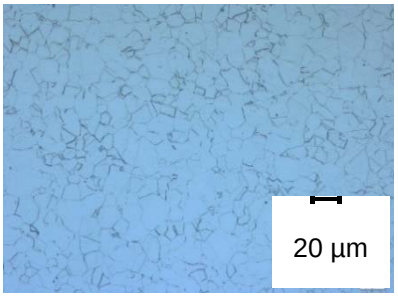

(d) D (900 °C) - 19.4 ± 4.3 µm

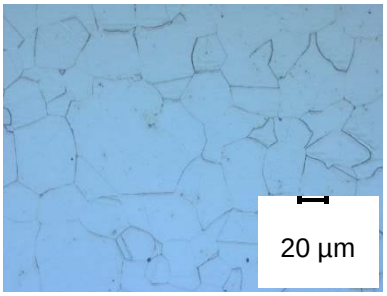

(e) E (1050 °C) - 61.2 ± 6.2 µm

Figure 5.2 Microstructure of heat treated specimens and their respective mean grain size: (a) heat treatment A, (b) heat treatment B, (c) heat treatment C, (d) heat treatment D, and (e) heat treatment E.

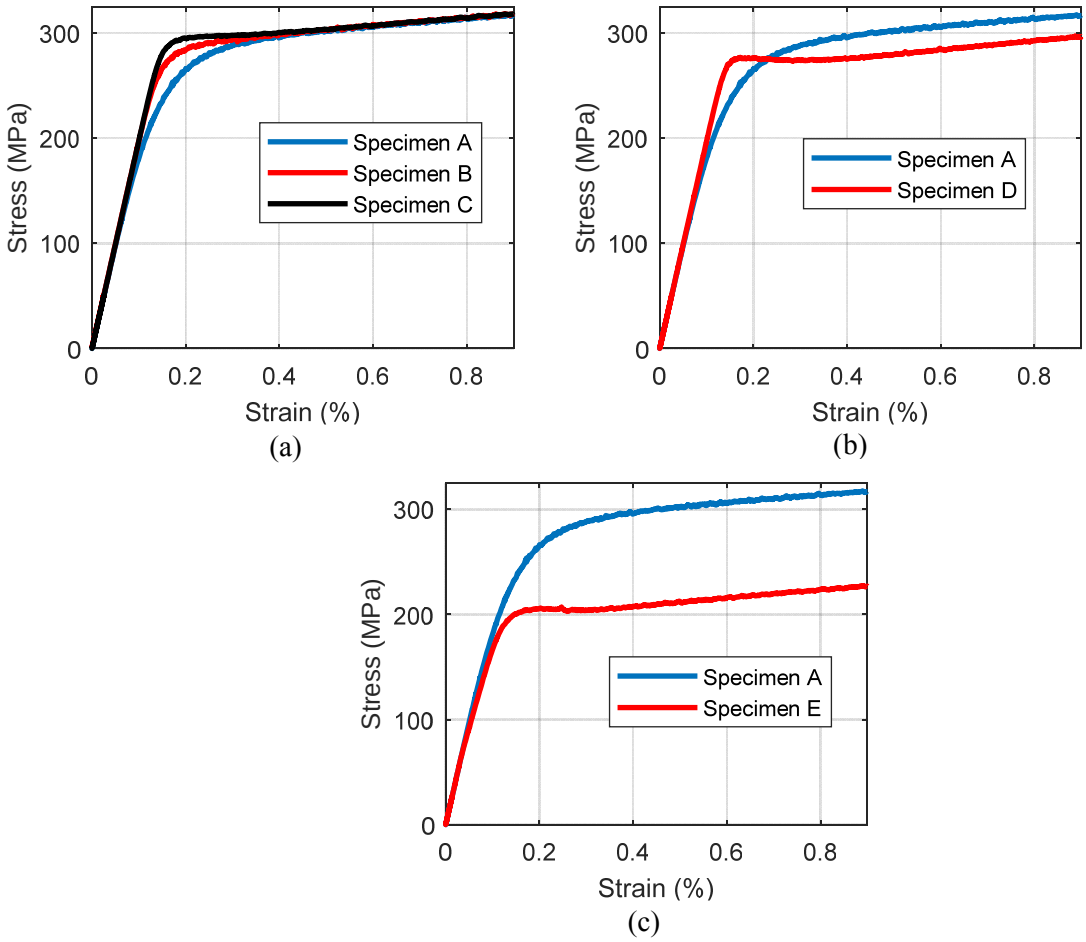

Figure 5.3 Stress strain curves of heat treated specimens compared against the as received specimen (A): (a) recovery (heat treatment B and C), (b) recrystallisation (heat treatment D), and (c) grain growth (heat treatment E).

Table 5.2 Summary of the mechanical properties for specimens A – E.

Heat treatment	0.2% Offset Yield Strength, σ_y (MPa)	Hardness (HV)	Standard Deviation (HV)
A	293	178	3.1
B	298	176	1.5
C	299	176	5.1
D	275	165	1.1
E	205	146	5.3

5.3 Results

A sequence of cyclic loading was applied to specimens A - E in Table 5.1 where the applied maximum stress level in the cycle was a fraction of the respective yield strength defined in Table 5.2. For all the specimens, stresses were applied at loading frequency of 14 Hz with a stress ratio, R_σ of 0.1. While the temperature variation of the specimen is recorded with an infrared camera set-up detailed in Chapter 3, the corresponding strain measurement is obtained using a strain gauge mounted on the back surface of the specimens.

In the case of the as received specimen, the fractions of yield strength are indicated on the stress-strain curve shown in Figure 5.4. The same fractions of yield strength were used for all specimens to give the maximum applied stress in the load cycle. Using the fractions of yield strength enables the energy dissipated at to be compared for each microstructure.

The sequence of loading is as shown in Table 5.3. The specimens are subjected to each stress level for approximately 300 load cycles (approximately 20 s) before increasing the applied stress to next level. The results from the fully elastic loading (steps 1-6 in Table 5.3) are presented in Section 5.3.1. As the cyclic loading was fully elastic, the heat source is constant over time as demonstrated in Chapter 4. As such, the temporal mean of the evolution of the spatially averaged heat source is used. The effect of the temporal mean is shown in Figure 5.5 where the spatially averaged heat source of two different tests under fully elastic loading (see Figure 5.5 (a)) is temporally averaged resulting in Figure 5.5 (b). As mentioned in the detection threshold section in Chapter 4, the uncertainty or error bar in each case is 0.05 $mK.s^{-1}$. Temporally averaging also eases comparison of results between the different specimens.

Under elastic-plastic cyclic loading (step 7 in Table 5.3) the specimen cyclically hardens. In this case, the heat source evolution is not constant and therefore the results are not temporally averaged as discussed in Section 5.3.2. Also, the plastic work during cyclic hardening is identified using strain data from the strain gauge in exactly the same way as described in Section 4.9. Finally, subsequent to hardening, the lower level stress is applied to the specimens to observe the effect of plastic straining (steps 8 – 13 in Table 5.3). The results of this post-yielding behaviour of the specimens are shown in Section 5.3.3.

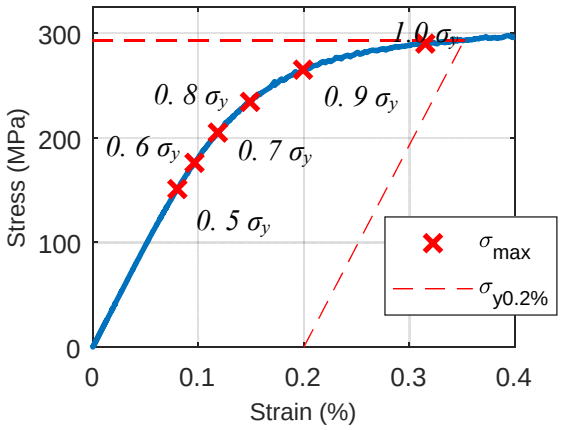

Figure 5.4 Locations of maximum stress of the applied cyclic loadings on the stress strain curve of the as received specimen.

Table 5.3 The sequence of the applied stress.

Applied Maximum Stress, σ_{max}	**Test Sequence**	
0.5 σ_y	1	8
0.6 σ_y	2	9
0.7 σ_y	3	10
0.8 σ_y	4	11
0.9 σ_y	5	12
1.0 σ_y	6	13
≈1.2 σ_y	7	

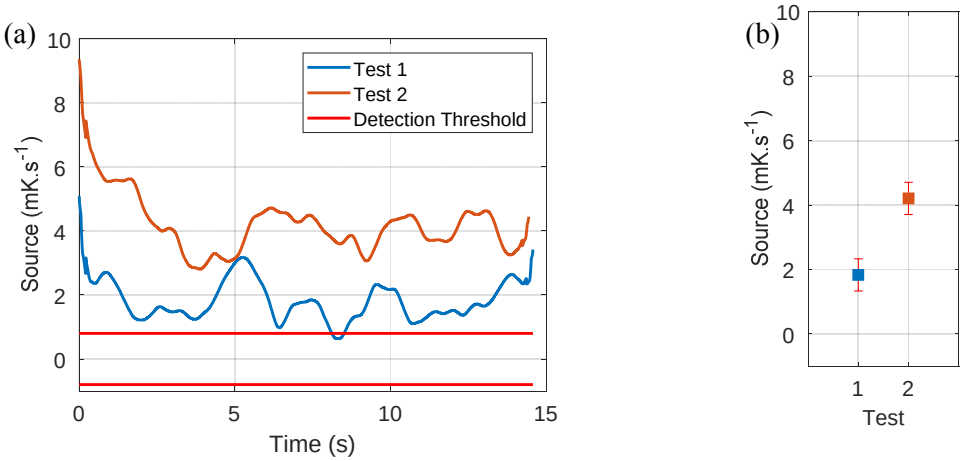

Figure 5.5 (a) Stabilised heat sources from fully elastic loading (b) temporal average of (a).

5.3.1 Effect of microstructure on energy dissipation at stress levels below the macroscopic yield stress

It is important that the variation of the heat source due to the variability in the material in the as received condition is known as that variability could then superimpose on the dissipation level of other microstructures. Connesson *et al.* [5] showed that there are inconsistencies in the heat source arising from plastically strained material of the same batch. Hence, the repeatability of this test is assessed by subjecting two as received specimens from the same batch of material to the same loading levels. Figure 5.6 shows that at all loading levels with the exception of the highest stress level, the dissipation is within the experimental error value, proving excellent repeatability. The slight discrepancy at the highest stress level could be due to the effect of the exact load applied by the test machine being slightly different. The repeatability in other specimens were not studied as the heat treatment, which is performed individually for every specimen, could induce further variability that is not related to the repeatability of the energy dissipation measurements.

It can be seen from Figure 5.6 that the energy dissipated generally increases as the stress level is increased for all the different microstructures. This is due to the fact that at higher stress level the mobility of the dislocations is higher. Figure 5.7 shows the comparison of the heat sources for the different microstructures. With the highest dislocation density, the energy dissipated by the as received specimen is the highest across all loading levels, as expected. The specimens that have been subjected to recovery dissipate less energy than the as received specimen due to a minor reduction in dislocation density whereas the dissipation in the specimens that have undergone recrystallization and grain growth is not at a measurable level except at the highest stress level close to the yield strength. However, when comparing the energy dissipated by specimen A and specimen B, where dissipation is measurable at almost all the stress levels, it can be seen that the dissipation is generally lower than the as received except at the highest stress level. This is due to the fact that, at the loading level where the maximum stress is the yield stress, both the monotonic tensile test curve for specimen A and specimen B converge (see Figure 5.3 (a)) and hence their dissipation is approximately the same.

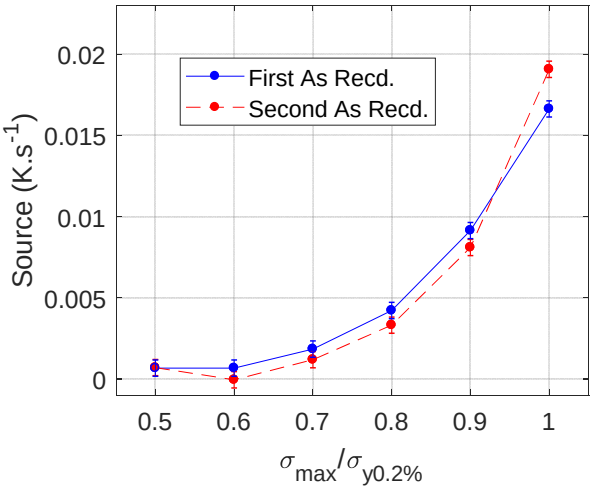

Figure 5.6 Comparison of the energy dissipated by two different specimens in the as received condition.

5.3.2 The heat source evolution during cyclic hardening

As the applied stress is increased beyond the macroscopic yield stress, strain hardening occurs. Cyclic loading is applied with a maximum stress of approximately 1.2 $\sigma_{y.}$ for specimens A – E to achieve this cyclic hardening. However, strain gauges were only mounted on specimens A, D and E and as such only these specimens are discussed in this section. The comparison of energy dissipation per cycle and its corresponding plastic work during strain hardening is shown in Figure 5.8 (a), (b) and (c) for the grain growth (specimen E), recrystallized (specimen D), and the as received specimens (specimen A) respectively. Plastic work in all the three cases is always lower than the energy dissipated due to the significant contribution from viscoelastic work. The difference between the plastic work and the total dissipated energy increases as strain hardening occurs. This is due to the fact that as the strain hardening progresses, the dislocation density increases and therefore the viscoelastic work also increases bringing the energy dissipated to a level much higher than the plastic work. The initial difference between the energy dissipated and plastic work is not noticeable for the grain growth (specimen E - Figure 5.8 (a)) and recrystallized (Specimen D - Figure 5.8 (b)), as it could be seen from its corresponding fully elastic cyclic loading results that the dissipation in those cases was generally low. The lower amount of energy dissipated is also the reason why more fluctuation (noise) can be observed in the E_D of specimen E. This is not the case for the as received specimen (Specimen A - Figure 5.8 (c)) as there is a noticeable difference in the two quantities right at the beginning. This could be attributed to the higher initial dislocation density in the as received specimen compared to the other two specimens that then causes a significantly higher viscoelastic dissipation.

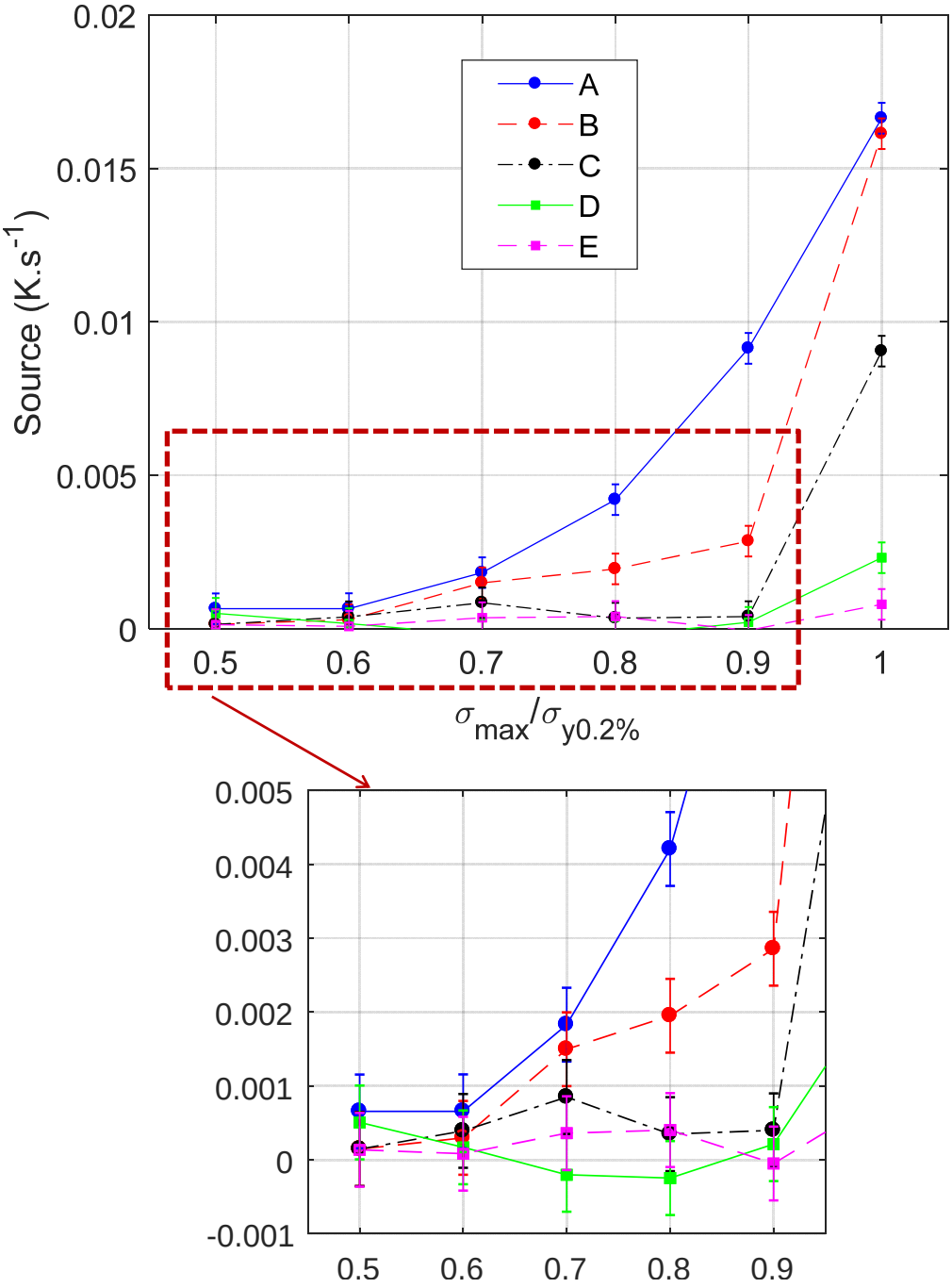

Figure 5.7 Energy dissipated at increasing stress levels below the macroscopic yield strength.

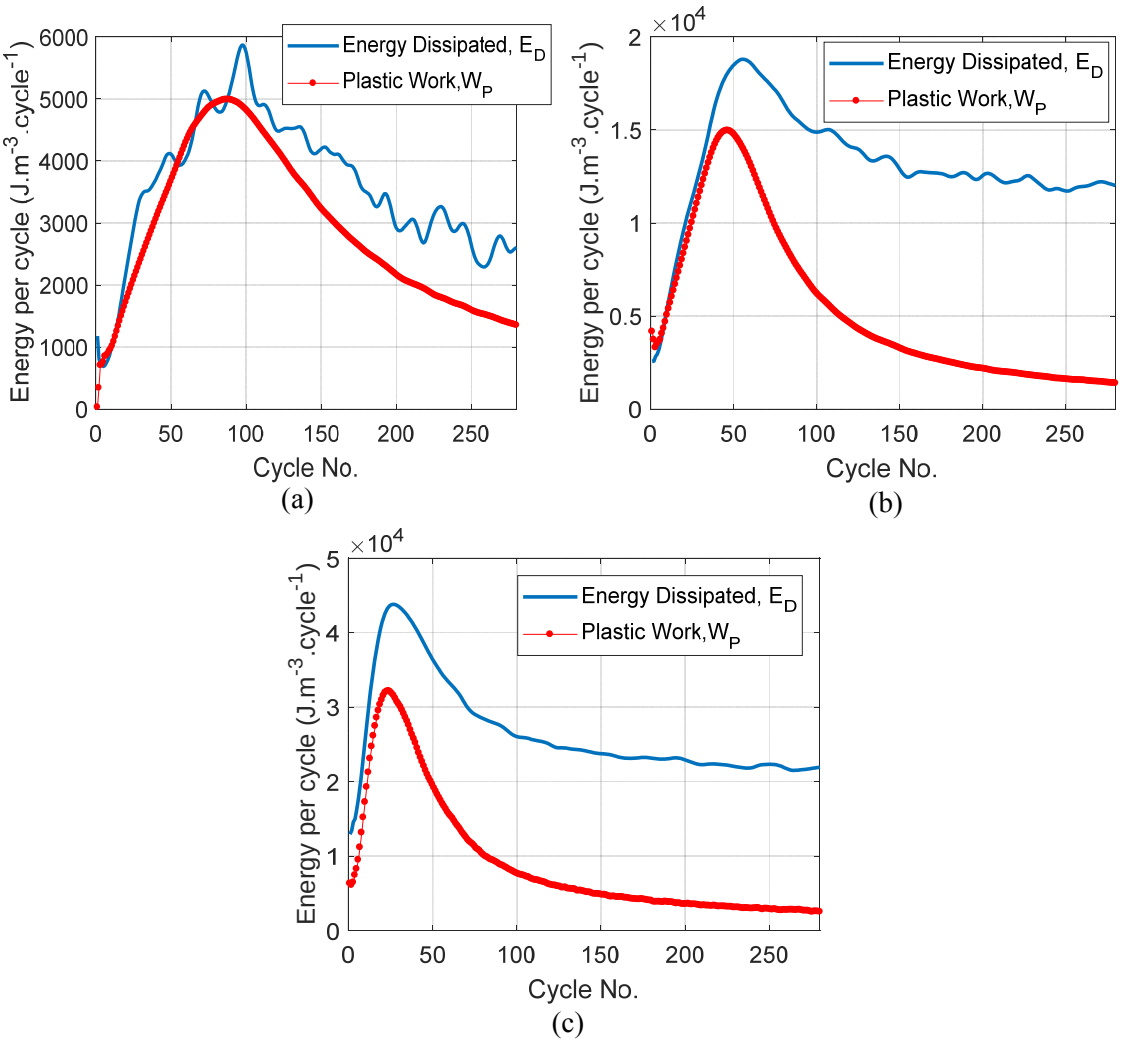

Figure 5.8: Comparison of plastic work to dissipated energy: (a) grain growth (specimen E), (b) recrystallized (specimen D), (c) as received (specimen A).

5.3.3 Post-yield heat source

Once the specimen has yielded, fully elastic loading at the same stress level as in the previous case was applied. It was found that all the specimens dissipated more due to the increase in dislocation density through plastic straining (see Figure 5.9). This is consistent with the findings of Connesson *et al.* [5].

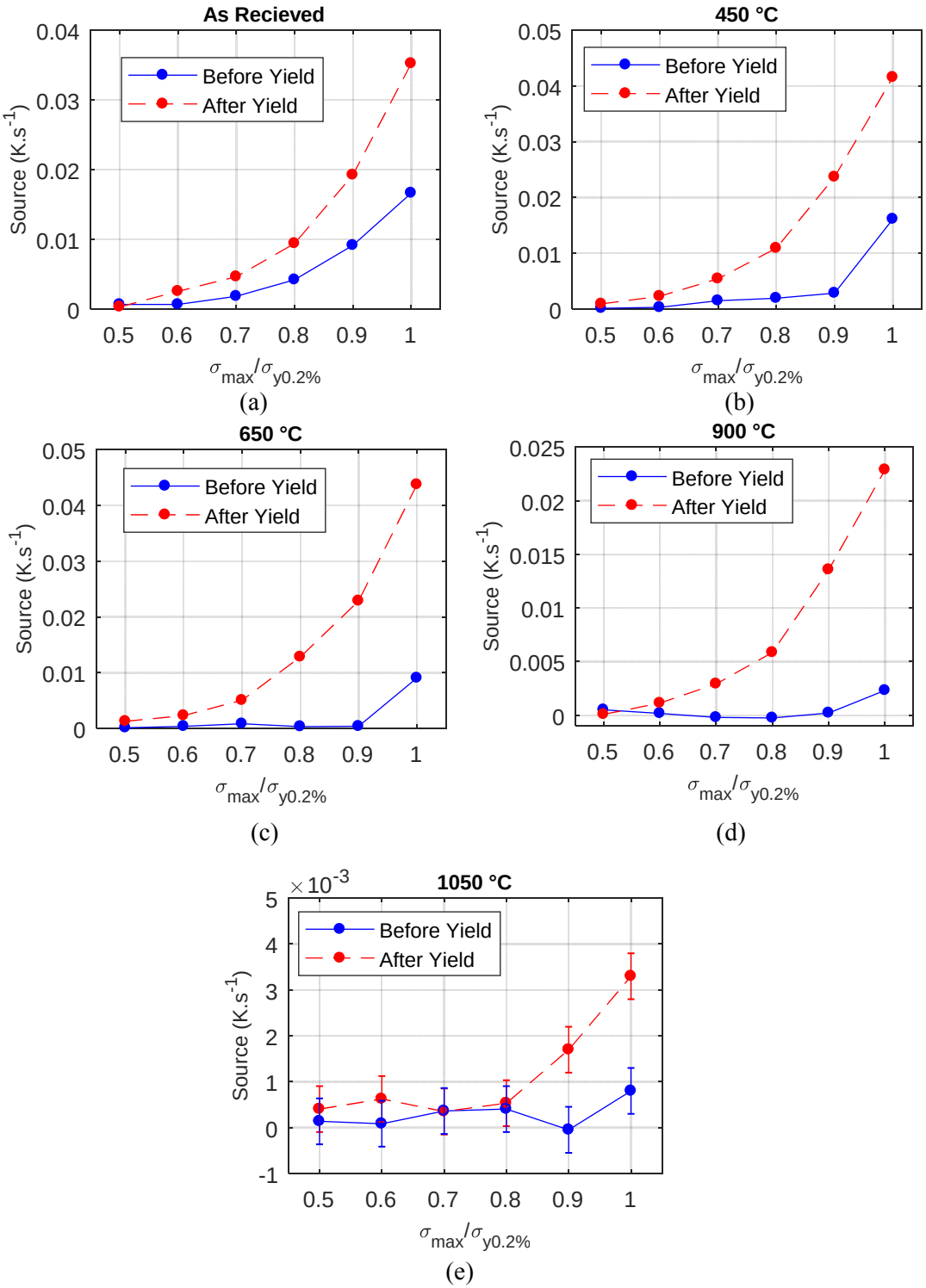

Figure 5.9 comparison between the energy dissipated before and after yielding for: (a) Specimen A (b) specimen B (c) specimen C, (d) specimen D, (e) specimen E.

5.4 Summary

The ability of the dissipative heat source to identify different microstructure has been examined. The different microstructures required for this work were achieved by devising a heat treatment procedure

that generates a range of microstructures based on the set maximum target temperature. The difference in these microstructures were established by performing microhardness test and monotonic tensile tests as well as through optical micrographs. Having successfully produced strip specimens of different known microstructures, the dissipative heat source behaviour of these specimens were examined under different stresses.

It was successfully demonstrated that with a combination of suitable experimental setup and data processing, that the energy dissipation response of different microstructures of 316L obtained through heat treatment was significantly different under fully elastic cyclic loading. These results were also found to be repeatable. The results are encouraging in that it shows that the energy dissipation could be used as a tool to assess more complex heterogeneous microstructures like that in the vicinity of a weld. However, this would require a different image processing procedure that allows the necessary improvement in thermal resolution. Developing an approach to deal with specimens with an inhomogeneous dissipative heat source is the focus of the next chapter.

6 Beyond spatial averaging: developing the image processing procedure for full-field dissipative heat source

6.1 Introduction

In the previous chapters both the stress field and the microstructure have been uniform/homogeneous across the field of view. The focus of the present chapter is to refine the image processing approach to enable specimens with a heterogeneous microstructure or stress distribution to be examined. Here, the distribution of the dissipative heat source is likely to be heterogeneous as well. As a consequence, the spatial averaging technique described in Chapter 4 is no longer suitable. In a homogeneous field, spatial averaging acts to reduce the noise enabling responses below the detection threshold of the infrared system to be identified. In a heterogeneous field, the spatial averaging serves only to provide the average value across the field and in the context of identifying small local changes in the temperature evolution resulting from changes in microstructure is meaningless. Hence, a different image processing procedure is required to extract the distribution of the heat sources over the field of view of the infrared camera.

It is important to note that the calculation of the heat source involves time derivative as well as spatial derivatives of the raw thermal data that contains noise. The derivative operation often amplifies noise significantly and therefore, a direct numerical computation of the heat source would be dominated by noise. In view of this, any implementation of the image processing procedure has to incorporate both spatial and temporal smoothing to be able to produce a reasonable result.

Here, the image processing procedure proposed by Berthel *et al.* [17] has been implemented. The procedure in [17] was developed to study heat source accompanying the fatigue process. As such, it is ideal for the current scenario since cyclic loading is used activate the dissipative heat source. A brief overview of this implementation is presented in the following section. Subsequently, the noise study carried out to determine the optimal parameters of the image processing procedure is detailed. The ability of the procedure to detecting heterogeneities in the heat source is verified with a specimen that contains an inhomogeneous stress distribution and hence produces an inhomogeneous dissipation in the infrared camera field of view.

6.2 The image processing procedure

Berthel *et al.* [17] developed a procedure to calculate the 2D distribution of the heat source based on the least square approximation of the temperature evolution over a predefined time and 2D (x-y)

space referred to as a 3D window. The approximation in both space and time also incorporates the smoothing required to identify the heat source. The 3D window is much smaller than the field of view and is swept spatially and temporally to cover the entire data set. The procedure developed in the PhD differs from that described in [17] as the influence of the environment is accounted for by subtracting the spatially averaged temperature variation of the reference specimen, $\bar{\bar{\theta}}_{ref}$, from each pixel in the frame of the thermal data of the specimen, θ_{spec}, as follows:

$$\tilde{\theta}(x,y,t) = \theta_{spec}(x,y,t) - \bar{\bar{\theta}}_{ref}(t) \tag{6.1}$$

where $\tilde{\theta}(x,y,t)$ is the data used for image processing as shown in Figure 6.1. The Matlab script developed to produce $\tilde{\theta}(x,y,t)$ is given in Appendix A.4.1.

The procedure given in [17] is particularly intended for evaluating a material undergoing fatigue, where much larger heat sources are generated, obviating the need for a reference specimen and the use of a chamber. It was described in Chapter 2, that the temporal evolution of the temperature in such cases consists of a sinusoidal variation superimposed on an increasing mean. As such, the approximation function selected for the temporal variation of the temperature, θ^{app}, is given as follows [17]:

$$\theta^{app} = p_1(x,y)t + p_2(x,y) + p_3(x,y)\cos(2\pi ft) + p_4(x,y)\sin(2\pi ft) \tag{6.2}$$

where the trigonometric terms represent the thermoelastic effect and linear terms represent the dissipative temperature rise. This is applicable to a non-linear temperature rise as well, when the time step is small and hence the temperature rise is approximately linear. The functions p_1 to p_4 are second order polynomials in x and y (i.e. spatial) as follows:

$$\begin{aligned}
p_1 &= P_1x^2 + P_5y^2 + P_9xy + P_{13}x + P_{17}y + P_{21} \\
p_2 &= P_2x^2 + P_6y^2 + P_{10}xy + P_{14}x + P_{18}y + P_{22} \\
p_3 &= P_3x^2 + P_7y^2 + P_{11}xy + P_{15}x + P_{19}y + P_{23} \\
p_4 &= P_4x^2 + P_8y^2 + P_{12}xy + P_{16}x + P_{20}y + P_{24}
\end{aligned} \tag{6.3}$$

where P_1 to P_{24} are the coefficients of the function and these parameters are dependent on the size of the window selected in space (N_x and N_y) and time (N_t) as seen in Figure 6.1.

A local coordinate system (i,j,u) centred at O (Figure 6.1) is introduced, which enables the same coordinates to be used for all windows. This new coordinate system is related to the physical coordinates (x,y,t) as follows:

$$\begin{aligned} x &= i\Delta x \quad where\ i \in \{-N_x,...,N_x\} \\ y &= j\Delta y \quad where\ j \in \{-N_y,...,N_y\} \\ t &= u\Delta t \quad where\ u \in \{-N_t,...,N_t\} \end{aligned} \tag{6.4}$$

where Δx and Δy are the spatial resolution in the x and y direction, and Δt is the time interval between successive images (i.e. 1/*f*). Accordingly, Equation 6.2 is then expressed in local coordinates as:

$$\theta^{app}(i,j,u) = p_1(i,j)u + p_2(i,j) + p_3(i,j)\cos(2\pi f u\Delta t) + p_4(i,j)\sin(2\pi f u\Delta t) \tag{6.5}$$

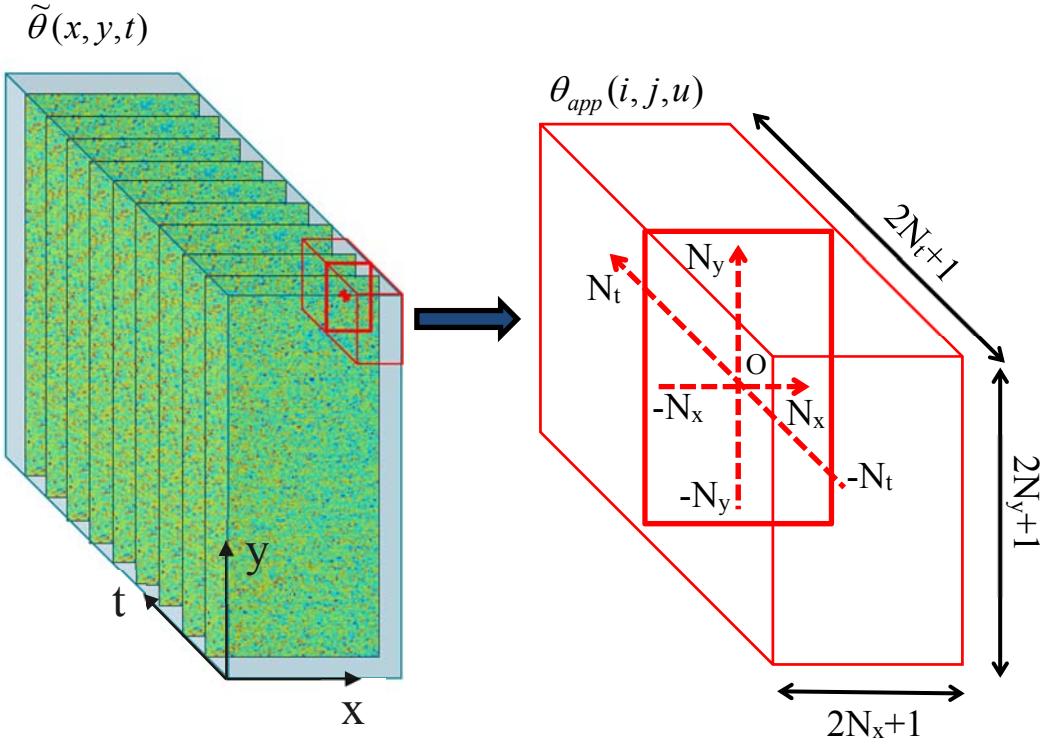

Figure 6.1 The smoothing window on frames of recorded thermal data.

The Equation 6.3 in the local coordinate system is then expressed as:

$$\begin{aligned} p_1 &= P_1 i^2 + P_5 j^2 + P_9 ij + P_{13} i + P_{17} j + P_{21} \\ p_2 &= P_2 i^2 + P_6 j^2 + P_{10} ij + P_{14} i + P_{18} j + P_{22} \\ p_3 &= P_3 i^2 + P_7 j^2 + P_{11} ij + P_{15} i + P_{19} j + P_{23} \\ p_4 &= P_4 i^2 + P_8 j^2 + P_{12} ij + P_{16} i + P_{20} j + P_{24} \end{aligned} \tag{6.6}$$

The main aim of the image processing procedure is to identify these fitting parameters. This is done by minimizing the sum of the squared difference between the approximation function and the raw thermal data within a particular window:

$$\frac{\partial}{\partial P_{1,\ldots,24}}\left[\sum_{i=-N_x}^{N_x}\sum_{j=-N_y}^{N_y}\sum_{u=-N_t}^{N_t}\left(\theta_{app}(i,j,u)-\tilde{\theta}(i,j,u)\right)^2\right]=0 \qquad 6.7$$

Expanding and rearranging Equation 6.7 results in the following form of equation:

$$M\cdot\vec{P}=\vec{B} \qquad 6.8$$

The full derivation of the equation is presented by Berthel [80] and is not given here. Essentially, the matrix *M* is a symmetric matrix formed from the approximation function and the window size and $\vec{B}$, is the product of the raw thermal data and the approximation function within the window. $\vec{P}$ represents the unknown 24 fitting parameters in Equation 6.7. The Matlab script developed to generate matrix M is given in Appendix A.4.2. As such, *M* and $\vec{B}$ can be obtained from the approximation function and raw thermal data enabling the evaluation of $\vec{P}$:

$$\vec{P}=M^{-1}\cdot\vec{B} \qquad 6.9$$

Once the parameters have been identified, those related to only the linear function can be directly substituted to the heat diffusion equation to calculate the dissipative heat source. Recalling the heat diffusion equation from Chapter 2:

$$\rho C\left[\frac{\partial\tilde{\theta}(x,y,t)}{\partial t}-\left(\frac{\partial\tilde{\theta}(x,y,t)}{\partial t}\right)_{(t=0)}\right]-k\nabla^2\tilde{\theta}(x,y,t)+\rho C\frac{\tilde{\theta}(x,y,t)}{\tau}=S_D(x,y,t)+S_{TE}(x,y,t) \qquad 6.10$$

However, using the parameters directly means that only one heat source value can be calculated per window. Hence, the value calculated represents the temporal average of the heat source at the centre of the window, i.e. point $O(x_c, y_c, t_c)$ in Figure 6.1, where the dissipative heat source at the centre of the window, $O(x_c,y_c,t_c)$ is given by:

$$\begin{aligned}\frac{S_D(x_c,y_c,t_c)}{\rho C}&=\frac{1}{\Delta t}\left(P_1\frac{I^2}{N_x^g}+P_5\frac{J^2}{N_y^g}+P_{21}\right)-\frac{1}{\Delta t}\left[P_1\frac{I^2}{N_x^g}+P_5\frac{J^2}{N_y^g}+P_{21}\right]_{(t=0)}\\&-\frac{2k}{\rho C}\left(\frac{P_2}{\Delta x^2}+\frac{P_6}{\Delta y^2}\right)+\left(P_2\frac{I^2}{N_x^g}+P_6\frac{J^2}{N_y^g}+P_{22}\right)\frac{1}{\tau}\end{aligned} \qquad 6.11$$

where $N_x^g = 2N_x + 1$ and $N_y^g = 2N_y + 1$ are the number of pixels in the window in the *x* and *y* direction, Δt is the temporal resolution, Δx and Δy are the spatial resolution in the *x* and *y* direction, and I^2 and J^2 are the sum of squares in the *x* and *y* direction i.e. $J^2 = \sum_{N_y^g} y^2$ and $I^2 = \sum_{N_x^g} x^2$.

The initial condition, $\left(\frac{\partial \tilde{\theta}(x,y,t)}{\partial t}\right)_{(t=0)}$ was calculated from the thermal data just before the test. The Matlab script implemented to calculate the full-field dissipative heat source is given in Appendix A.4.3. Similarly, the thermoelastic source at the centre of the window $O(x_c,y_c)$ could also be calculated. As the sinusoidal term is represented by both sine and cosine terms, the source arising from these terms must be calculated first:

$$\theta_A(x_c,y_c) = \omega\left(P_4\frac{I^2}{N_x^g} + P_8\frac{J^2}{N_y^g} + P_{24}\right) - \frac{2k}{\rho C}\left(\frac{P_3}{\Delta x^2} + \frac{P_7}{\Delta y^2}\right) + \left(P_3\frac{I^2}{N_x^g} + P_7\frac{J^2}{N_y^g} + P_{23}\right)\frac{1}{\tau}$$
$$\theta_B(x_c,y_c) = -\omega\left(P_3\frac{I^2}{N_x^g} + P_7\frac{J^2}{N_y^g} + P_{23}\right) - \frac{2k}{\rho C}\left(\frac{P_4}{\Delta x^2} + \frac{P_8}{\Delta y^2}\right) + \left(P_4\frac{I^2}{N_x^g} + P_8\frac{J^2}{N_y^g} + P_{24}\right)\frac{1}{\tau} \quad 6.12$$

where θ_A is the amplitude of the heat source term resulting from the cosine term whereas θ_B is the amplitude of the heat source resulting from the sine term. The overall amplitude and phase of the thermoelastic source is then given by:

$$\frac{S_{TE}(x_c,y_c)}{\rho C} = \sqrt{{\theta_A}^2 + {\theta_B}^2}$$
$$\varphi = \tan^{-1}\left(\frac{{\theta_B}^2}{{\theta_A}^2}\right) \quad 6.13$$

where φ is the phase angle. The thermoelastic source amplitude is related to the commonly found thermoelastic response, ΔT, as follows:

$$\frac{\Delta T}{2} = \frac{\left(\frac{S_{TE}}{\rho C}\right)}{2\pi f} \quad 6.14$$

To obtain a map of the heat source, the window was swept spatially by increments of 1 pixel in both the *x* and *y* direction. This is shown in Figure 6.2 (a) where it can be seen that the windows overlap. This ensures that the spatial resolution of the original thermal data can be retained. However, it has to be noted that the N_x and N_y pixels on either side of the *x* and *y* edges respectively will not be recoverable (see Figure 6.2 (b)).

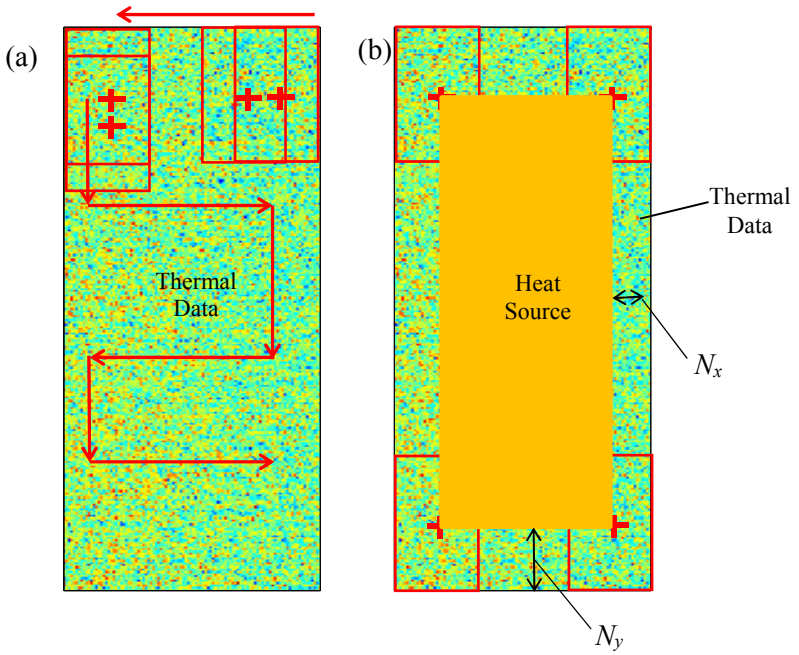

Figure 6.2(a) The direction of the spatial window sweep (b) the resulting heat source illustration overlaid on the thermal data.

Figure 6.3 shows the temporal sweeping and that there is no overlap in the time step, which is acceptable since the dissipative heat source is approximately constant in time under elastic cyclic loading. As mentioned earlier, using a relatively short time step (3 loading cycles) ensures that no overlap is needed for the elastic plastic cyclic loading where the temperature rise and hence the dissipative heat source is non-linear.

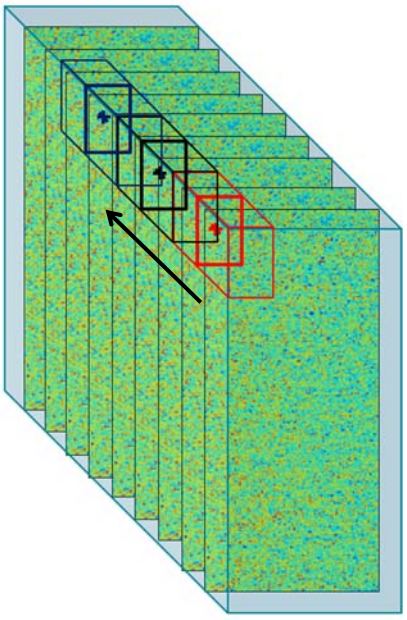

Figure 6.3 Temporal sweeping of the window on the recorded thermal data.

6.3 The Detection Threshold

It is essential to establish the detection threshold that can be obtained from the developed image processing approach. In establishing the detection threshold for the image processed results, data was acquired in the same way as described in Section 4.8 – i.e. recording the data without applying cyclic load to assess the noise. The data was acquired in DLs without NUC and then converted to temperature values as described in Section 3.4 on pixel-by-pixel calibration. As the Laplacian term involved in the calculation of the heat source is a function of Δx and Δy, the detection threshold is dependent on the spatial window size. In view of the different spatial resolutions that are used, the noise was assessed in both the high (55μm/pixel) and low (0.22 mm/pixel) resolution. In this case, the data for the high resolution measured 251 x 141 pixels whereas the low resolution measured 200 x 79 pixels. It should be noted that the size of the data does not influence the noise. It is the smoothing window parameters that are of interest in determining the detection threshold. It could be said that increasing the window size reduces the noise level due to the smoothing effect. However, an extremely large window also means that the data is overly smoothed in addition to losing more pixels at the edges. As such, the effect of various window sizes on the noise level is examined.

The effect of the temporal size of the window is quite different. For instance, in the actual data where the specimen is elastically cyclically loaded, the heat source is assumed to be constant. However, the heat rate term is not constant due to the effect of conduction. It is the conduction term that then corrects the heat rate term to produce a constant heat source. It follows that the conduction term is time dependent and so the size of the temporal window has to be as short as possible. Connesson [57] found that a window size of three load cycles provided adequate data for accurate fitting and at the same time was not affected by the time dependence of the conduction term. Hence, the temporal size of the window was fixed at 3 loading cycles (i.e. with a framerate of 350 Hz and a loading frequency of 14 Hz – 350/14 = 25 frames per cycle x 3 frames = 75 frames; $N_t = 37$).

Firstly the detection threshold for low resolution data for different window sizes was examined as shown in Figure 6.4. In all of the window sizes examined, the aspect ratio was kept to 1, i.e. $x = y$. It can be seen that as the window size is increased, as expected the spatial standard deviation decreases. Also, more data at the edges are lost when the size of the window is increased. In Figure 6.4, the size of the original data is indicated by the grey rectangle surrounding the dissipative heat source field.

However, after 51 pixels, the improvement in the detection threshold achieved does not increase significantly. Further, the window size could be extended to encompass the full width of the data. In such cases, the width of the resulting heat source reduces to one pixel. In other words, a 1D heat source is produced (as seen in Figure 6.4 when the window size is 79 x 79). This can be particularly

useful at improving the detection threshold when a large variation in heat source across the width of a specimen is not expected.

Similarly, a drop in the detection threshold as the window size is increased could be seen at higher resolution in Figure 6.5. However, for the same window size, the detection threshold increases when the spatial resolution is higher. This is attributed to the Laplacian term as when the spatial resolution is increased the spatial gradients are sharper over the physical length of the area studied. While these thresholds are specific to this data, it provides an estimate of the detection threshold for a certain window size.

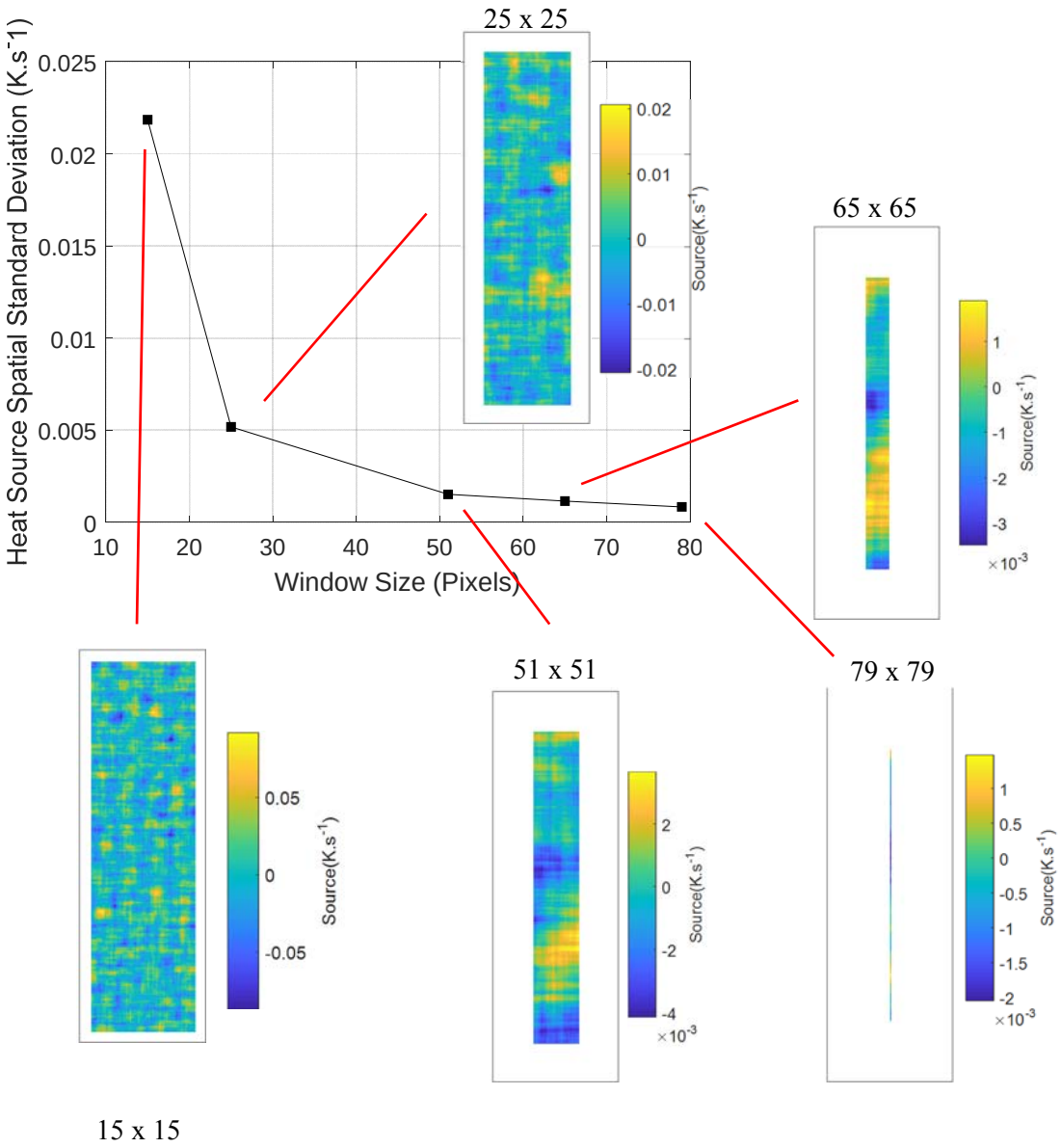

Figure 6.4 The spatial standard deviation of the dissipative heat source at low resolution.

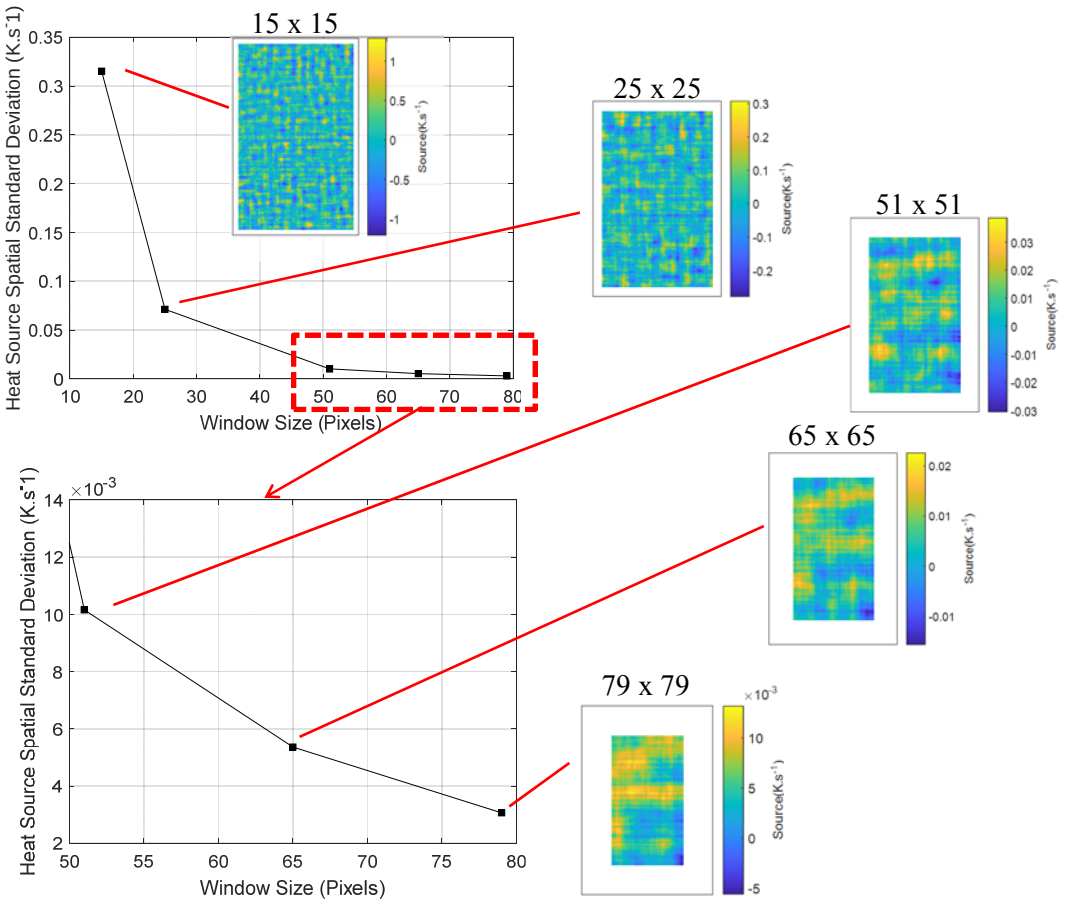

Figure 6.5 The spatial standard deviation of the dissipative heat source at high resolution.

6.4 Verification of the image processing procedure

Before examining spatial heterogeneities in the heat source, it is important to verify the implementation of the image processing technique by comparing the heat source obtained from the image processing technique with that from spatially averaged heat source, as it has a lower detection threshold. Employing a window size of 51 x 51, the data of the results shown in Chapter 4 are reprocessed using the image processing method. At this window size, the standard deviation of the spatial noise is found to be approximately 1.5 mK.s^{-1} and hence a two standard deviation detection threshold is 3 mK.s^{-1}.

A low intensity heat source below 3 mK.s^{-1}, which is measurable by the spatial averaging technique was first examined using the image processing technique. The resulting dissipative heat source field was spatially averaged and then compared to the spatially averaged heat source. The comparison of the two techniques is shown in Figure 6.6 where the dissipative heat source field at $t = 2s$, $t = 6s$, t

= *12s* is shown alongside the comparison. It was concluded that the dissipative heat source field produced was inaccurate, as the zoomed in data in Figure 6.6 shows that the heat source values obtained were negative and do not show any correspondence with the original heat sources obtained from the spatial averaging method. It is also clear in Figure 6.6 that the inconsistencies at the beginning of the test are amplified by the image processing method. This is because the heat source over the three load cycles are evaluated together, so if there is no clear trend in the heat source the least squares approximation often underestimates or overestimates the heat source.

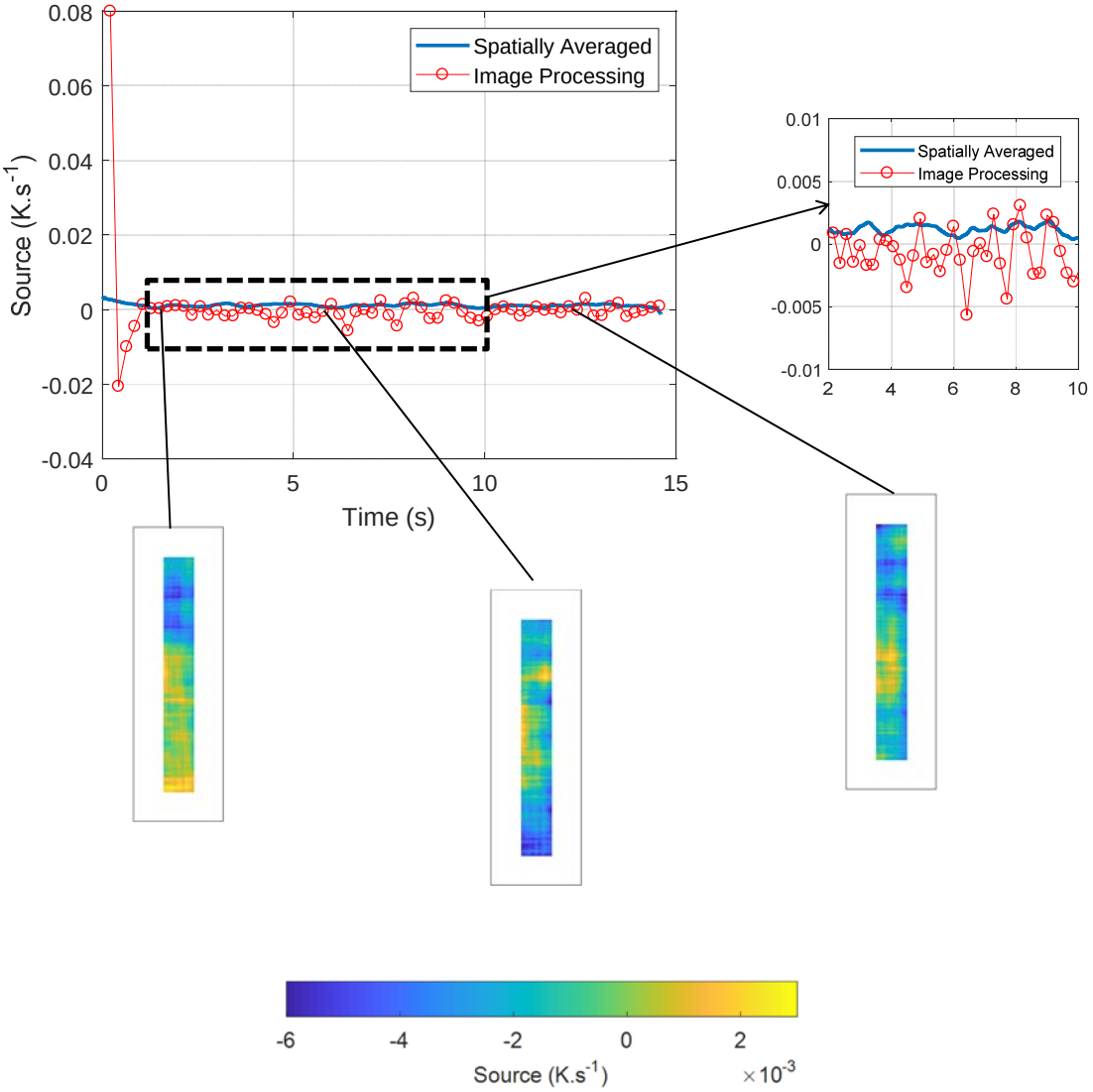

Figure 6.6 The comparison of the evolution of spatially averaged and image processed data for a lower intensity heat source.

The heat source comparison for a higher intensity heat source is shown in Figure 6.7. Due to the higher intensity of the heat source, the image processing method was able to obtain the heat sources as accurately as the spatial averaging technique. The heat source fields are also uniform, confirming

the suitability of the spatial averaging technique for a homogeneous specimen. Although, inaccuracies in the estimation of the initial heat source is significantly reduced, it is still present over the first 6 load cycles. As such, with the combination of an appropriate window size and intensity of heat source, it is possible to measure the heat sources accurately using the image processing technique.

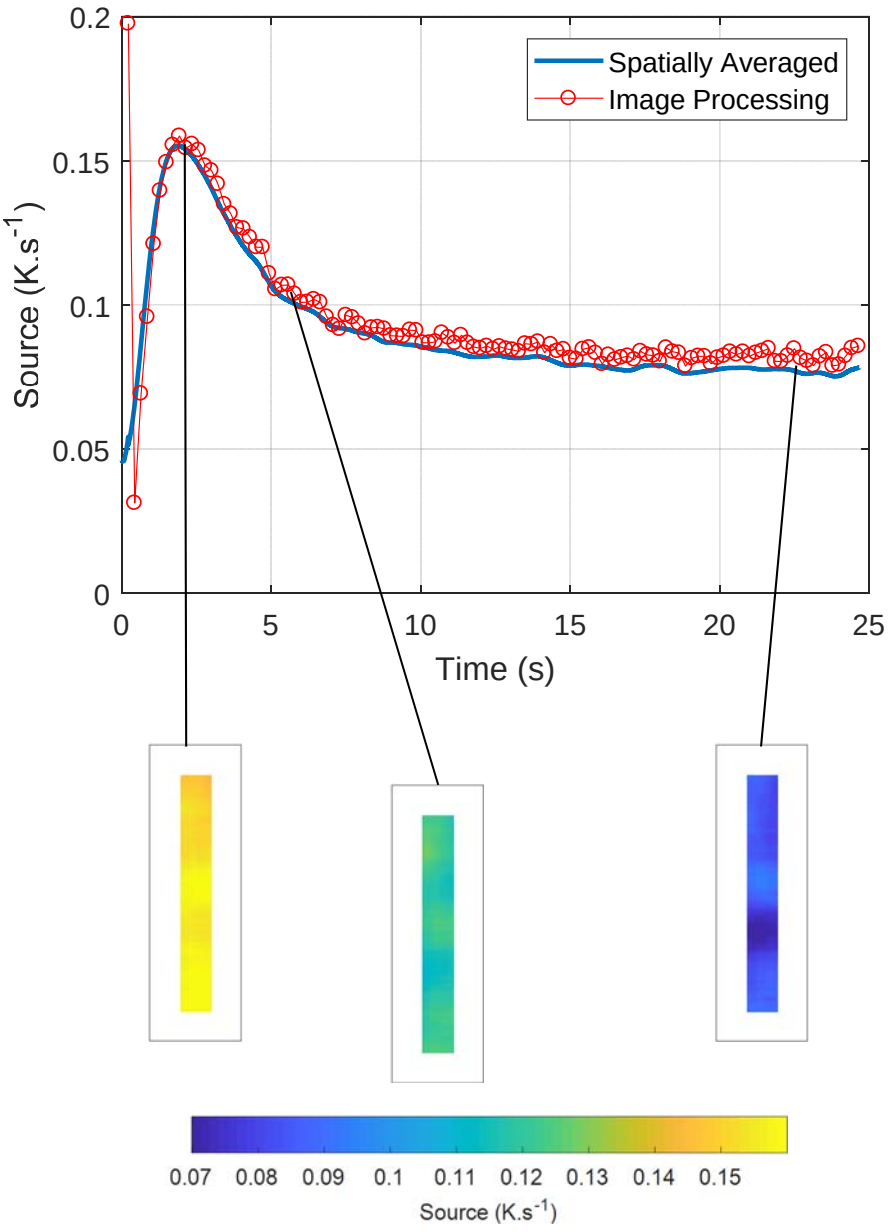

Figure 6.7 The comparison of the evolution of spatially averaged and image processed data for a higher intensity heat source.

6.5 Capturing spatial heterogeneities in the heat source

Obtaining and verifying the dissipative heat source arising from a heterogeneous microstructure is difficult. To establish confidence in the ability of the image processing method to capture spatial heterogeneities, the dissipative heat source from a known non-uniform stress field is examined. It was shown in the previous chapter that the dissipation increases as the applied stress is increased. In theory, a non-uniform stress field should have a non-uniform dissipative heat source field as well. The present section explores this using a 'hole-in-plate' specimen, which comprises a strip of material with a central circular hole loaded in tension. The initial design of the specimen is shown in Figure 6.8 (a), which is made from 316L stainless steel in the as received condition (i.e. identical to that used in the experimental work in the previous chapters). The energy dissipated in the as received condition is generally low in comparison to the detection threshold obtained from the image processing procedure. In view of this, the 'hole-in-plate' specimen was plastically strained (by applying a far field stress of σ = 350 MPa) to increase the dislocation density, and unloaded. This then increases the energy dissipated by the specimen loaded at a level below the elastic limit. This resulted in slight deformation in the shape of the hole which resulted in the dimensions given in Figure 6.8 (b).

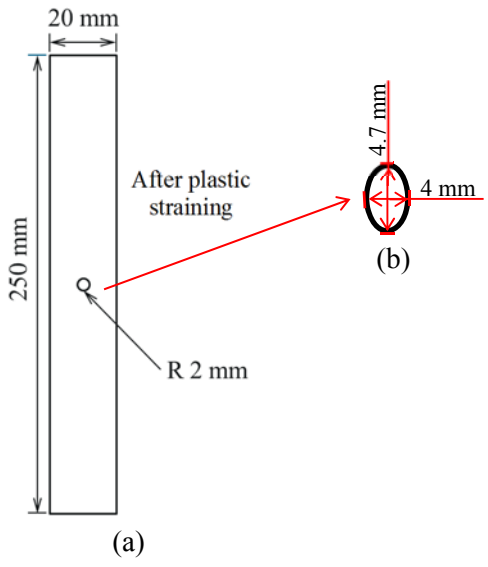

Figure 6.8 (a)The design of the 'hole-in-plate' specimen (b) the geometry of the hole after plastic straining.

Even then, a sufficiently large window size is required to capture this spatial heterogeneity. This necessarily means that the specimen has to be imaged at high resolution, increasing the number of pixels covering the specimen. A common problem encountered when imaging a cyclically loaded

specimen at high spatial resolution is the rigid body motion. The specimen moves in relation to the position of the infrared detector and this results in motion blurring, which occurs when the movement of the specimen is greater than the projected pixel size in the field of view. In a material with a uniform stress field such as those studied in the previous chapter, small motions have little effect. However, when the field of view is non-uniform, image blurring causes deleterious effects which must be eliminated. Clearly matters worsen as the spatial resolution is increased. Therefore it was necessary to implement a motion compensation procedure to each image before applying the image processing method, as described in the following section.

6.5.1 Motion compensation

The motion compensation method implemented here is similar to that of Urbanek and Bär [81] and Ummenhofer and Medgenberg [18] in that it relies on cross correlation to track the rigid body motion and interpolation to correct for the motion. Noting that the DL response of a pixel changes due to both a change in temperature and motion of the specimen, the recorded frames were first subjected to 'Laplacian of Gaussian' edge detection (see Figure 6.9). As a result, only the edges of the specimen are identified and the effect of temperature change is normalised. This also means that when the edges of the specimen are visible in the image, a tracking marker is not required.

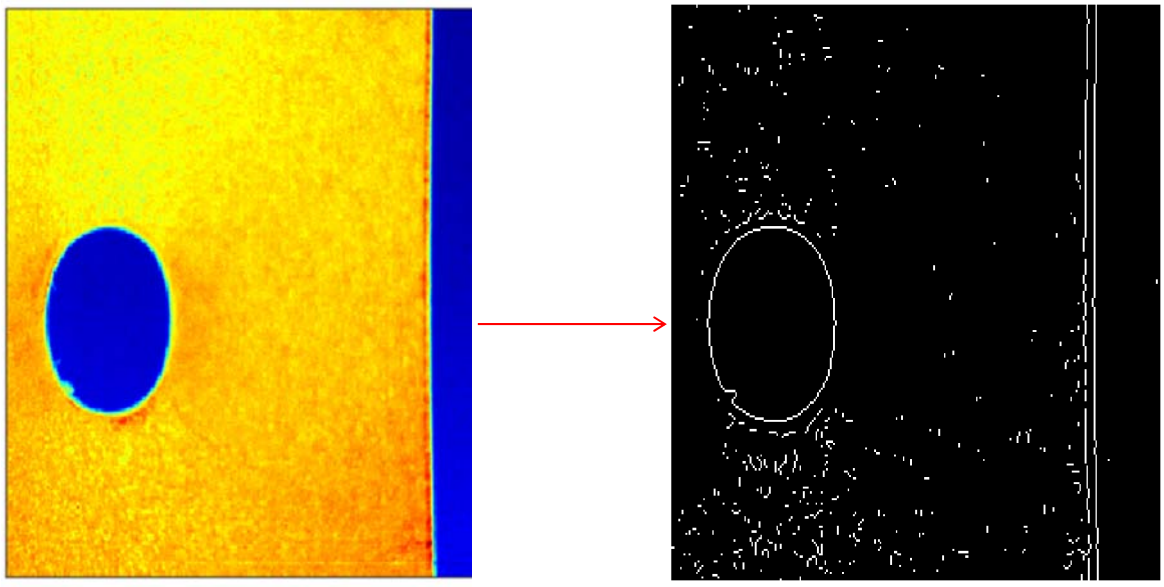

Figure 6.9 Edge detection of the thermal data.

A two dimensional cross correlation is then carried out between the image frame just before the start of the cyclic loading and all other frames. The resulting cross correlation is shown in Figure 6.10. Finding the location of the maximum value of the cross correlation allows the motion to be tracked. To attain a sub-pixel resolution of the motion, the centroid of a 7 x 7 pixels area centred on the maximum location is found.

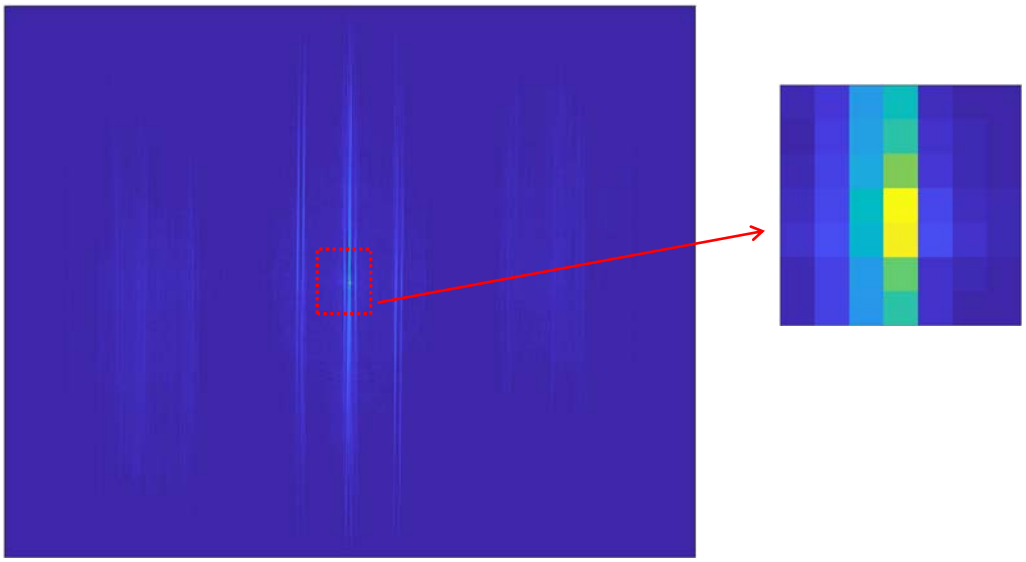

Figure 6.10 The cross correlation result showing the 7 x 7 pixels area centred on the maximum value.

The motion that can be detected is confined to translation motion i.e. displacement in the x and y direction. This is usually sufficient for rigid body motion of a cyclically loaded strip like specimen. It should be noted that more complex motions can be compensated using methods that rely on Digital Image Correlation (DIC) for tracking the motion [82]. Using the calculated motion, the effects of the motion are then corrected by 2D interpolation by a spline method. When there is significant motion, motion blurring is usually visible when image subtraction with the initial frame is performed on data without motion compensation (see Figure 6.11 (a)). It can be seen that these effects are minimized on the motion compensated data, as shown in Figure 6.11 (b).

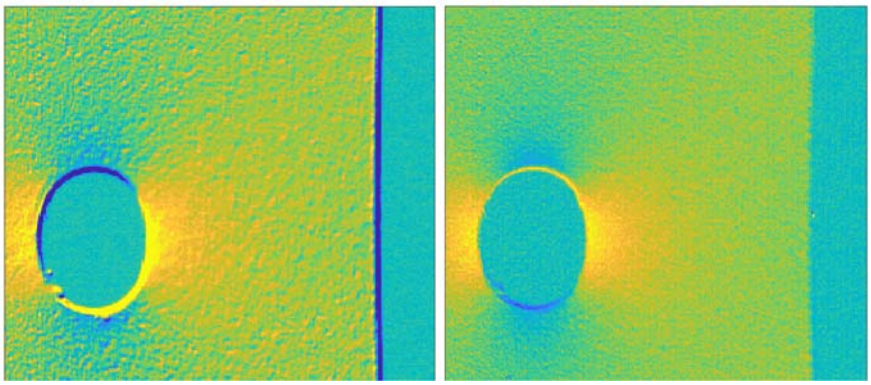

(a) (b)

Figure 6.11 Image subtraction: (a) without motion compensation (b) with motion compensation.

6.5.2 Results

The advantage of using a 'hole-in-plate' specimen to study the heterogeneity in the heat source is that the stress distribution in the specimen under loading could be easily identified using Finite Element Analysis (FEA). As the specimen is symmetrical in both *x* and *y* direction about the centre of the hole, a 3 D quarter model was created in Abaqus using eight node shell element with reduced integration as shown in Figure 6.12 (a). Only elastic behaviour was modelled, where the Young's modulus is 197 GPa and the Poisson's ratio is 0.3 [33]. For every cyclic loading applied, a single load step at the maximum far field stress of the applied cyclic load (σ_{max} = 205 MPa, 265 MPa, 295 MPa) was applied in the model. Reflecting the experimental conditions, the boundary conditions were such that the right edge was constrained in the y and z direction and the bottom edge was constrained in the x and z directions (see Figure 6.12 (b)). The load step was applied on the top edge. A very fine mesh size was also applied (refer zoomed in Figure 6.12 (b)).

The FE map of maximum stresses in a cycle in both the *y* and *x* directions were then obtained as shown in Figure 6.13 (a) and Figure 6.14 (a) respectively. These stress values can then be used to examine the dissipation at the same locations. However, it has to be verified that the stress values predicted are accurate. This can be done by comparing the sum of principal stresses from the FE model, to the stresses from the thermoelastic source from the same test. Since the model is elastic, the minimum stress can be obtained by multiplying the maximum stress by 0.1 as the load ratio is 0.1. The change in the sum of the principal stress, $\Delta(\sigma_{11}+\sigma_{22})$ is given by:

$$\Delta(\sigma_{11}+\sigma_{22})=(\sigma_{yy}+\sigma_{xx})_{\max}-0.1\times(\sigma_{yy}+\sigma_{xx})_{\max} \qquad 6.15$$

As seen in Figure 6.12 (c), the region of interest in the field of view is covered by 251 x 141 pixels. A window size of 65 x 65 pixels (N_x=N_y= 32) which has a reasonably good detection threshold was selected for the image processing procedure. As such, the thermal data cannot be processed at the edges, i.e. 32 pixels from the edge of the hole and 32 pixels from the edge of the plate, the first and last 32 points in this FEA were discarded to match the results from the thermal data as shown in Figure 6.13 (b) and Figure 6.14 (b).

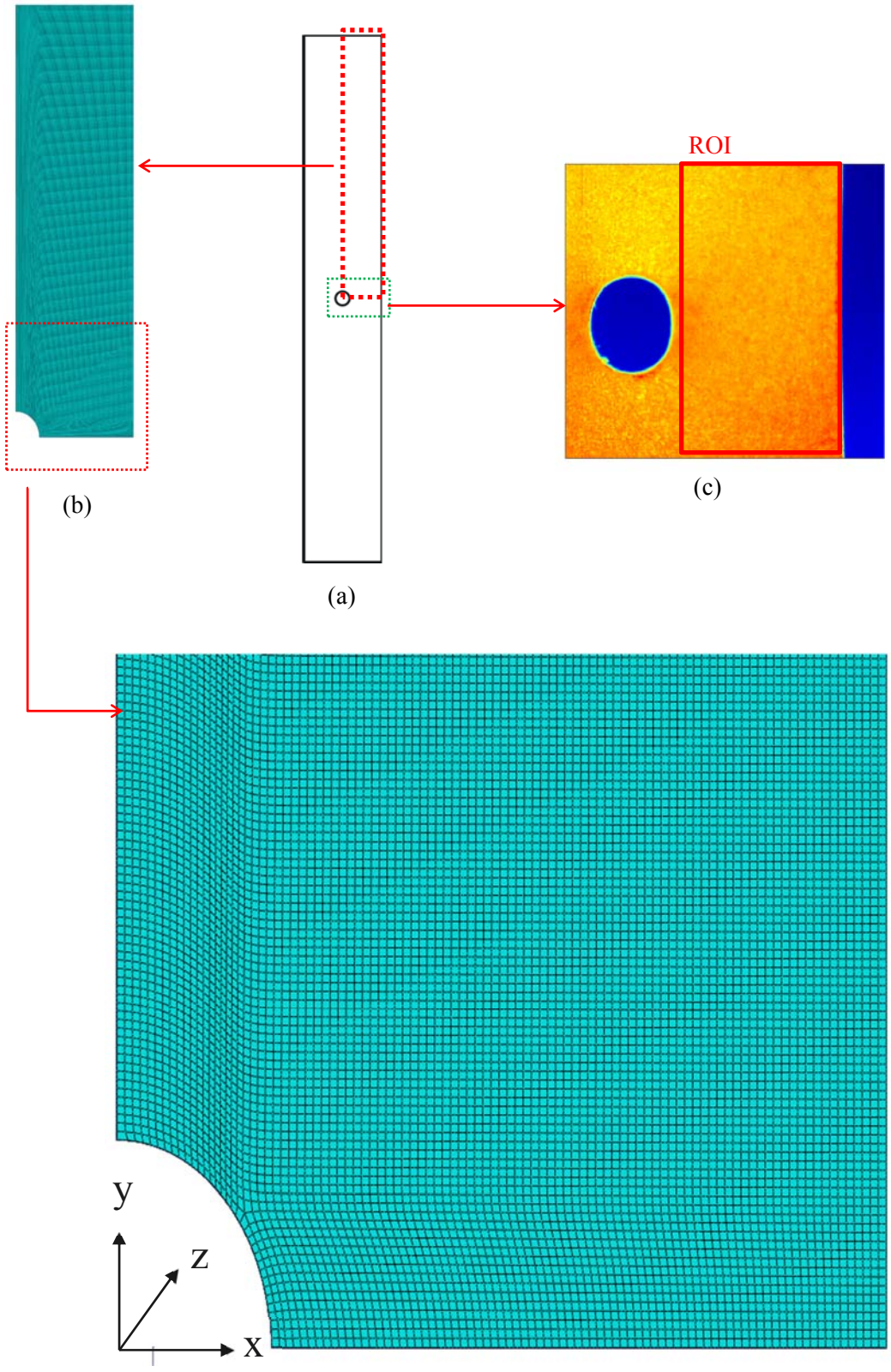

Figure 6.12 (a) The specimen (b) the FE model (c) the recorded thermal data.

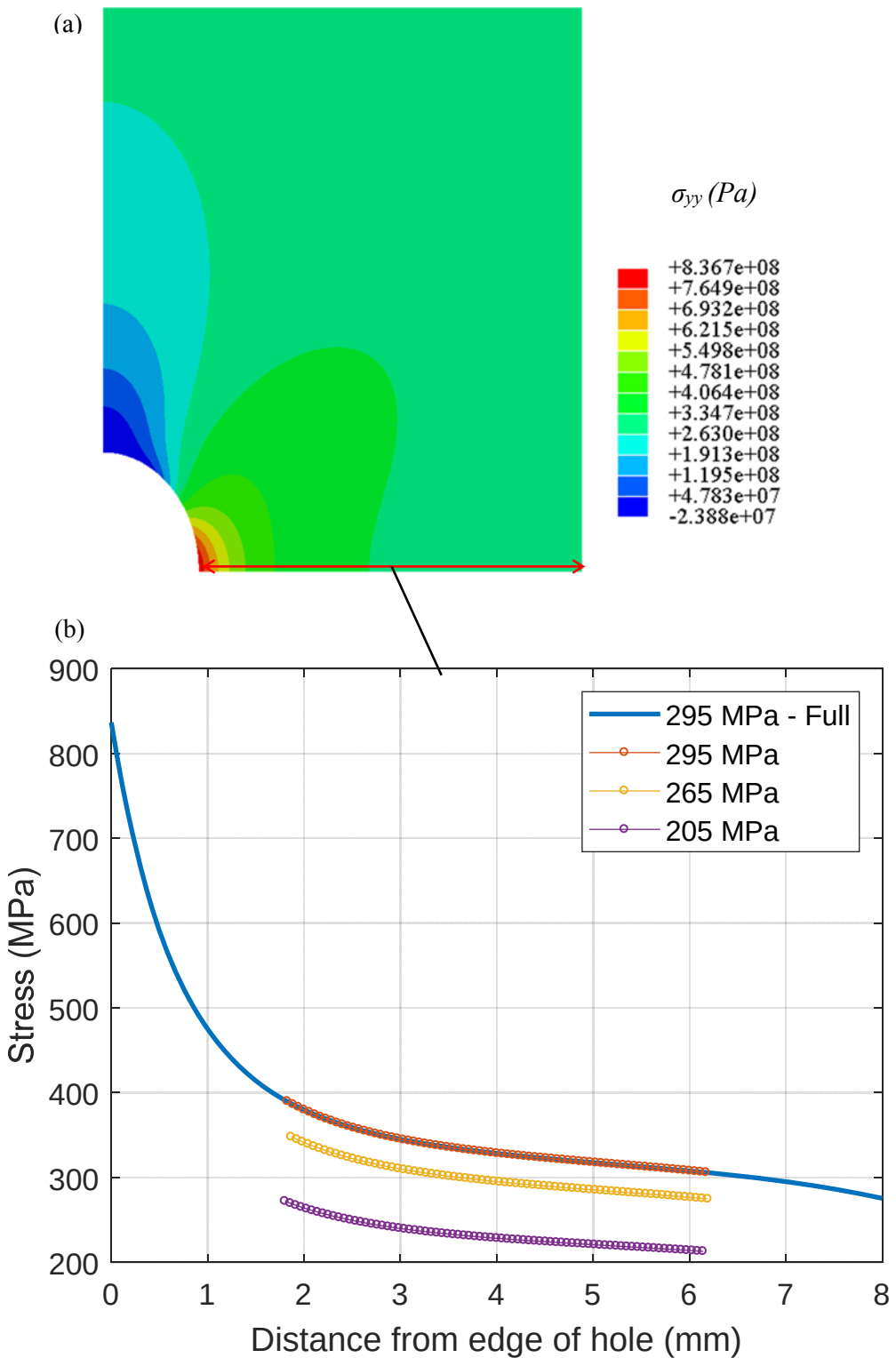

Figure 6.13 (a) σ_{yy} at σ_{max} = 295 MPa (b) The data along the edge of the hole to the edge of the specimen for σ_{max} = 295, 265, 205 MPa.

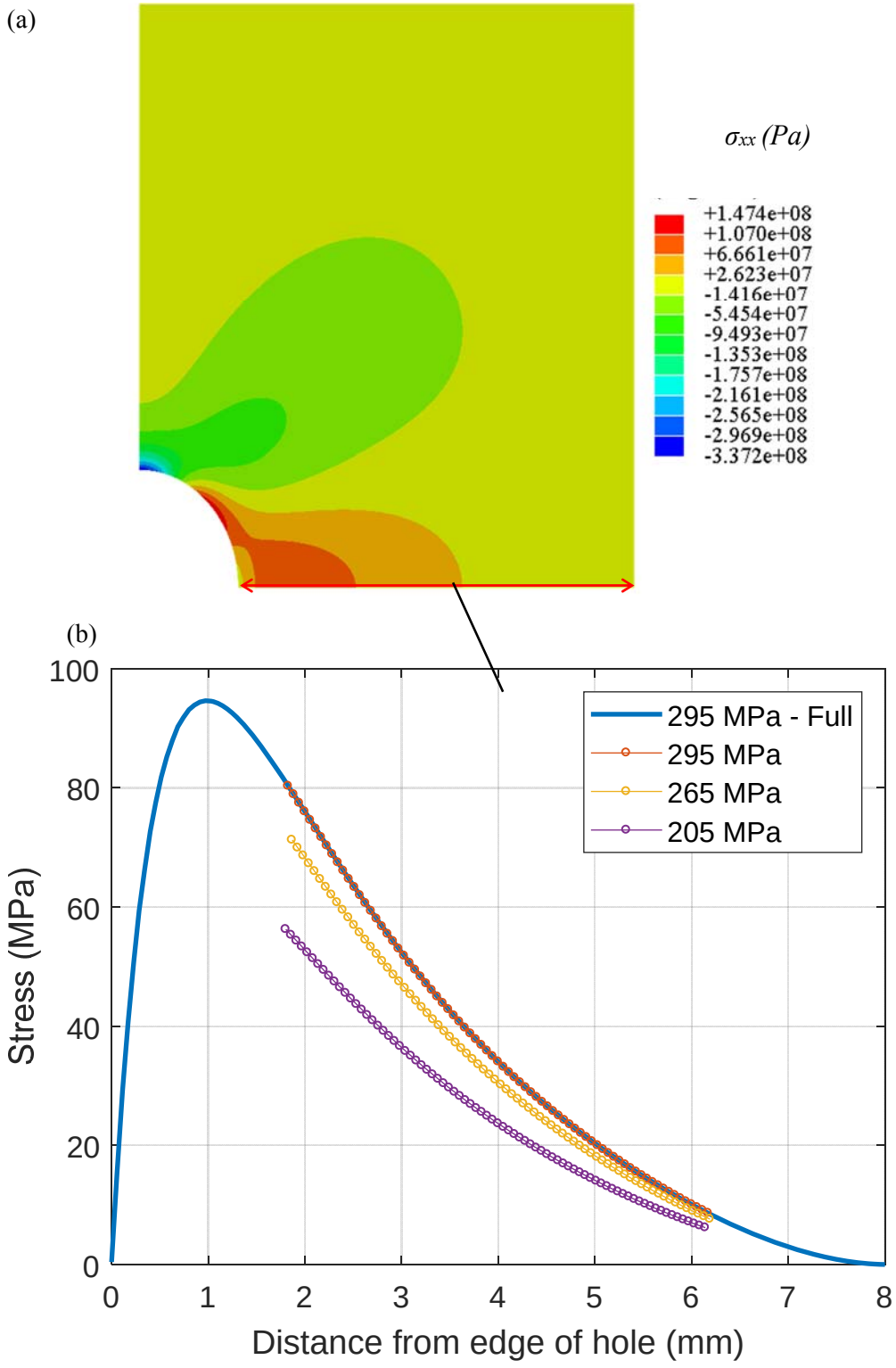

Figure 6.14 (a) σ_{xx} at σ_{max} = 295 MPa (b) The data along the edge of the hole to the edge of the specimen for σ_{max} = 295, 265, 205 MPa.

The FE data was added to provide the maximum stress sum in the cycle and then Equation 6.15 was applied to give the change in the principal stresses in the load cycle. This allows the FEA results to

be compared to the stress sum resulting from the thermoelastic source. The thermoelastic reponse, ΔT, is obtained from the thermoelastic source using Equation 6.14. To obtain the stress sum from ΔT it is necessary to apply Equation 2.15 and therefore the thermoelastic constant, K and the mean surface temperature of the component is required. A K of value of 4.3 x10^{-12} Pa^{-1} was used [33], which had been derived experimentally in a previous project for 316L stainless steel; the surface temperature of the component was obtained by averaging the temperature data throughout the test.

An example of the thermoelastic source field obtained from the thermal data is shown in Figure 6.15 (a) overlaid on the specimen. A significant portion of the data near the edges is lost due to the large window size used. The stresses derived from the thermoelastic source from along the black dotted line is compared to the FE model (see Figure 6.15 (a)). The comparison of the stress sum between the FE data and the source data is shown in Figure 6.15 (b) for three different cyclic loading levels specified by their maximum far field stress level. The source data matches that of the FE data. Due to the substantial smoothing obtained from large window sizes almost no noise is seen in the source data. The minor discrepancies between the source data and the FE data can be attributed to the averaging effect of the large window.

The dissipative source field was then calculated for the same set of thermal data. The resulting dissipative source at three different stress level (σ_{max} = 295, 265, 205 MPa) at three different times (t = *4 s, t = 8 s, t = 12 s*) can be seen in Table 6.1. The heat source at all the three different stress level remain stable over the entire test. At the highest stress (σ_{max} = 295 MPa), it can be said that the pattern of the heat source matches the thermoelastic source/stress distribution pattern (Figure 6.15 (b)) – that is, the heat source is higher at the region where a higher stress is experienced. The contours are not an exact match since the averaging effect of the large window is also present here. This distribution is also observed at σ_{max} = 265 MPa. Although the heat source at σ_{max} = 205 MPa follows the same trend, it contains regions that have a heat source value of zero. As the intensity of the heat source is close to the detection threshold, the result is noisy and therefore has regions that have negative values. With the lower level of colour bar set to zero, these noisy regions are identified by the saturated values.

This increase in dissipation due to an increase in stress can be compared to the purely uniaxial case presented in Chapter 5. The heat source distribution from the edge of the hole to the edge of the specimen, as a function of stress in the y direction, σ_{yy}, can then be compared to the increase in dissipation due to increasing stress from the uniaxial loading in Chapter 5. This is possible since the strip specimen subjected to uniaxial loading was also plastically strained to the same level (σ_{max} = 350 MPa) (refer Chapter 5). The comparison is shown in Figure 6.16. It can be seen that the stress range generated by three load levels in the hole-in-plate specimen are in good agreement with the result obtained from the eight load steps on the on strip specimen subject to a uniaxial stress. The minor discrepancies can be attributed to the averaging effect of the large window used.

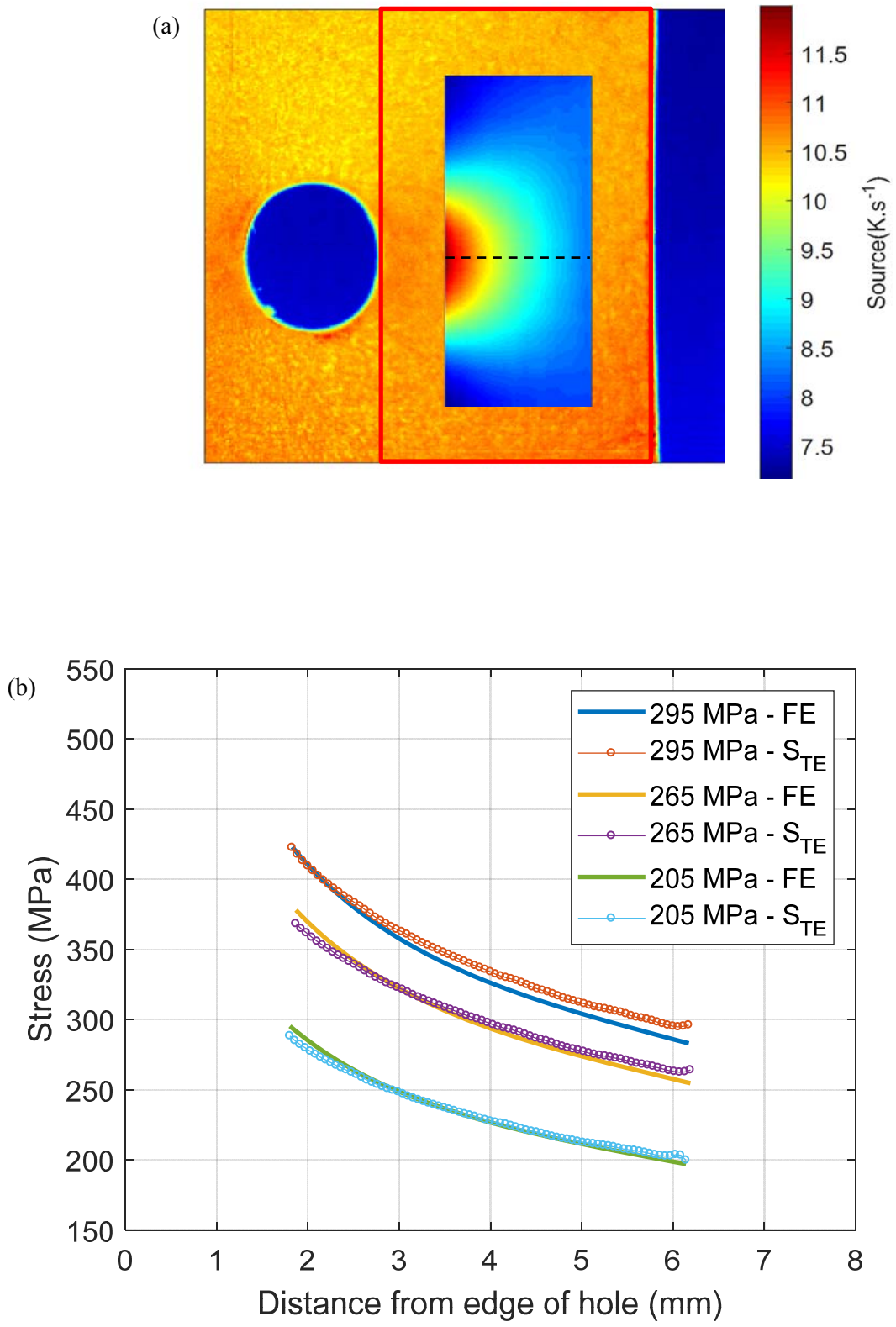

Figure 6.15 (a) The thermoelastic source for σ_{max} = 295 (b) Comparison of the thermoelastic source and FE result for σ_{max} = 295, 265, 205 MPa.

Table 6.1 The dissipative heat source at σ_{max} = 295, 265, 205 MPa.

	t = 4 s	t = 8 s	t = 12 s
σ_{max} = 295 MPa	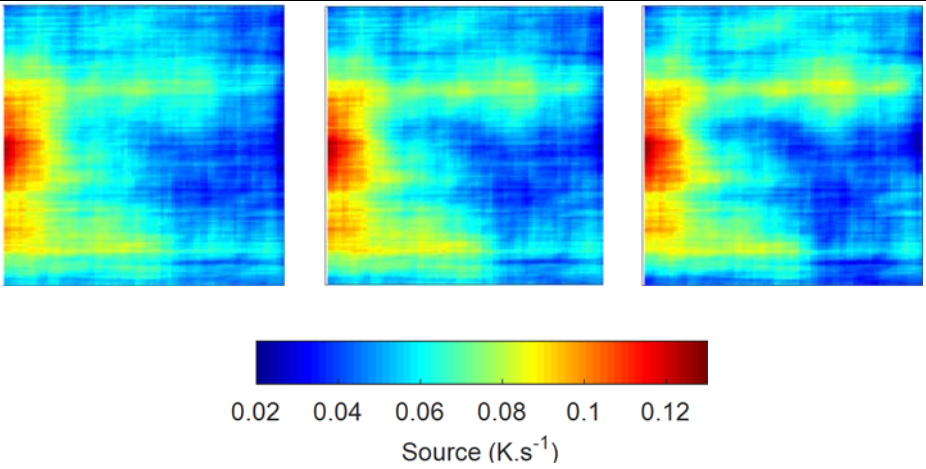		
σ_{max} = 265 MPa	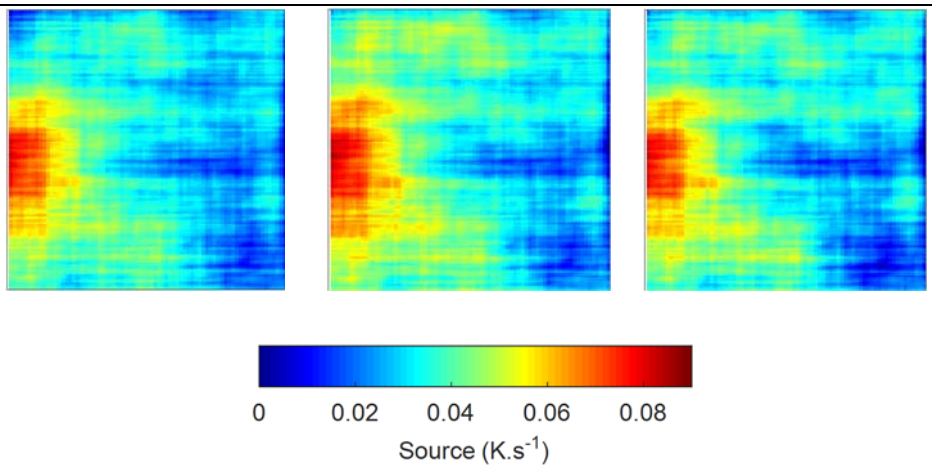		
σ_{max} = 205 MPa	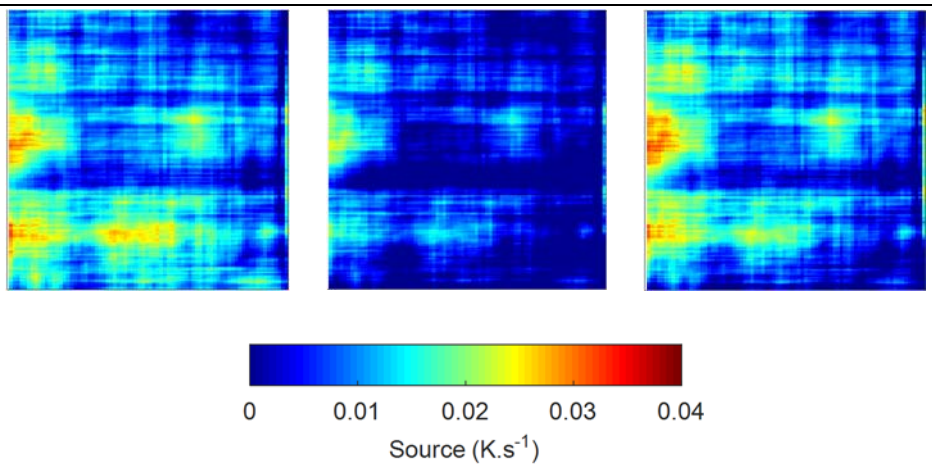		

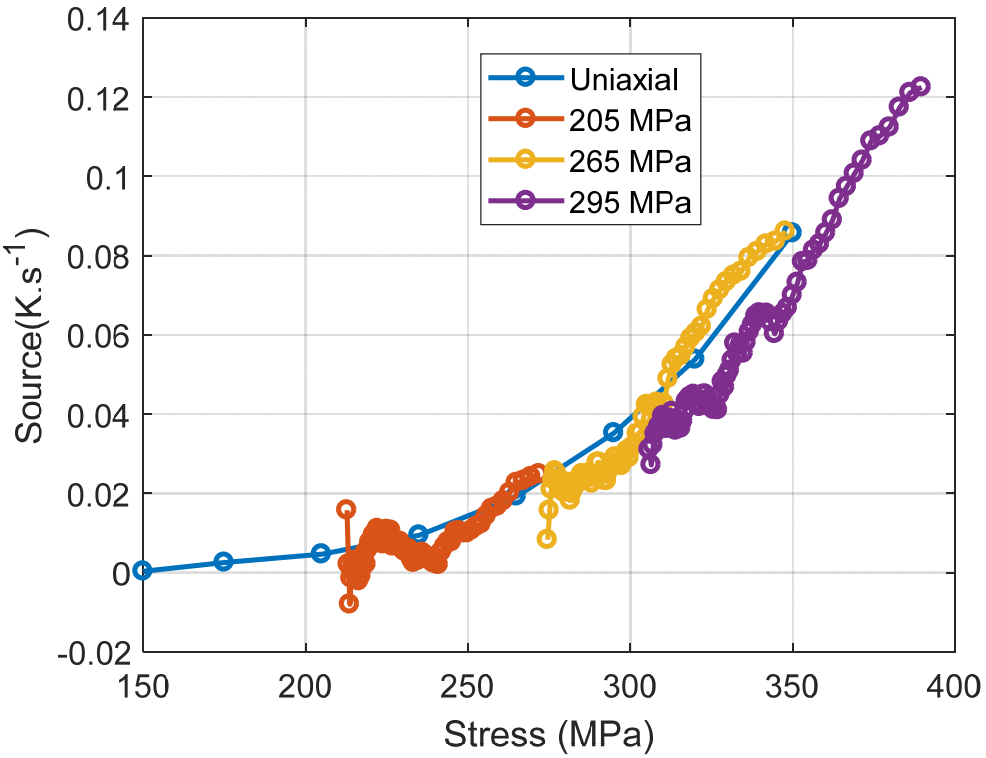

Figure 6.16 Comparison of the hole in plate heat source with uniaxial dissipative heat source.

6.6 Conclusion

The procedure to obtain spatially resolved dissipative heat sources from specimens with a non-uniform stress was developed and verified in this chapter. The image processing method of Berthel *et al.*[17] was successfully incorporated into the methodology of Maquin and Pierron [13]. In other words, by performing the temperature correction using the reference specimen, the full-field dissipative heat sources were produced with a lower detection threshold that is required for this work. However, the detection threshold of the image processing procedure to spatially resolve the heat sources is poorer than the spatial averaging method. It was shown that with careful selection of window size and spatial resolution it possible to assess the full-field dissipative heat source.

The ability of the image processing method to capture heterogeneities in the heat source was demonstrated using a test specimen with a non-uniform stress distribution i.e. a 'hole-in-plate' specimen. As established in Chapter 5, the dissipation increases with stress and therefore a non-uniform stress field would result in heterogeneous heat source distribution. To study the dissipative heat source distribution of the 'hole-in-plate' specimen next to the hole at high resolution, the experimental procedure was modified to image closer to the specimen while maintaining the chamber

in position. The results revealed that, the heat source distribution is indeed heterogeneous and to certain extent is similar to the thermoelastic response/distribution. In the next chapter the methodology is applied to a specimen that has a nominally uniform stress field but contains a non-uniform microstructure in the vicinity of a weld, demonstrating that the approach can be used to identify microstructural changes.

7 Dissipative heat source in the vicinity of a weld

7.1 Introduction

With the successful implementation of the image processing procedure, the final stage of the PhD is to address the evaluation of the heterogeneous dissipative heat sources developed in the vicinity of a weld as a result of the different microstructural regions. A necessary part of the process involves the design of a welded specimen that can be mounted in the chamber with the cross-section of the weld visible to the infrared camera. Therefore the type of welded specimen that would be most suited for studying the dissipative heat source is discussed. After establishing the configuration of the specimen, the different microstructural regions that are typically found in a welded specimen are reviewed. The mechanical properties of these regions are also discussed. The results from the preliminary test using a TIG welded specimen is presented. Subsequently, the dissipative heat source of a laser welded specimen is examined at both high resolution and low resolution. The results are verified by the mechanical properties of the welded specimen obtained from monotonic tensile testing by using Digital Image Correlation (DIC).

7.2 Considerations for design of welded specimen

One of the most important assumptions in applying the developed image processing procedure is that the temperature through the thickness of the specimen is uniform. To achieve this, the specimen must be thin. It has been shown in the previous chapter that this can be achieved in 316L stainless steel using specimens with thickness of 2 mm, therefore a key element in the design is that a 2 mm thickness must be achievable in the welded specimen and that the weld is uniform through the thickness. However, simply welding a thin sheet metal is not an option as the specimens would distort and warp even if they were clamped.

A possibility that was explored was producing a thin welded specimen by cutting a thin strip from a thick butt welded specimen. By cutting perpendicular to the welding direction, the cross section of the weld is revealed, enabling the imaging of the full extent of all the different microstructural regions of the weld. This approach has the key benefit of being able to examine the dissipative heat source arising from the different microstructural regions developed during the welding procedure, as opposed to just the base metal and fusion zone. The downside is that the cutting process may have an effect on the microstructure of the surface. However, by water-jet cutting the effect could be minimized, as material is removed abrasively in small amounts under constant cooling. Therefore, two butt welded specimens were designed and manufactured for the present study: a tungsten inert gas (TIG) welded specimen and a laser welded specimen, as detailed in the subsequent sections.

7.3 Regions in a fusion weld

As both TIG welding and laser welding are fusion welding processes, the mechanical properties and microstructure resulting from this process are reviewed. Specific properties of each weld are then presented in the following sections along with their microstructure. A typical weld joint consists of many different microstructural regions. It is well known that the microstructure in these regions are a direct consequence of the combination of the weld thermal cycle and the material composition [83]. For instance, the research conducted by Savage *et al.* [84] showed that there are at least five different regions. Figure.7.1 (a) shows the positions of these regions in a weld. This includes the Composite Zone where the base metal and filler metal were mixed to form a composite composition, the Unmixed Zone which consists of melted and re-solidified base metal that does not mix with the filler metal [83]. The Transition Zone exists to represent a composition transition from Composite Zone to Unmixed Zone in the case of heterogeneous welds which have filler metals of different composition from base metals [83]. There are also two different zones in the region where the work piece does not melt i.e.: the Partially Melted Zone (PMZ) and the True Heat Affected Zone (T-HAZ). The difference between these regions is that all metallurgical reactions in the T-HAZ occur in the solid state. Whilst it is clear that there may be several regions, the present study is limited to the mesoscale aspects of the weld and therefore this review is focused on three generalised regions only: the fusion zone – which represents all regions which melt and re-solidify, the Heat Affected Zone (HAZ), which represents the region experiencing higher temperatures but below the melting point of the material, and the unaffected base Metal (BM) as shown in Figure.7.1 (b). It is important to note that the boundaries between these regions are not always well defined in terms of microstructure as detailed below. However, it is useful to define these regions for ease of discussion. Of significant interest are the mechanical and metallurgical properties of these regions, with a focus on 316L stainless steel, i.e. an austenitic stainless steel.

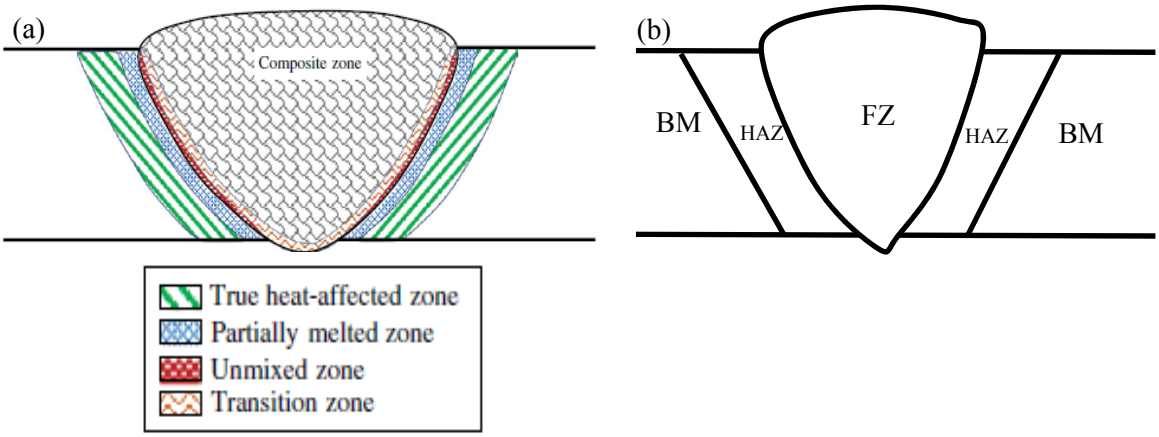

Figure.7.1 (a) Regions of a fusion weld [83] (b) generalised regions in a fusion zone.

The fusion zone is the region in which complete melting and solidification occurs. The fusion zone can be classified into three types: autogenous, homogenous, and heterogeneous. The autogenous weld is formed from the melting and re-solidification of base metal without the use of filler metal. They are commonly employed in situations where the section thickness is minimal and penetration can be achieved easily [83]. It is not applicable to all materials due to weldability issues. Homogenous welds use a filler metal that has an identical composition to that of the base metal. Type 316L base metal is usually welded together using 316L filler metal to achieve matching corrosion resistance properties [83]. Finally, heterogeneous welds are obtained using filler metals with a different composition to that of the base metal.

The solidification process plays a key role in determining the metallurgical nature of the fusion zone. Initially, nucleation occurs during solidification. The heat of fusion resulting from this transformation is dissipated by conduction through the solid away from the solidification front [83]. The solute is redistributed between liquid and solid as the composition of solid and liquid changes continuously. In all welding processes, the solid does not have time to reach its equilibrium composition. The redistribution results in local variations in composition in the solidified structure [83].

The solidification of the weld metal begins with the formation of dendritic /columnar grains which are relatively long. As metals are better heat conductors compared to the surrounding air, these grains form parallel to the heat flow/the plane of components being welded. The grain structure and its size mainly depends on the welding process employed and the filler metal used besides the type of metal itself. As a consequence of cast structure and coarse grains, the structure generally has low strength, toughness, and ductility [85]. This could be overcome by appropriate selection of filler metal and proper heat treatment.

Stainless steels solidify with ferrite or austenite as the primary phase [86]. This is determined by its specific composition. Austenitic stainless steels can undergo both solidification modes as they have

sufficiently broad composition range. More specifically, there are four possibilities for austenitic stainless steel solidification and solid state transformation. This can be observed in Figure 7.2. Types A and AF solidification have austenite as their first phase upon solidification. Fully austenitic solidification occurs in type A and it will remain austenitic upon cooling to room temperature as well. Figure 7.3 (a) shows the microstructure resulting from this solidification. Substructures such as cells and dendrites are noticeable. This is due to segregation of alloying and impurity elements that occur during solidification [86]. When 316 stainless steel undergoes type A solidification Cr and Mo will partition to the cell and dendrite boundaries [86]. In type AF solidification, ferrites form at the end of primary austenite solidification process. The microstructure (refer Figure 7.3 (b)) resulting from this transformation reveals ferrite along solidification subgrain boundaries. Similarly, two types of primary ferrite solidification could occur. The fully ferritic Type F results in acicular ferrite microstructure whereas when some austenite forms at the end of solidification the solidification is termed FA. This could produce either skeletal ferrite (Figure 7.3 (c)) or lathy ferrite (Figure 7.3 (d)) morphology depending on the Cr_{eq}/Ni_{eq} ratio of the composition. As for the 316L stainless steel used in this work, EN 10027 grade 1.4404 for which the chemical composition is listed in Table 7.1, the solidification type works out to be Type FA. Therefore, it is advantageous that a solid state phase change does not occur in this material during cooling and as such the microstructural changes can be attributed to mainly dislocation density.

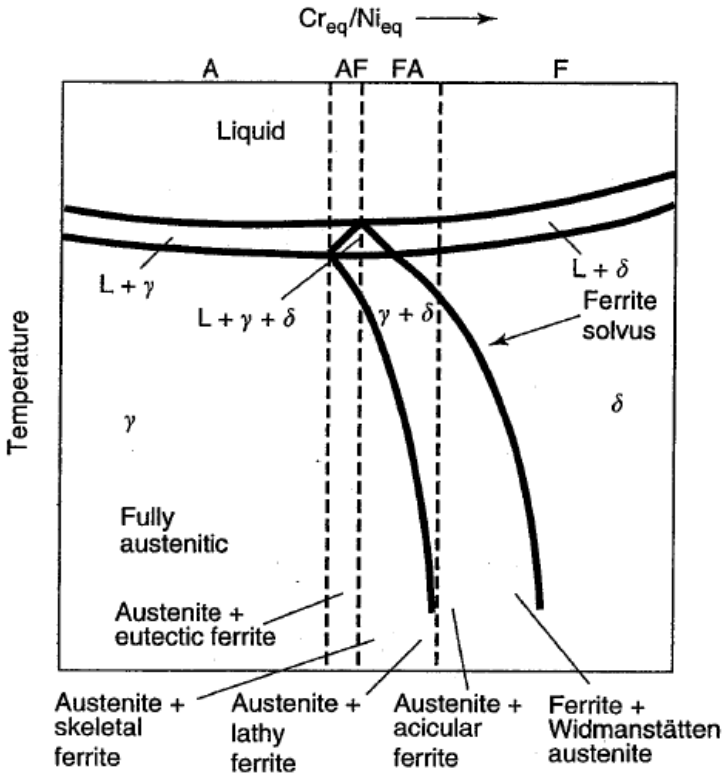

Figure 7.2 Solidification types shown in a phase diagram [86].

Table 7.1 Chemical composition of the EN 10027 grade 1.4404 austenitic stainless steel [4].

Element	C	Mn	Cr	Ni	Mo	N	Fe
Wt. %	0.02	<2.0	17.2	10.1	2.1	0.1	Balance

In terms of the dislocations in the FZ, the dislocation distribution segregates into sub-boundaries (see Figure 7.4) as opposed to the random nature of dislocations in the base metal [87]. However, the dislocation density with respect to the BM, is dependent on the initial condition of the BM, i.e. cold worked or annealed. From just within the FZ region, the part that is away from the welded surface tends to receive the lowest heat input rate and therefore has almost negligible sub-boundary misorientation which translates to the lowest dislocation density. In fact, the dislocation density in this case is comparable to that of a fully annealed dislocation structure [88]. The dislocation density then increases as the surface of the weld is approached. While this information is obtained from a GTA welded 316 stainless steel, a similar dislocation density values were obtained in the case of laser welded 304 stainless steel [89]. Just as for the dislocation density, the mechanical properties of the FZ with respect to the BM depends on the initial condition of the BM.

The HAZ is the region where melting does not occur. Generally the microstructural evolution of the HAZ depends on composition and thermal factors such as the maximum temperature it was raised to and the heating rate and cooling rate. The metallurgical reactions that occur in the HAZ are so complicated that large local variation of microstructure could be observed within the same weld. Some of the reaction that takes place in this region includes recrystallization, grain growth, and phase transformation [83]. Very limited grain coarsening occurs in the HAZ of austenitic stainless with the exception of when the base metal is in the cold worked condition.

Boyce *at al.* [90] observed that, in the case of an autogenously laser welded 304L stainless steel without a distinct HAZ region, there was a strain gradient in between the FZ and BM over a distance of approximately 1 FZ width. Since, the corresponding region did not have any change in terms of ferrite content or grain size with respect to the BM, this gradient has been attributed to difference in strength between the BM and FZ and also the degree of strain hardening. That is to say, metallurgical changes do not have a pronounced effect on the mechanical behaviour of the HAZ.

Interestingly, another study using the same type of material but with a slightly different laser welding parameter found a similar trend, in that, the hardness values of the FZ and HAZ are consistently harder than the BM for four different heat input (Figure 7.5) [91]. Nevertheless, the difference in the hardness values were actually minimal. The BM is weaker in the first case [90] because the welded plate was in an annealed condition whereas the history of the plate in [91] was not detailed.

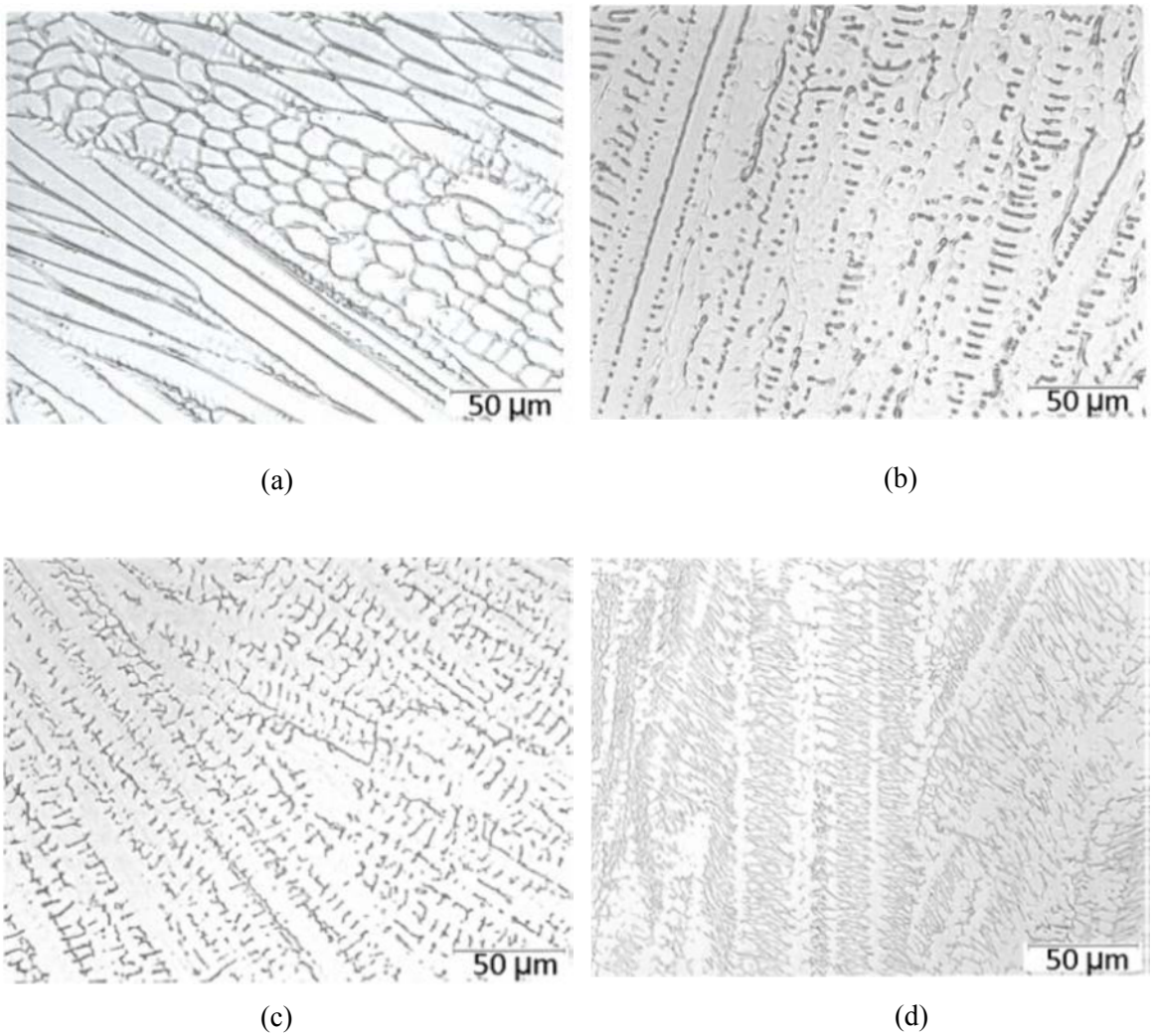

Figure 7.3 Fusion zone microstructure: (a) Type A, (b) Type AF, (c) Type FA, and (d) Type F [86].

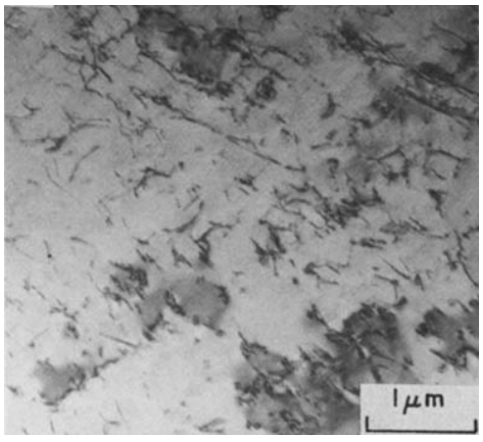

Figure 7.4 TEM of the FZ of laser welded 304 stainless steel showing the dislocation arrangements [89].

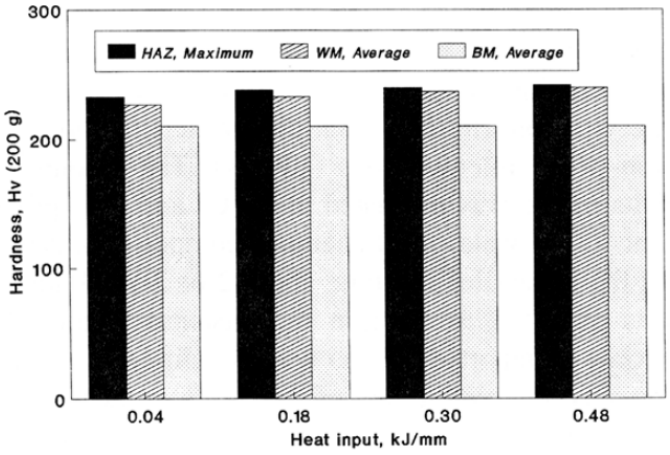

Figure 7.5 Hardness profile of laser welded 304L stainless steel (Note WM indicates FZ) [91].

7.4 The TIG welded specimen

The TIG welded specimen was designed as part of the RESIST project to be subjected to TSA tests. In the current PhD, these specimens were used for a preliminary study to assess if there was any indication of changes in the dissipative heat source in the vicinity of the weld and also to inform the design of a specimen especially for the study of the dissipative sources. Subsequently another set of specimens were designed and manufactured that were specifically intended for dissipation studies based on the outcome of the results of the present section.

7.4.1 Specimen Design

To create the test specimens, autogenous welding was carried out along the centre line of a 316L (EN 1.4404) austenitic stainless steel plate of dimensions 50 x 270 x 15 mm by simultaneous TIG welding on both sides of the plate with a heat input of 1246 W at a welding speed of 1.53 mm/s (see Figure 7.6(a)). Prior to welding, the material was stress relieved in a vacuum furnace at 1100 °C for 20 minutes followed by a slow cooling rate of 100 °C.hour^{-1} to avoid distortion. The different microstructural regions in the vicinity of the weld must be visible so they can be imaged. Hence, the welded plate was waterjet cut into strips of 2 mm thickness to reveal the cross section through the weld as shown in Figure 7.6 (b). The plate and a strip specimen are shown in Figure 7.6 (c).

The microstructure of the welded specimen was identified using optical microscopy. A macrograph (see Figure 7.7 (a)) was obtained to examine the extent of Fusion Zone (FZ) whereas the micrographs established the microstructural conditions of the different weld regions (Figure 7.7 (b) and (c)). The FZ is seen to have a dendritic grain structure due to rapid cooling. It should be noted that the relatively large grain size observed immediately next to the FZ boundary is due to the annealed initial condition

of the welded plate as opposed to grain coarsening due to the effect of welding. Hence, there is no noticeable HAZ region in terms of grain structure in the welded specimen produced.

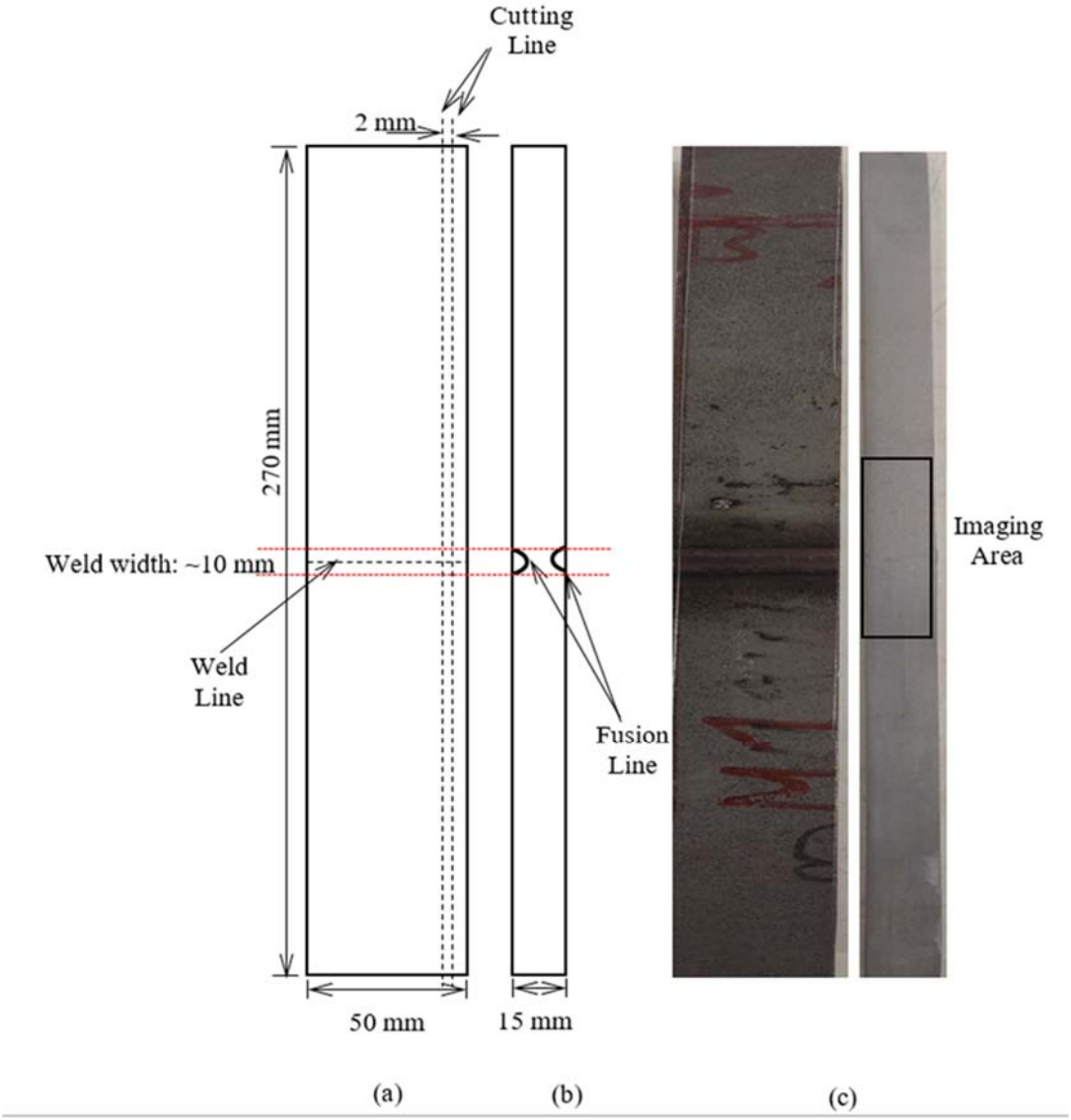

Figure 7.6 (a) Dimensions and weld line of the autogenous TIG welded plate, (b) water jet cut strip, (c) actual TIG welded specimen.

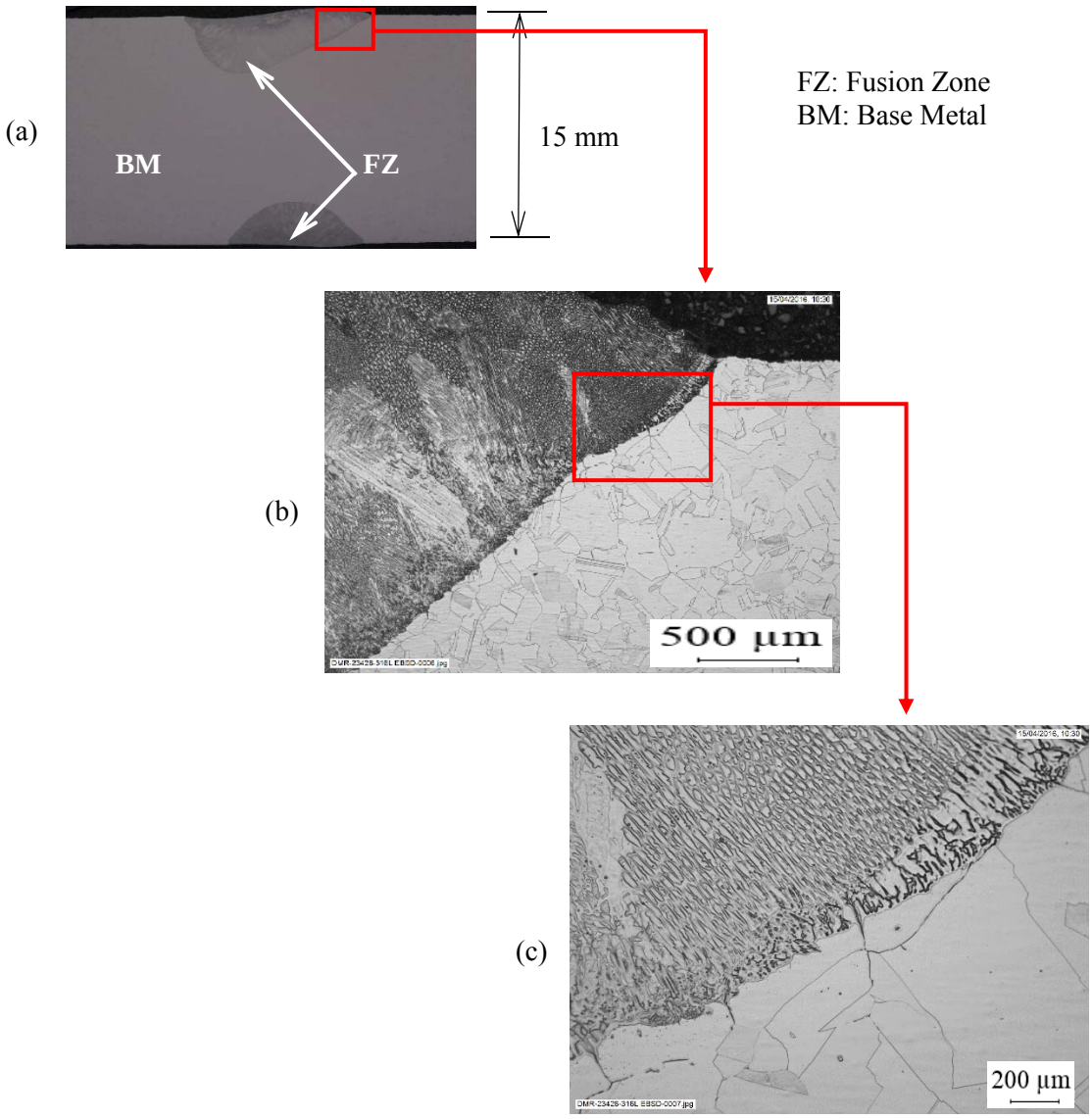

Figure 7.7 (a) Macrograph of the welded region (b) and (c) Micrographs of the welded region [92].

7.4.2 Results

A cyclic load with a maximum stress, σ_{max} of 250 MPa and load ratio of 0.1 was applied on the strip specimen at a loading frequency of 14 Hz and the dissipative heat source field was then obtained using the image processing procedure developed in the previous chapter. As shown in Figure 7.8 (a), the region of the welded specimen imaged is indicated by the black rectangle. This region is covered by 65 x 196 pixels. Noting that the resolution is not adequate to produce a contrast along the width, a full width window was employed i.e. a window size of 65 x 65 pixels spatially. This resulted in the 1 Dimensional heat source along the centre of the specimen as indicated by the red dotted line (Figure 7.8 (a)). The evolution of the heat source along the length of the indicated region for each time step is shown in Figure 7.8 (b) to (d). Note that 0 mm corresponds to the centreline (black dashed line) shown in Figure 7.8 (a).

Figure 7.8 (b) shows that at σ_{max} = 250 MPa that the base metal undergoes a rapid rise in dissipative heat source in the initial stages, suggesting that the base metal has yielded and started to work harden in the first few cycles. As the base metal completely hardens, the dissipative heat source reaches a plateau (elastic behaviour) (see Figure 7.8 (c)). In the FZ region, it was found that microplasticity occurred in the first few seconds quickly returning to elastic (viscoelastic) behaviour (see Figure 7.8 (b).

The test was repeated using the same parameters to study the dissipative heat source evolution under completely elastic loading for a more extended period of time. The evolution of dissipative heat source field in the elastic regime of the entire second test (Figure 7.8 (d)) was found to be similar to the evolution of the second part of the first test (see Figure 7.8 (c)). This can also be seen when a point in the BM and HAZ are plotted against time step as shown in Figure 7.8 (e) and (f) where the difference between the dissipative heat source levels in the BM and HAZ regions are consistent in both cases. The fluctuation in the dissipative heat source of the HAZ region in Figure 7.8 (f) is expected, since the intensity of the heat source is below the detection threshold. To verify the result, a tensile test was performed on the same specimen. The stress-strain behaviour of the specimen was evaluated using Digital Image Correlation (DIC) during a uniaxial tensile loading at a strain rate of 0.0005 s^{-1}. The test data was recorded using an E-Lite 5M camera from LaVision and processed using the DaVis DIC software. Figure 7.9 (b) shows that the yield point of the BM has increased to just above 250 MPa. The similarity between Figure 7.9 (a) and the dissipative heat source field in Figure 7.8 (b) where yielding first occurs is also to be noted.

It can be seen that the dissipative heat source response of the different microstructural regions are different. However, the current specimen is less ideal in that the heterogeneous microstructure that is visible in the micrograph is towards the edges of the specimen. Even if imaged at higher resolution, the large window size required to reduce noise would mean that a significant portion of the region of interest would be lost. Hence, a specimen that has FZ covering the entire width is required.

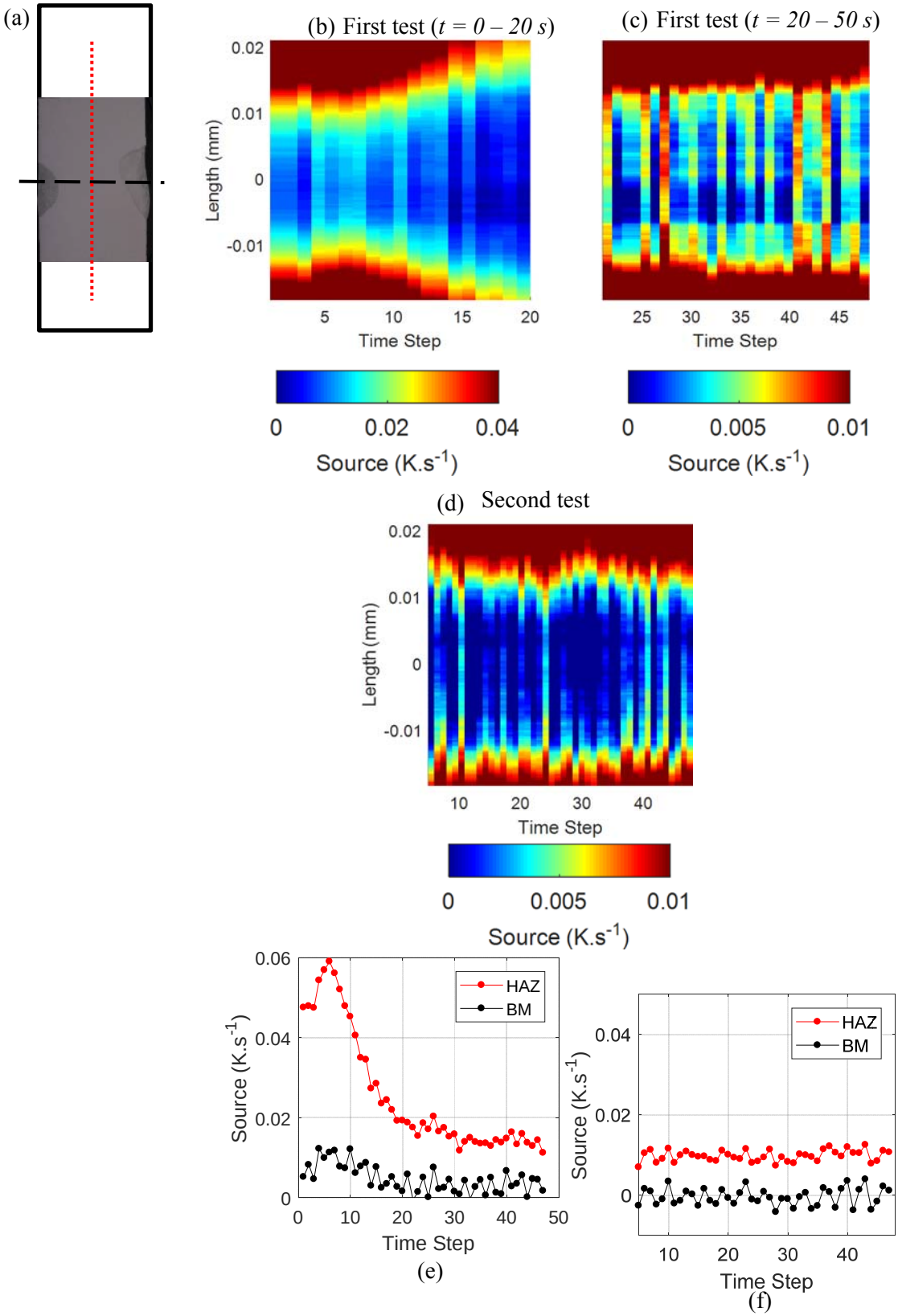

Figure 7.8 (a) The test specimen, evolution of 1D Dissipative Source for first test at σ_{max} =250 MPa: (b) part 1 and (c) part 2, Second test at σ_{max} =250 MPa (d), Dissipative heat source evolution of a point for first test (e) and second test (f).

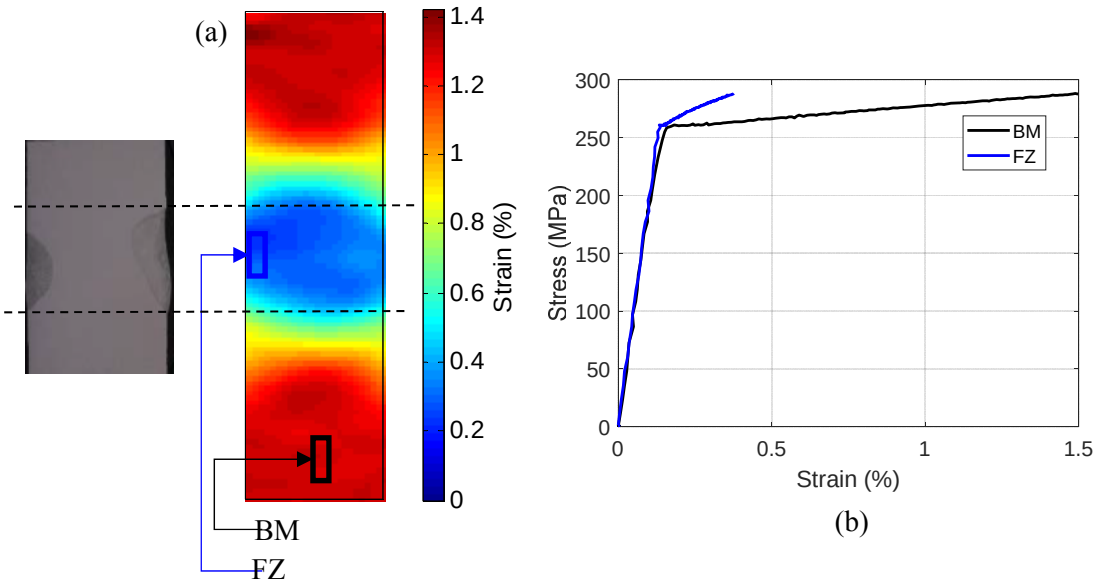

Figure 7.9 Tensile test DIC: (a) normal strain distribution in the loading direction (b) stress-strain curve.

7.5 Laser Welded Specimen

7.5.1 Specimen Design

The test specimen was created by welding along the width of two 316L (EN 1.4404) austenitic stainless steel plate positioned edge to edge (see Figure 7.10 (a)) and clamped in position. A 5 kW laser welding process was used with a speed of 0.3 m.min^{-1} to create an autogenous weld (i.e. no filler material used) in two passes on each side of the specimen. The laser used was a 1 micron wavelength fibre delivered laser with a spot size of 300 microns. To conduct the IR imaging on the different microstructural regions in the vicinity of the weld, the welded plate was waterjet cut into strips of 2 mm thickness to reveal the cross section through the weld as illustrated in Figure 7.10 (b). The macrograph of the cross section is shown in Figure 7.11 (a). It can be seen that the grain structure of the base metal (refer Figure 7.11 (b)) is similar to the as received strip specimen and has a mean grain size of approximately 25 µm. The lines that are visible are delta ferrite stringers. They are formed as a result of the cold rolling process. The FZ microstructure is dendritic in structure (see Figure 7.11 (c)).

The two passes of the FZ is also clearly visible. The full profile that can be seen is the second pass, identified as FZ 2. The first pass labelled FZ 1 does not a have full profile since it has been melted again by the second pass.

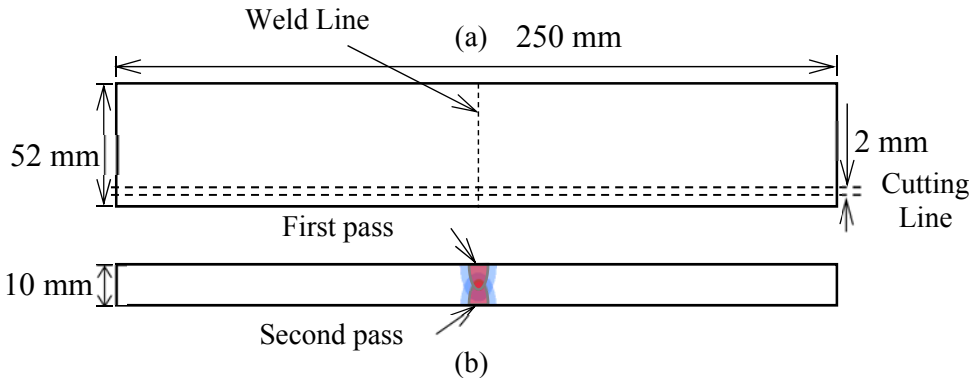

Figure 7.10 (a) Dimensions and weld line of the autogenous laser welded plate, (b) water jet cut strip.

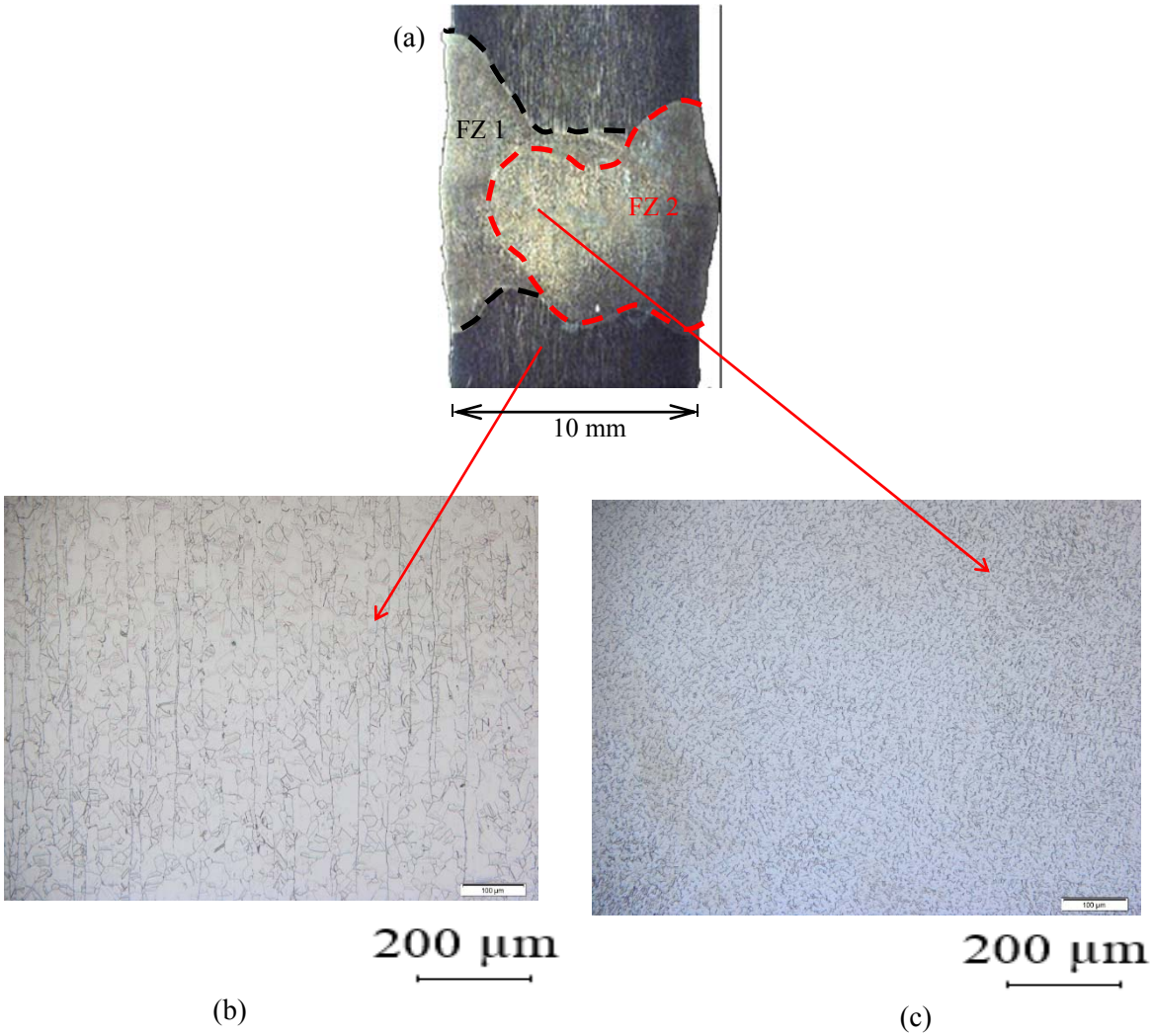

Figure 7.11 (a) The macrograph of the weld (b) the base metal microstructure and (c) the weld metal microstructure.

The mechanical properties local to each microstructural region were then examined by obtaining the stress-strain behaviour during a monotonic tensile test on the welded strip specimen. The strain

distribution obtained from DIC during yielding is shown in Figure 7.12 (a). Assuming that the width of the specimen is nominally uniform, the stress strain curve of the region highlighted in Figure 7.12 (a) is shown in Figure 7.12 (b). The FZ hardens slightly more than the BM. The strongest region is the region in between the FZ and the BM as it shows the highest hardening. Whist this region may be regarded as the HAZ, there is not a well-defined region in terms of both the mechanical properties (as seen in the strain distribution along the centre of the width as in Figure 7.12 (c)) and the microstructure.

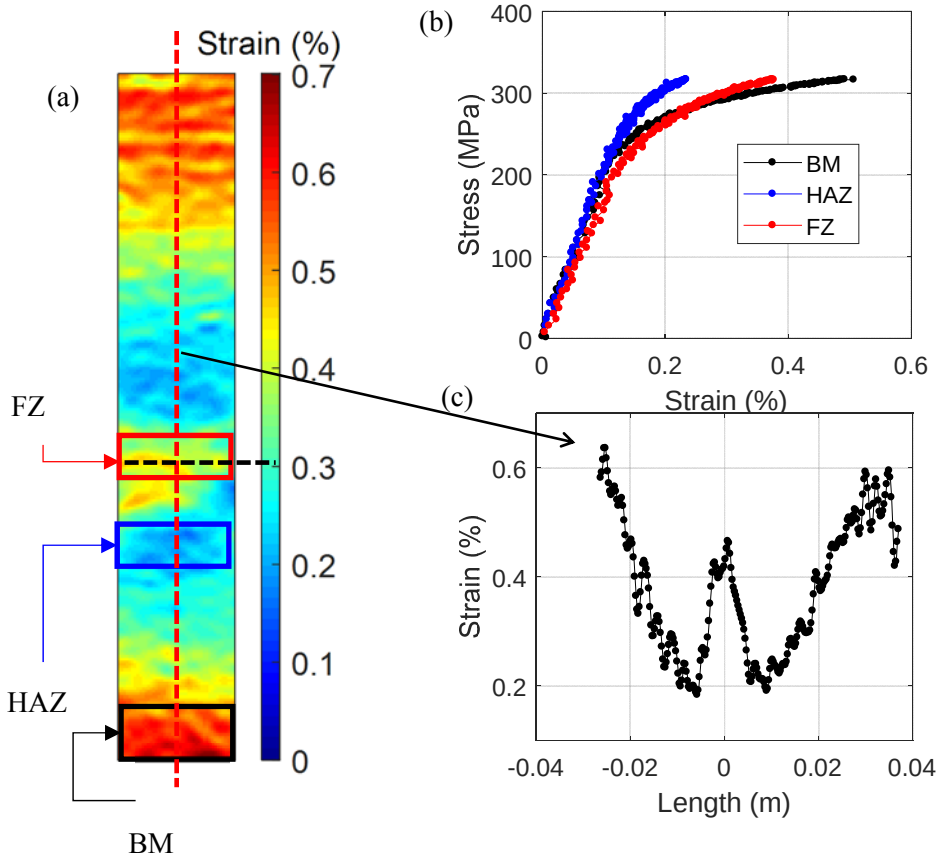

Figure 7.12 Tensile test DIC: (a) normal strain distribution in the loading direction, (b) stress-strain curve, (c) the strain distribution along the vertical centreline of the specimen.

7.6 Dissipative source obtained from laser welded strip

The test was imaged at low resolution using the same experimental setup described in Chapter 3 so that the whole specimen could be studied at stress levels between $\sigma_{max} = 215$ MPa and $\sigma_{max} = 385$ MPa in increments of 25 MPa at a load ratio of 0.1 and a loading frequency of 14 Hz. As the stress is increased, the specimen eventually cyclically hardens. Subsequently, the test was repeated at the same stress levels at both low resolution and high resolution focusing in on the fusion zone of the

weld. It is worth noting that in the second set of tests, the behaviour of the specimen is completely elastic since the yield stress was increased by cyclic hardening.

The dissipative heat source was evaluated as described in Section 7.4.2. As such, the results consist of the dissipative heat source distribution along the centre of the specimen where the position 0 mm refers to the centreline of the weld (see black dotted line in Figure 7.12) for Figure 7.13 (a) to (e).The results from the first set of test is shown in Figure 7.13 (a) to (c). The general trend in these figures is that the dissipation is highest at the BM and gradually decreases towards the HAZ and then undergoes a sharp rise as it approaches the centreline of the weld. It should be noted that it is less noticeable in Figure 7.13 (a) since the dissipation is close to the detection threshold and hence is dominated by noise. At lower stresses where plasticity was still expected to occur based on the stress strain curves, it was found that significant cyclic hardening was not apparent. This is due to the small interval between the stress levels from σ_{max} = 215 MPa to σ_{max} = 335 MPa where cyclic hardening is also less apparent. When the σ_{max} was increased from 335 MPa to 385 MPa, there was a significant rise in dissipative heat source in the base metal, which was established to be the weakest of the three region (see Figure 7.13 (d) & (e)). Accordingly, a considerably smaller rise in dissipation is seen at the FZ and HAZ regions as it was established that these regions are stronger than the BM.

Noting that the BM is similar in grain structure to the as received strip specimen used in Chapter 4 and 5, the dissipation at the BM from the second set of test (after cyclic hardening) were compared to the dissipation of the cyclically hardened strip specimen. The data for the BM was obtained from a point 0.02 m above the centreline of the weld. As shown in Figure 7.14, the increase in dissipation with stress is similar for both the specimens. A higher dissipation is consistently observed in the case of the BM since it was cyclically hardened at σ_{max} = 385 MPa, whereas the strip specimen was hardened at σ_{max} = 350 MPa.

Additionally, the effect of cyclic hardening can also be seen in the other regions of the weld as shown in Figure 7.15 (a) and (b). The black dotted line seen in Figure 7.15 (a) is obtained from the temporal average of Figure 7.13 (a). It can be seen that initially at σ_{max} = 240 MPa, there is no clear trend in the dissipative heat source pattern due to noise. After cyclic hardening, the dissipation increases and a trend emerges. This is due to the increased dislocation density in all of the regions as a consequence of cyclic hardening. In the case of a slightly higher stress, σ_{max} = 290 MPa, where a trend is already visible, the trend is maintained but an increasing shift is seen after cyclic hardening (refer Figure 7.15 (b)).

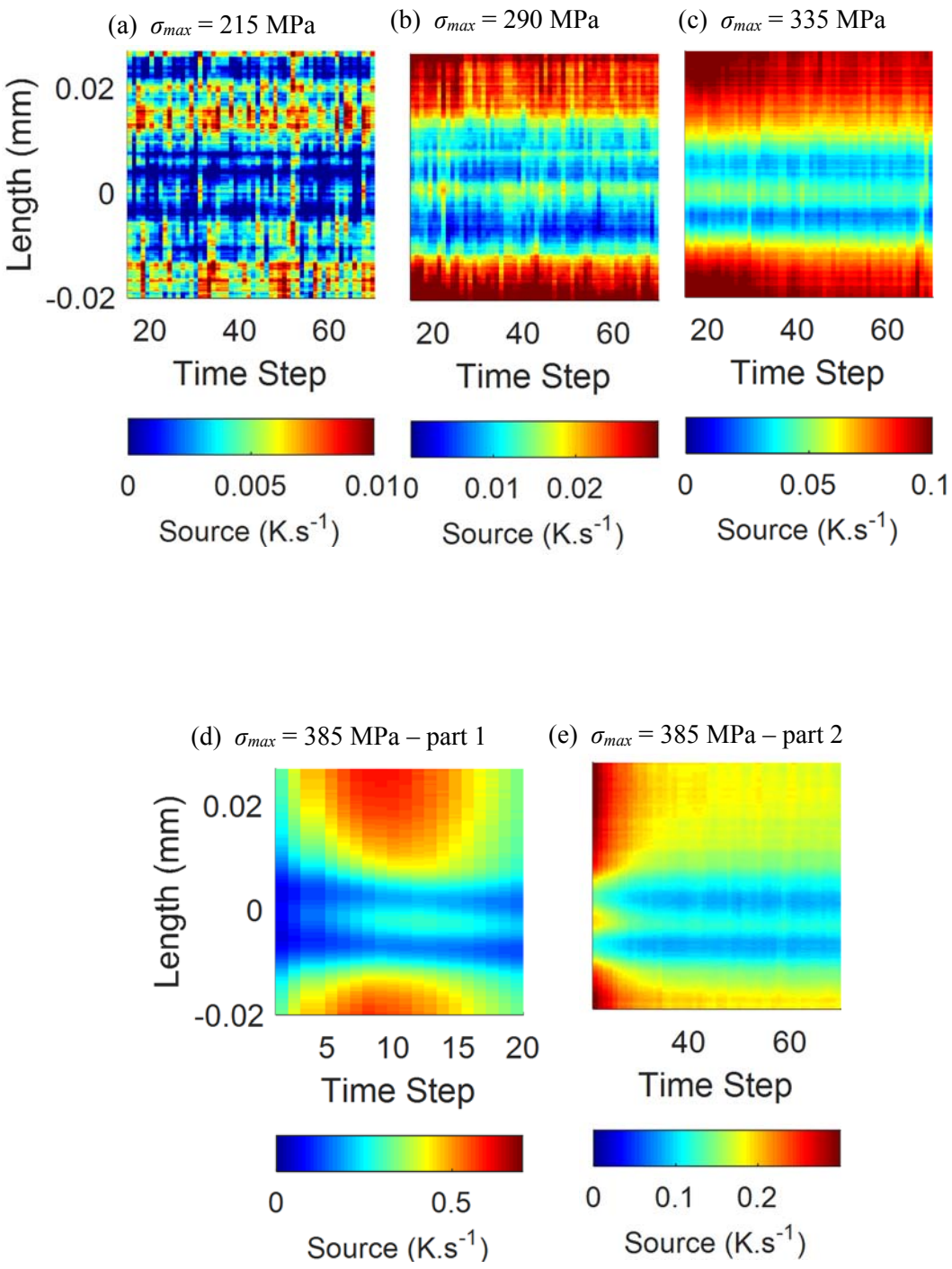

Figure 7.13 (a) to (e) The 1D dissipative heat source distribution at increasing stress levels

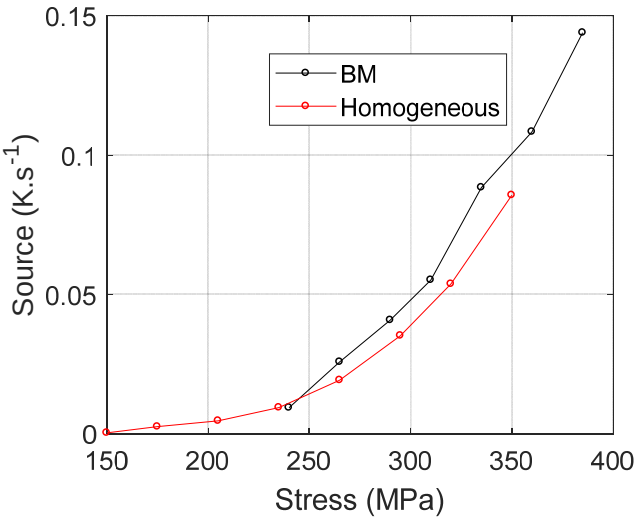

Figure 7.14 Comparison between the spatially averaged heat source from homogeneous specimen to dissipation of base metal.

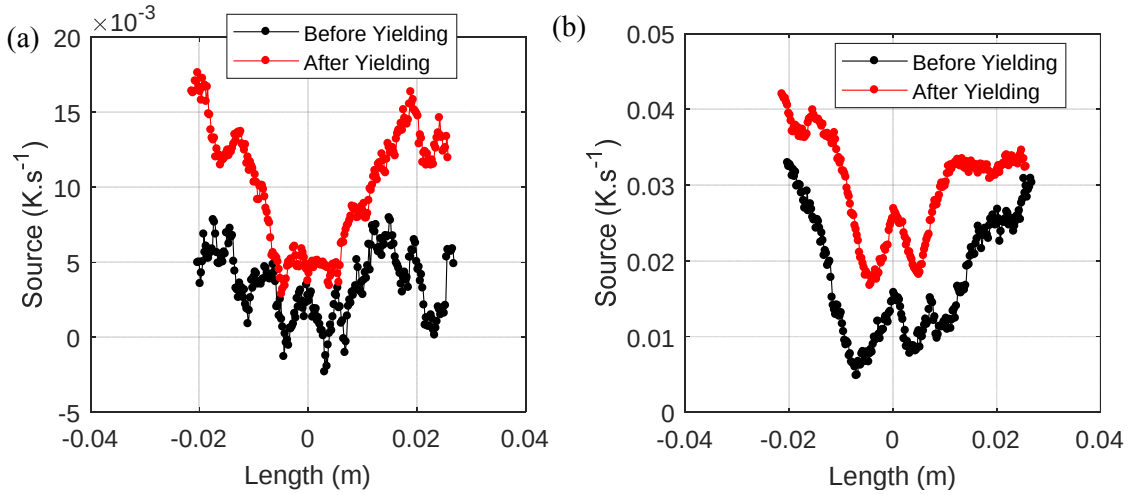

Figure 7.15 Comparison of dissipation before and after cyclic hardening at σ_{max} = 385 MPa for σ_{max} = (a) 240 MPa and (b) 290 MP.

It can be observed that this general trend seen in the dissipative heat source distribution (Figure 7.15 (b) for instance) is similar to that of the distribution of the strain in Figure 7.12 (c). By normalizing these distributions with respect to their maximum value, the two of these quantities can be compared. From Figure 7.16, for dissipative heat sources at a few different stress level and the strain distribution, it can be seen that the distribution is similar.

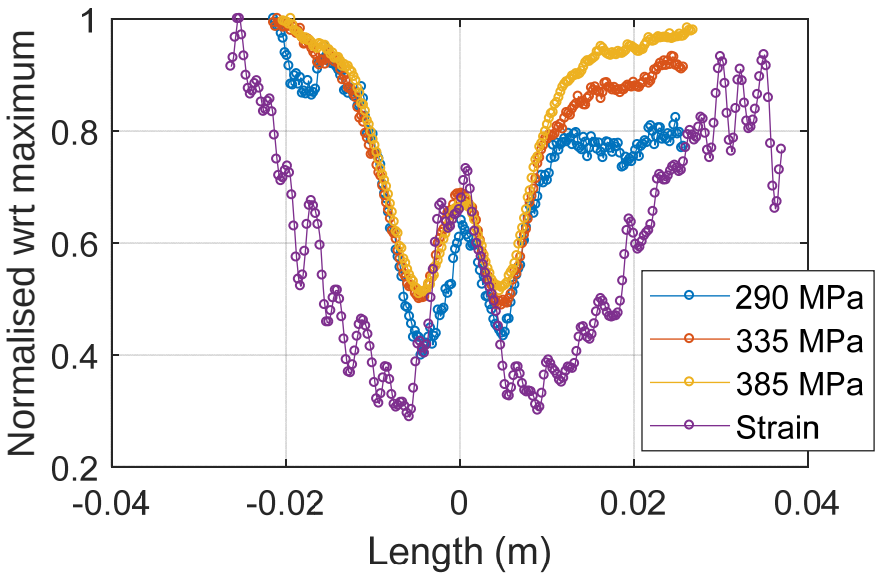

Figure 7.16 Comparison of normalised dissipation at σ_{max} = 385, 355, 290 MPa and normalised strain distribution.

Subsequently, the same strip specimen was tested at the same load levels and imaged at high resolution. The field of view of the thermal data at high resolution is shown in Figure 7.17. It has a spatial resolution of 55 µm/pixel. Due to the increase in noise level at higher resolution, a large window size of 65 x 65 pixels had to be used. The approximate size of the resulting dissipative heat source field with respect to the region of interest can be seen in Figure 7.17.

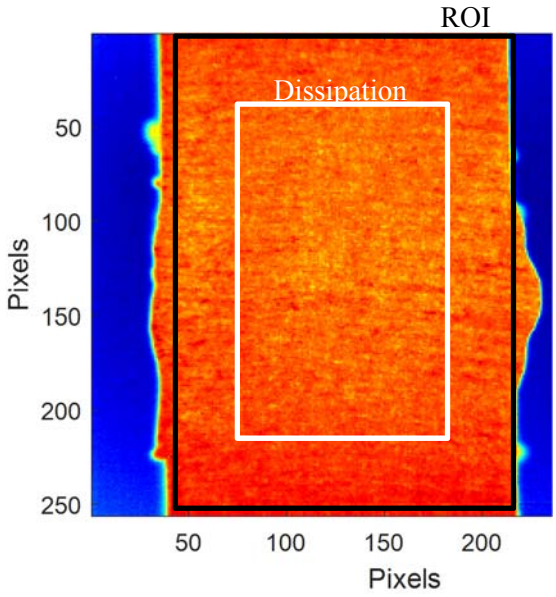

Figure 7.17 The approximate size of the ROI and the resulting dissipative source field.

The resulting dissipative heat source field at stresses of σ_{max} = 385 MPa, 335 MPa and 290 MPa are provided in Table 7.2 at different times of the test. A similar heterogeneous pattern can be observed at all stress levels, which are also stable over time. To verify that the heat source produced is

consistent with the results obtained at low resolution, the heat source at the centre of the width at high resolution was compared to the result obtained at low resolution for a stress level of σ_{max} = 385 MPa (see Figure 7.18). The magnitude and distribution are similar in both cases. However, at low resolution the change is seen to be more gradual due to the window size. The 37 x 37 pixels in a window is larger in physical units compared to the 65 x 65 pixels at high resolution. As a result a greater averaging effect is expected at low resolution.

Table 7.2 The dissipative heat source at σ_{max} = 385, 355, 290 MPa.

	t = 4 s	t = 8 s	t = 12 s
σ_{max} = 385 MPa	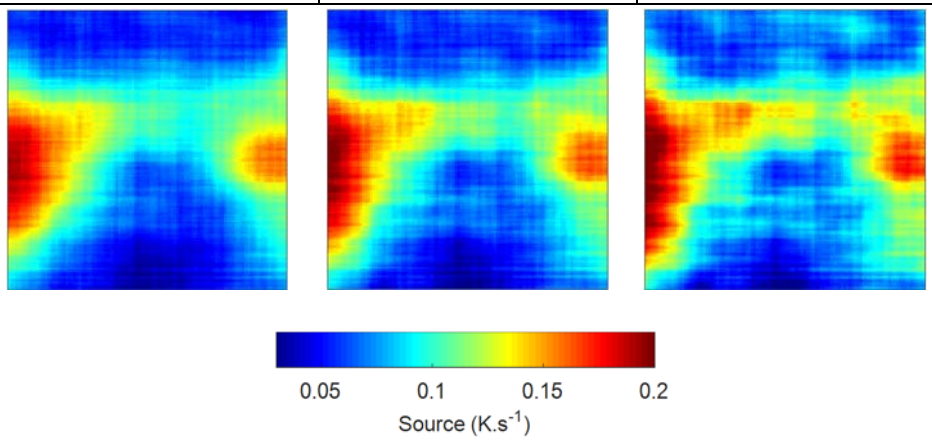		
σ_{max} = 335 MPa	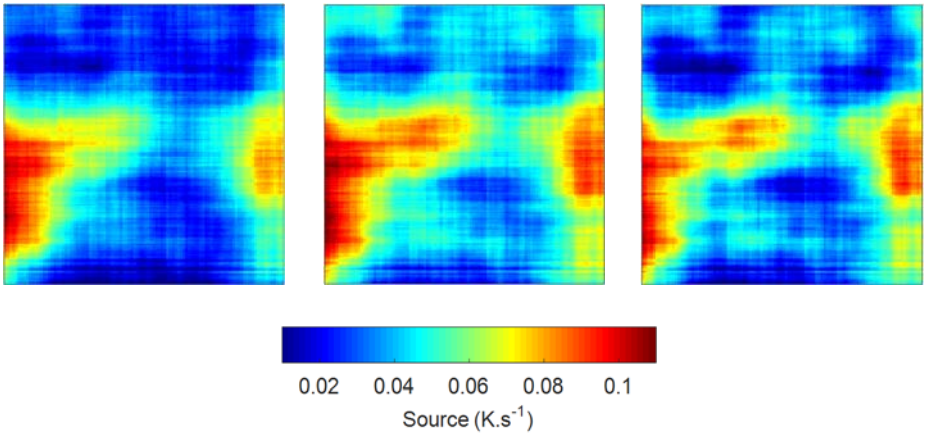		
σ_{max} = 290 MPa	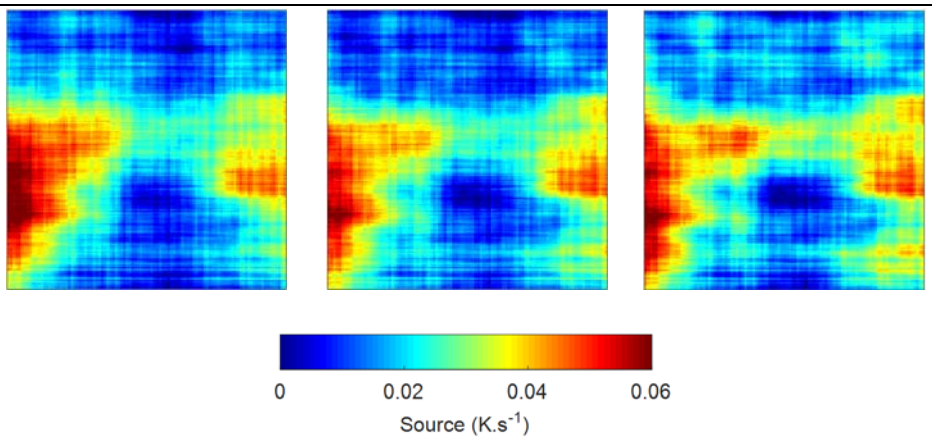		

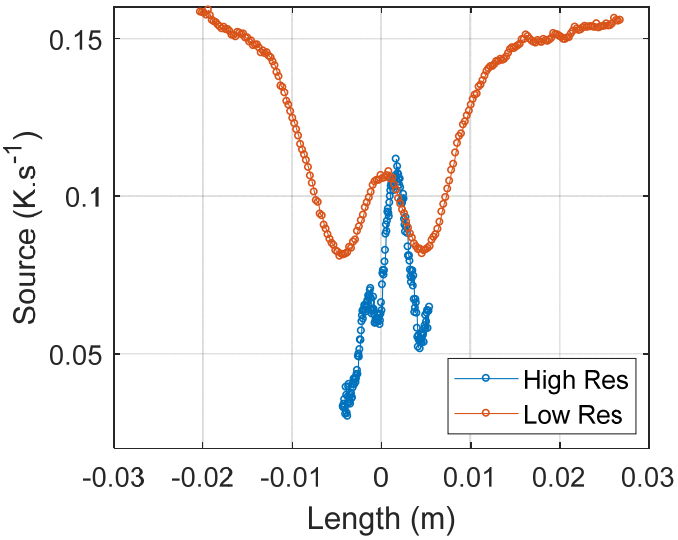

Figure 7.18 Comparison of the heat source at high resolution and at low resolution.

To interpret the results of the dissipative heat source field at high resolution, it was overlaid on top of the macrograph of the same specimen as seen in Figure 7.19. It was ensured that the locations of the macrograph and the dissipative heat source field correspond to each other precisely. The boundaries of the fusion zone and the patterns observed in the dissipative heat source field is not a perfect match. This is thought to be caused by the inevitable over-smoothing as a result of large window size. However, the pattern of the dissipative heat source is consistent with the dislocation density levels that are expected in theory. In the FZ2 region for instance, the region away from the heat source, i.e. the centre of the width of the specimen, receives the least heat input and hence, a lower misorientation in the subgrain boundaries that results in the region of the lowest dislocation density. The dislocation density increases towards the surface of the weld. This is reflected by the smaller dissipation at the centre, which increases as the edge is approached. The edge of the FZ1 dissipates more than the edge of the FZ 2 since FZ1 has a higher dislocation density. This is because the second pass deforms/hardens the region of the first pass that does not melt and introduces thermal stresses. In other words, plastic strain is developed in the first pass which means that the dislocation density is higher.

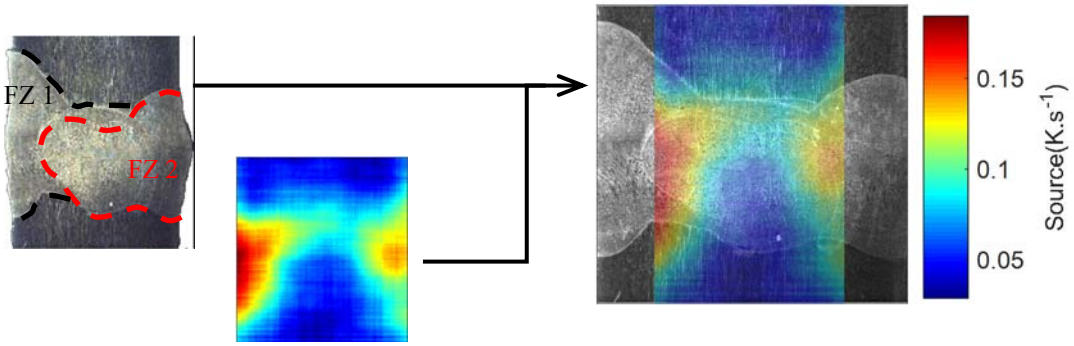

Figure 7.19 Dissipation at high resolution overlaid on weld macrograph.

7.7 Summary

The dissipative heat source distribution in the vicinity of welds is explored in this chapter. By using the reliable image processing procedure set out in Chapter 6, the dissipative heat source arising from welds were examined. Two welded specimens were successfully designed for this study. The requirements of the current study were taken into consideration when designing the welded specimen. The optical micrographs of the welded specimens were produced and their respective mechanical properties were also established by using DIC.

The preliminary work conducted using the autogenous TIG welded specimen showed that the dissipative heat source response is sensitive to the local microstructural condition. However, the specimen was unsuitable to be examined at high resolution. Taking into consideration of the inadequacies of the preliminary specimen, a second set of laser welded specimens was designed and manufactured to examine the dissipative heat source at higher resolution. A consistent result was obtained in that the results from low resolution and high resolution imaging were in agreement. At low resolution, the dissipation was found to be larger in the base metal followed by a gradual decrease approaching the heat affected zone and then a sharp rise as the weld centreline was reached. This was verified by the strain distribution obtained by the DIC. At higher resolution, the dissipative heat source was consistent with the expected dislocation density distribution of each region.

8 Conclusions and Future Work

8.1 Conclusions

The primary aim of the PhD was to characterise the dissipative heat source distribution in the vicinity of welds. This has arisen from the fact that dissipative heat source, calculated from the temperature rise caused by mechanical loading, is sensitive to the microstructure of a material. As such, the research was specifically focused on identifying the possibility of assessing the heterogeneity in microstructure in the vicinity of a weld using the dissipative heat source. The main conclusions of the work are summarised below:

1. In Chapter 2, a detailed review of the literature regarding the thermomechanical (thermoelastic and dissipative heat source) heat sources that are activated during mechanical loading of a material were presented. From the review, it was clear that the dissipative heat source is sensitive to microstructural changes in a material. However, it was shown that further research is necessary to elucidate the link between microstructure and energy dissipation. A review on the methodology for assessing the small heat sources (encountered during the elastic cyclic loading of metals) revealed that it is indeed possible to measure such small heat sources as demonstrated by Maquin and Pierron [13]. As the present work demands full-field heat source distribution, there is a need for integrating a spatial-temporal image processing procedure with the methodology provided in [13]. It is noteworthy that the image processing described in the literature have not been applied on a heterogeneous microstructure such as in the region of a weld. Therefore, it is evident that significant novel adaptation to both the experimental and data processing procedures described in the literature was required to obtain information related to the microstructure from the dissipative heat source.
2. Chapter 3 details the experimental aspects of the thesis where the infrared detector is used to obtain the very small temperature change that occurs in a material under cyclic load associated with the dissipative source. The temperature calibration implemented by the manufacturers was deemed inadequate for the present work as the spatial distribution of the resulting thermal data is less precise. It was demonstrated that this can be overcome by a pixel-by-pixel calibration that preserves the individual pixel behaviour thereby enabling accurate spatial distribution to be captured in the thermal data. The thermal resolution of the infrared detector was questionable due to the age of the infrared camera. It was shown using experimentally calculated NETD that the performance of the infrared camera matches that of the manufacturer's specification enabling accurate thermal measurements to be made. It is inevitable that heat exchanges occur between the specimen and its environment. It was also shown that the effects of these could be minimised by:

a. Isolating the measurement space from the surroundings by the use of a specially designed wooden chamber.
b. Using a reference specimen to eliminate any changes in the thermal environment inside the chamber.

3. Chapter 4 shows that the data processing method proposed in [13] can be implemented in conjunction with the experimental procedures to extract the small heat sources. Thus, a data processing routine based on the spatial averaging method in [13] was successfully developed. It was established that the spatial averaging method enabled the measurement of heat sources as low as $1mK.s^{-1}$. As subsequently demonstrated, this detection threshold is sufficient to detect the heat source of cyclic loading below the elastic limit of the material. Then, the sensitivity of the heat source to microstructural evolution was verified through the similarity between the evolutions of the heat source and plastic work obtained from simultaneous strain measurement for a material undergoing elastic plastic cyclic loading. The plastic work (arising from plastic strain) in this case is a measure of dislocation density.
4. Chapter 5 demonstrates the link between energy dissipation and microstructure using the spatial averaging procedure verified in Chapter 4 on test specimens with different known microstructures. Hence Chapter 5 confirms one of the research hypotheses of the PhD that the dissipative heat source can be utilised to identify difference in microstructure between different test specimens and provides a significant indication of the feasibility of using the dissipative heat source to characterise the heterogeneity in the weld microstructure. Further verification was obtained by assessing the difference in the test specimen microstructure using optical micrographs, the mechanical property, and the microhardness values.
5. Chapter 6 develops a spatial-temporal data processing procedure that incorporates key aspects of the image processing method proposed by Berthel *et al.* [17] into the methodology of established in Chapter 4, where the use of the reference specimen ensured a detection threshold that is low enough to capture the dissipative heat source. The procedure developed was also extended to higher spatial resolution through a modification of the experimental procedure that enables a closer imaging distance facilitated by the specially designed adaptable chamber. As rigid body motion is apparent at higher spatial resolution, the motion was compensated using a specially developed cross-correlation algorithm. The procedure was verified by extracting the thermoelastic and dissipative heat sources response from a non-uniform stress field (‘hole-in-plate’ specimen). In was shown that the dissipative heat source distribution was related to the stress field and that the thermoelastic source corresponded exactly to that predicted by an FE model of the stress field.
6. Chapter 7 shows that the full-field dissipative heat source distribution in the vicinity of a weld could be obtained using the procedures developed in the thesis on both a TIG welded specimen and a laser welded specimen. The results from the preliminary TIG welded specimen at low resolution showed that the dissipative heat sources was inhomogeneous in

a nominally uniform stress field. It was also shown that that the dissipative heat source distribution was very similar to the strain distribution observed under a static load obtained through DIC. In the laser welded specimens specifically designed to probe the dissipative heat source at higher spatial resolution, the dissipative heat source field was found to be connected to the dislocation density. The feasibility of using dissipative heat source to assess heterogeneity in the microstructure in the vicinity of a weld was confirmed.

8.2 Recommendations for future work

The results produced in this work relied heavily on the accuracy of the thermal data obtained. As such, the quality of the thermal data should be improved. Layers of thermal insulation were provided to protect the specimens from parasitic heat sources in the form of a chamber and a curtain. This leads to the eventual warming up of the camera environment. The effect of this has not been included when performing temperature calibration. It is possible that incorporating the effect of the change in camera housing temperature in the calibration process could lead to a more accurate thermal measurement. Naturally, the thermal measurements could also be improved by using an infrared detector with superior temperature resolution.

It was evident from the work that, even with a detection threshold in the order of tens of mK.s-1, it is difficult to produce the full-field dissipative heat source from purely elastic loading and achieving a purely non-destructive approach. One solution is to image with a higher resolution infrared camera. Notwithstanding this, the noise generated when calculating the spatial gradients will still persist. Recent works have suggested various ways to pre-filter the data before applying the image processing method. A detailed study is required to evaluate the effects of such pre-filtering (like Proper Orthogonal Decomposition [93] or Modal Decomposition [61]) on a heterogeneous field.

In terms of the dissipative heat source field obtained, a full verification of the results is still lacking. This is mainly due to the difficulty in obtaining complementary dislocation density measurement. A possible method to obtain complementary metallurgical data is Electron Backscatter Diffraction (EBSD). This would establish confidence in the results obtained and their interpretation. Additionally, the understanding of the exact nature of the dissipative heat source in a weld could only be obtained by studying the dissipative heat source arising from various different materials. Noting that phase transformation is not present in 316L stainless steel, there is still further avenue to explore the dissipative behaviour of materials with different phases.

Ultimately, it is envisaged that the development of this technique would result in a rapid non-contact microstructural analysis tool used in conjunction with other full-field measurement techniques such as DIC. In the case of a weld for instance, it could be used as a rapid way to assess strength of the weld with respect to its parent material or BM under cyclic loading for various welding parameters.

It is also possible that this technique may serve as a useful tool to assess the susceptibility of a weld to hydrogen embrittlement (or hydrogen induced cracking) since the presence of hydrogen is known to alter dislocation motion.

Therefore, the work described in this thesis has thereby demonstrated that, the dissipative heat source can be applied to the heterogeneity of the microstructure in a material using the weld microstructure as an example. The realisation of the dissipative heat source is the first significant step towards developing infrared thermography based dissipative heat source assessment as a potential non-destructive, full-field microstructural assessment tool capable of providing an insight into the material microstructure, particularly that of dislocation density.

Appendix A

A.1 Matlab Script for spatially averaged heat source calculation

```
close all; clear all; clc;

s.m_filename        = '360MPa_py360MPa.ptw'; % State the filename in the
form of 'Cpaturexxx.ptw'
s                   = RKF_ReadFileInfo(s); % Refer Richards code
cal                 = importdata('cal1200mus.mat',','); % Calibration
file for the appropriate integration time
ActuatorStartFrame  = 980; % Last frame before the start of the actuaor
f   = 350;
loadingf = 14;
newtime                 = linspace(0,s.m_lastframe/f,s.m_lastframe); %
Time variable

s.m_framepointer = 1;
s = RKF_ReadCroppedImage(s);
ref = s.m_data';
[X1 Y1 X2 Y2]   = getRoi(ref); % To select the area of the specimen:
resize and double click
[x1 y1 x2 y2]   = getRoi2(ref); % To select the area of the specimen:
resize and double click

% load and crop images
SP_temp = zeros([s.m_lastframe,Y2-Y1+1,X2-X1+1]);
REF_temp = zeros([s.m_lastframe,y2-y1+1,x2-x1+1]);
count = 0;%counter

for a = 1:s.m_lastframe; % Reads every image and stores them in an array

    s.m_framepointer = a;
    s = RKF_ReadCroppedImage(s);
    tmp = s.m_data';
    % crop and convert in Temperature
    SP_temp(a,:,:) = stuffcalPX(tmp(Y1:Y2,X1:X2),cal);
    REF_temp(a,:,:) = stuffcalPX(tmp(y1:y2,x1:x2),cal);

    if (a*100/s.m_lastframe >= count)
        fprintf('%i %% \t',count);
        count = count + 10;
    end;

end
fprintf('\n');

%-------------------------------------------------------------------------%
%-------------------------IMAGE SUBTRACTION-------------------------------%
%-------------------------------------------------------------------------%


theta_SP        = zeros(size(SP_temp)); % Creating a 2D theta for
specimen
```

```
for i = 1:s.m_lastframe; % 2D theta of the specimen

    theta_SP(i,:,:) = SP_temp(i,:,:) - SP_temp(ActuatorStartFrame,:,:); %
each frame subtracted by the last frame before start of the actuator

end

theta_REF = zeros(size(REF_temp)); % Creating a 2D theta for specimen

for i = 1:s.m_lastframe;

     theta_REF(i,:,:) = REF_temp(i,:,:) -
REF_temp(ActuatorStartFrame,:,:); % each frame subtracted by the last
frame before start of the actuator

end

theta_SP_1D     = mean(theta_SP,3); % Vertical profile of specimen
theta > for Laplacian
theta_SP_0D     = mean(theta_SP_1D,2); % Spatially averaged specimen
theta
theta_REF_0D    = mean(mean(theta_REF,2),3); % Spatially averaged
reference specimen theta
theta   = theta_SP_0D - theta_REF_0D; % Final theta (Uncomment for noise
floor)

%-------------------------------------------------------------------------%
%-----------------------------LAPLACIAN-----------------------------------%
%-------------------------------------------------------------------------%

x           = (2.3*10^-4:2.3*10^-4:2.3*10^-4*size(theta_SP_1D,2))'; %
Pixel size calculated

coeff_cond  = zeros(s.m_lastframe,1); % Initiate the conduction
coefficient variable

for i = 1:s.m_lastframe;

    cf              = fit(x,theta_SP_1D(i,:)','poly2'); % Second order
polynomial fitting of specimen vertical temperature profile
    polycoeff       = coeffvalues(cf); % Ouptut of the coefficients of
the second order polynomials
    coeff_cond(i,:) = 2*polycoeff(1,1); % Second derivative of the
polynomial

end

SmoothedLaplacian = mone(coeff_cond,151,3); % Smoothing the conduction
coefficient
SmoothedLaplacian = SmoothedLaplacian(ActuatorStartFrame+1:end); %
Extracting the smoothed conduction coefficient after the start of the
actuator



%-------------------------------------------------------------------------%
%---------------------THERMOELASTIC SUBTRACTION---------------------------%
%-------------------------------------------------------------------------%
```

```
s = RKF_ReadLISignal(s);
DL = s.LI;

delta_load          = DL - DL(ActuatorStartFrame);
trimmed_delta_load  = delta_load(ActuatorStartFrame:end);

trimmed_theta       = theta(ActuatorStartFrame:end);
theta_wodc          = PJS_removeDC(trimmed_theta);

newtime = (0:(s.m_lastframe-ActuatorStartFrame))/f;
ft = fit(newtime(500:3000)',trimmed_delta_load(500:3000)','fourier1');
c = coeffvalues(ft);
a1 = c(2);
b1 = c(3);

ft = fit(newtime(500:3000)',theta_wodc(500:3000),'fourier1');
c = coeffvalues(ft);
a2 = c(2);
b2 = c(3);

A = sqrt((b2^2+a2^2))/sqrt((b1^2+a1^2));
g1 = atan(abs(b1)/abs(a1));
g2 = atan(abs(b2)/abs(a2));
g = g1-g2;
gt = g/(2*pi*loadingf);


theta_th            = -A*trimmed_delta_load;
y = interp1(newtime,theta_th,newtime-gt);
sub_theta = trimmed_theta - y';


SmoothedTheta      = mone(sub_theta,151,3); % Smoothing the theta, enter
window size and number of passes

time = (0:(s.m_lastframe-ActuatorStartFrame))/f;
% SmoothedTheta       = mone(theta(ActuatorStartFrame:end),151,3); %for
noise



%-------------------------------------------------------------------------%
%-------------------------INITIAL GRADIENT--------------------------------%
%-------------------------------------------------------------------------%

linfit = fit((0:ActuatorStartFrame-
1)'/f,theta(1:ActuatorStartFrame,1),'poly1');
lfoutput = coeffvalues(linfit);
gradient = lfoutput(1,1);

%-------------------------------------------------------------------------%
%-------------------------TEMP DERIVATIVE---------------------------------%
%-------------------------------------------------------------------------%
%


dtheta      = diff(SmoothedTheta);
dt          = diff(time);

dtheta_dt   = dtheta./dt;
```

```
%-------------------------------------------------------------------------%
%-----------------------------DISSIPATION---------------------------------%
%-------------------------------------------------------------------------%

wch = (7900*500*(dtheta_dt-gradient))+(-
14*SmoothedLaplacian)+((8000*500*SmoothedTheta(2:end))/239);
wchdc_360MPa_py360MPa = wch/(8000*500);
```

A.2 Matlab script for pixel-by-pixel calibration

```
s.m_filename        = 'MUBv3_385_380MPa.ptw'; % State the filename in the
form of 'Cpaturexxx.ptw'
s                   = RKF_ReadFileInfo(s); % Refer Richards code
DL = zeros([s.m_lastframe,s.m_rows,s.m_cols]);

count = 0;%counter
for a = 1:s.m_lastframe % Reads every image and stores them in an array

    s.m_framepointer = a;
    s = RKF_ReadCroppedImage(s);
    DL(a,:,:) = s.m_data';


    if (a*100/s.m_lastframe >= count)
        fprintf('%i %% \t',count);
        count = count + 10;
    end

end


%
[dimt,dimx,dimy] = size(DL);
TempFit = zeros(dimt,dimx,dimy);

for i = 1:256
    for j = 1:320

        p = squeeze(P(:,i,j));
        mu = squeeze(MU(:,i,j));
        a = squeeze(DL(:,i,j));
        f = polyval(p,a,[],mu);
        TempFit(:,i,j) = f;

    end
end



BPRSize = length(DP);

for ino = 1:BPRSize

    [R,C] = ind2sub([dimx,dimy],DP(ino));
```

```
    TempFit(:,R,C) = NaN;
end

for ino = 1:BPRSize

[R,C] = ind2sub([dimx,dimy],DP(ino));

if R == 1

                if C == 1

                    neighbours = TempFit(:,R:R+1,C:C+1);
                    [DPz,DPx,DPy] = size(neighbours);
                    neighbours = permute(neighbours,[2 3 1]);
                    neighbours = reshape(neighbours,DPx*DPy,DPz);
                     neighbours(1,:) = [];
                    NeighbourMean = nanmean(neighbours);
                    TempFit(:,R,C) = NeighbourMean;

                    continue



                elseif C == 320

                    neighbours = Tfit(:,R:R+1,C-1:C);
                    [DPz,DPx,DPy] = size(neighbours);
                    neighbours = permute(neighbours,[2 3 1]);
                    neighbours = reshape(neighbours,DPx*DPy,DPz);
                    neighbours(2,:) = [];
                    NeighbourMean = nanmean(neighbours);
                    TempFit(:,R,C) = NeighbourMean;

                    continue

                else

                    neighbours = TempFit(:,R:R+1,C-1:C+1);
                    [DPz,DPx,DPy] = size(neighbours);
                    neighbours = permute(neighbours,[2 3 1]);
                    neighbours = reshape(neighbours,DPx*DPy,DPz);
                    neighbours(2,:) = [];
                    NeighbourMean = nanmean(neighbours);
                    TempFit(:,R,C) = NeighbourMean;

                    continue

                end

elseif R == 256

            if C == 1

                    neighbours = TempFit(:,R-1:R,C:C+1);
                    [DPz,DPx,DPy] = size(neighbours);
                    neighbours = permute(neighbours,[2 3 1]);
                    neighbours = reshape(neighbours,DPx*DPy,DPz);
```

```
                neighbours(3,:) = [];
                NeighbourMean = nanmean(neighbours);
                TempFit(:,R,C) = NeighbourMean;

                continue

        elseif C == 320

                neighbours = TempFit(R-1:R,C-1:C);
               [DPz,DPx,DPy] = size(neighbours);
                neighbours = permute(neighbours,[2 3 1]);
                neighbours = reshape(neighbours,DPx*DPy,DPz);
                neighbours(4,:) = [];
                NeighbourMean = nanmean(neighbours);
                TempFit(:,R,C) = NeighbourMean;

                continue

        else
                neighbours = TempFit(:,R-1:R,C-1:C+1);
                [DPz,DPx,DPy] = size(neighbours);
                neighbours = permute(neighbours,[2 3 1]);
                neighbours = reshape(neighbours,DPx*DPy,DPz);
                neighbours(5,:) = [];
                NeighbourMean = nanmean(neighbours);
                TempFit(:,R,C) = NeighbourMean;

                continue
        end




elseif C == 1

    neighbours = TempFit(:,R-1:R+1,C:C+1);
    [DPz,DPx,DPy] = size(neighbours);
    neighbours = permute(neighbours,[2 3 1]);
    neighbours = reshape(neighbours,DPx*DPy,DPz);
    neighbours(3,:) = [];
    NeighbourMean = nanmean(neighbours);
    TempFit(:,R,C) = NeighbourMean;

    continue



elseif C == 320

    neighbours = TempFit(:,R-1:R+1,C-1:C);
    [DPz,DPx,DPy] = size(neighbours);
    neighbours = permute(neighbours,[2 3 1]);
    neighbours = reshape(neighbours,DPx*DPy,DPz);
    neighbours(4,:) = [];
    NeighbourMean = nanmean(neighbours);
    TempFit(:,R,C) = NeighbourMean;

    continue
```

```
else
    neighbours = TempFit(:,R-1:R+1,C-1:C+1);
    [DPz,DPx,DPy] = size(neighbours);
    neighbours = permute(neighbours,[2 3 1]);
    neighbours = reshape(neighbours,DPx*DPy,DPz);
    neighbours(5,:) = [];
    NeighbourMean = nanmean(neighbours);
    TempFit(:,R,C) = NeighbourMean;
end

end
```

A.3 Matlab script for motion compensation

```
[dimt,dimy,dimx] = size(TempFit);

xvec = 1:dimx;
yvec = 1:dimy;

[Xgrid,Ygrid] = meshgrid(xvec,yvec);

FixIm = squeeze(TempFit(ActuatorStartFrame,:,:));
FixImEd = double(edge(FixIm,'log'));
XX = zeros(dimt,1);
YY = zeros(dimt,1);
MC_TempFit = zeros(dimt,dimy,dimx);

for lp = 1:(dimt-ActuatorStartFrame)
    MovIm           = squeeze(TempFit(lp+ActuatorStartFrame,:,:));
    MovImEd         = double(edge(MovIm,'log'));

    C               = xcorr2(FixImEd,MovImEd);

    [max_cc, imax]  = max(abs(C(:)));
    [ypeak, xpeak]  = ind2sub(size(C),imax(1));

    sqr             = 3;
    maxregion       = C(ypeak-sqr:ypeak+sqr,xpeak-sqr:xpeak+sqr);
    s               = regionprops(true(size(maxregion)), maxregion,
'WeightedCentroid');

    ym = ypeak-dimy+(sqr+1-s.WeightedCentroid(1));
    xm = xpeak-dimx+(sqr+1-s.WeightedCentroid(2));

    XX(lp,1) = xm;
    YY(lp,1) = ym;

    MC_TempFit(lp+ActuatorStartFrame,:,:) =
interp2(Xgrid,Ygrid,MovIm,Xgrid-xm,Ygrid-ym,'spline');
end
```

A.4 Matlab script for image processing procedure

A.4.1 Processing the thermal data

```
ActuatorStartFrame = 1289;
[dimt,dimx,dimy] = size(TempFit);

ref = squeeze(TempFit(1,:,:));
[X1 Y1 X2 Y2]   = getRoi(ref); % To select the area of the specimen:
resize and double click


% load and crop images
SP_temp = zeros([dimt,Y2-Y1+1,X2-X1+1]);

for ino = 1:dimt

    SP_temp(ino,:,:) = squeeze(TempFit(ino,Y1:Y2,X1:X2));

end




[x1 y1 x2 y2]   = getRoi2(ref); % To select the area of the specimen:
resize and double click
REF_temp = zeros([dimt,y2-y1+1,x2-x1+1]);

for ino = 1:dimt


    REF_temp(ino,:,:) = squeeze(TempFit(ino,y1:y2,x1:x2));
end
clearvars TempFit


%-------------------------------------------------------------------------%
%-------------------------IMAGE SUBTRACTION-------------------------------%
%-------------------------------------------------------------------------%


theta_SP        = zeros([dimt,Y2-Y1+1,X2-X1+1]); % Creating a 2D theta
for specimen

for i = 1:dimt % 2D theta of the specimen

    theta_SP(i,:,:) = SP_temp(i,:,:) - SP_temp(ActuatorStartFrame,:,:); %
each frame subtracted by the last frame before start of the actuator

end

theta_REF = zeros([dimt,y2-y1+1,x2-x1+1]); % Creating a 2D theta for
specimen
```

```
for i = 1:dimt

     theta_REF(i,:,:) = REF_temp(i,:,:) -
REF_temp(ActuatorStartFrame,:,:); % each frame subtracted by the last
frame before start of the actuator

end

theta_REF_0D    = mean(mean(theta_REF,2),3); % Spatially averaged
reference specimen theta

clearvars SP_temp REF_temp

%--------------------------------------------------------------------------%
%----------------------------GENERATE THETA--------------------------------%
%--------------------------------------------------------------------------%

clearvars theta_REF


theta       = zeros([dimt,Y2-Y1+1,X2-X1+1]);

y = Y2-Y1+1;
z = X2-X1+1;

for i = 1:y
    for j = 1:z
        theta(:,i,j) = squeeze(theta_SP(:,i,j))-theta_REF_0D;
    end
end
```

A.4.2 Generating the shape matrix

```
SF = [0 0;0 1;0 2;1 0;1 1;2 0];
f = 14;
delta_t = 1/350;
M_sf = zeros(6,6);
x = 32;
y = 32;
u = 37;
vu = -u:u;


for i = 1:6
    for j = 1:6
        for vx = -x:x
            for vy = -y:y
        M_sf(i,j) =
M_sf(i,j)+(vx.^(SF(i,1)+SF(j,1))*vy.^(SF(i,2)+SF(j,2)));
            end
        end
    end
end
```

```
M_11 = sum(vu.^2);
M_13 = sum(vu.*sin(2*pi*f*vu*delta_t));
M_22 = 2*u+1;
M_24 = sum(cos(2*pi*f*vu*delta_t));
M_33 = sum(sin(2*pi*f*vu*delta_t).*sin(2*pi*f*vu*delta_t));
M_44 = sum(cos(2*pi*f*vu*delta_t).*cos(2*pi*f*vu*delta_t));

M = zeros(24,24);

M1 = M_11*M_sf;
M2 = M_22*M_sf;
M3 = M_33*M_sf;
M4 = M_44*M_sf;
M5 = M_13*M_sf;
M6 = M_24*M_sf;

M(1:6,1:6) = M1;
M(1:6,13:18) = M5;
M(7:12,7:12) = M2;
M(7:12,19:24) = M6;
M(13:18,13:18) = M3;
M(13:18,1:6) = M5;
M(19:24,7:12) = M6;
M(19:24,19:24) = M4;

M = sparse(M);
```

A.4.3 Calculating the dissipative heat source

```
tic

count = 0;
loadingf = 14;
delta_t = 1/350;
tc = round((1/delta_t)*0.6);

x = 1;
y = 1;
t = 1;
td=1;

u0 = 37;
i0 = 32;
j0 = 32;

Nt = 2*u0+1;
Nx = 2*i0+1;
Ny = 2*j0+1;

InitialVar = theta(ActuatorStartFrame-tc-u0:ActuatorStartFrame-
tc+u0,:,:);
TestVar = theta(ActuatorStartFrame:end,:,:);
[dimt,dimy,dimx] = size(TestVar);
Totalt = floor(dimt/Nt);

VarName = TestVar(1:(Totalt*Nt),:,:);
```

```
[i,j]=meshgrid(-i0:i0,-j0:j0);
ij1 = i.^SF(1,1).*j.^SF(1,2);
ij2 = i.^SF(2,1).*j.^SF(2,2);
ij3 = i.^SF(3,1).*j.^SF(3,2);
ij4 = i.^SF(4,1).*j.^SF(4,2);
ij5 = i.^SF(5,1).*j.^SF(5,2);
ij6 = i.^SF(6,1).*j.^SF(6,2);



u_mat1 = zeros(2*u0+1,2*j0+1,2*i0+1);
u_mat3 = zeros(2*u0+1,2*j0+1,2*i0+1);
u_mat4 = zeros(2*u0+1,2*j0+1,2*i0+1);

for i = -u0:u0
    u_mat1(i+u0+1,:,:) = i;
    u_mat3(i+u0+1,:,:) = sin(2*pi*loadingf*i*delta_t);
    u_mat4(i+u0+1,:,:) = cos(2*pi*loadingf*i*delta_t);
end




for i = -u0:u0
    u_mat1(i+u0+1,:,:) = i;
    u_mat3(i+u0+1,:,:) = sin(2*pi*loadingf*i*delta_t);
    u_mat4(i+u0+1,:,:) = cos(2*pi*loadingf*i*delta_t);
end

b1_1 = zeros(2*u0+1,2*j0+1,2*i0+1);
b1_2 = zeros(2*u0+1,2*j0+1,2*i0+1);
b1_3 = zeros(2*u0+1,2*j0+1,2*i0+1);
b1_4 = zeros(2*u0+1,2*j0+1,2*i0+1);
b1_5 = zeros(2*u0+1,2*j0+1,2*i0+1);
b1_6 = zeros(2*u0+1,2*j0+1,2*i0+1);

b2_1 = zeros(2*u0+1,2*j0+1,2*i0+1);
b2_2 = zeros(2*u0+1,2*j0+1,2*i0+1);
b2_3 = zeros(2*u0+1,2*j0+1,2*i0+1);
b2_4 = zeros(2*u0+1,2*j0+1,2*i0+1);
b2_5 = zeros(2*u0+1,2*j0+1,2*i0+1);
b2_6 = zeros(2*u0+1,2*j0+1,2*i0+1);

b3_1 = zeros(2*u0+1,2*j0+1,2*i0+1);
b3_2 = zeros(2*u0+1,2*j0+1,2*i0+1);
b3_3 = zeros(2*u0+1,2*j0+1,2*i0+1);
b3_4 = zeros(2*u0+1,2*j0+1,2*i0+1);
b3_5 = zeros(2*u0+1,2*j0+1,2*i0+1);
b3_6 = zeros(2*u0+1,2*j0+1,2*i0+1);

b4_1 = zeros(2*u0+1,2*j0+1,2*i0+1);
b4_2 = zeros(2*u0+1,2*j0+1,2*i0+1);
b4_3 = zeros(2*u0+1,2*j0+1,2*i0+1);
b4_4 = zeros(2*u0+1,2*j0+1,2*i0+1);
b4_5 = zeros(2*u0+1,2*j0+1,2*i0+1);
b4_6 = zeros(2*u0+1,2*j0+1,2*i0+1);

for i = -u0:u0

    b1_1(i+u0+1,:,:) = ij1.*squeeze(u_mat1(i+u0+1,:,:));
    b1_2(i+u0+1,:,:) = ij2.*squeeze(u_mat1(i+u0+1,:,:));
```

```
    b1_3(i+u0+1,:,:) = ij3.*squeeze(u_mat1(i+u0+1,:,:));
    b1_4(i+u0+1,:,:) = ij4.*squeeze(u_mat1(i+u0+1,:,:));
    b1_5(i+u0+1,:,:) = ij5.*squeeze(u_mat1(i+u0+1,:,:));
    b1_6(i+u0+1,:,:) = ij6.*squeeze(u_mat1(i+u0+1,:,:));

    b2_1(i+u0+1,:,:) = ij1;
    b2_2(i+u0+1,:,:) = ij2;
    b2_3(i+u0+1,:,:) = ij3;
    b2_4(i+u0+1,:,:) = ij4;
    b2_5(i+u0+1,:,:) = ij5;
    b2_6(i+u0+1,:,:) = ij6;

    b3_1(i+u0+1,:,:) = ij1.*squeeze(u_mat3(i+u0+1,:,:));
    b3_2(i+u0+1,:,:) = ij2.*squeeze(u_mat3(i+u0+1,:,:));
    b3_3(i+u0+1,:,:) = ij3.*squeeze(u_mat3(i+u0+1,:,:));
    b3_4(i+u0+1,:,:) = ij4.*squeeze(u_mat3(i+u0+1,:,:));
    b3_5(i+u0+1,:,:) = ij5.*squeeze(u_mat3(i+u0+1,:,:));
    b3_6(i+u0+1,:,:) = ij6.*squeeze(u_mat3(i+u0+1,:,:));

    b4_1(i+u0+1,:,:) = ij1.*squeeze(u_mat4(i+u0+1,:,:));
    b4_2(i+u0+1,:,:) = ij2.*squeeze(u_mat4(i+u0+1,:,:));
    b4_3(i+u0+1,:,:) = ij3.*squeeze(u_mat4(i+u0+1,:,:));
    b4_4(i+u0+1,:,:) = ij4.*squeeze(u_mat4(i+u0+1,:,:));
    b4_5(i+u0+1,:,:) = ij5.*squeeze(u_mat4(i+u0+1,:,:));
    b4_6(i+u0+1,:,:) = ij6.*squeeze(u_mat4(i+u0+1,:,:));

end

B = zeros(24,1);
P = zeros(24,1);
I = -i0:i0;
J = -j0:j0;
sumI = sum(I.^2);
sumJ = sum(J.^2);
delx2 = (5.2*10^-5)^2;
dely2 = (5.2*10^-5)^2;
rho = 7900;
C = 500;
k = 15;
tau = 360;
dhri   = zeros(dimy-Ny+1,dimx-Nx+1);


for n = 1:(dimy-Ny+1)*(dimx-Nx+1)

    Var = InitialVar(:,y:y+Ny-1,x:x+Nx-1);

    B1 = Var.*b1_1;
    B2 = Var.*b1_2;
    B3 = Var.*b1_3;
    B4 = Var.*b1_4;
    B5 = Var.*b1_5;
    B6 = Var.*b1_6;
    B7 = Var.*b2_1;
    B8 = Var.*b2_2;
    B9 = Var.*b2_3;
    B10 = Var.*b2_4;
    B11 = Var.*b2_5;
    B12 = Var.*b2_6;
    B13 = Var.*b3_1;
    B14 = Var.*b3_2;
    B15 = Var.*b3_3;
```

```
    B16 = Var.*b3_4;
    B17 = Var.*b3_5;
    B18 = Var.*b3_6;
    B19 = Var.*b4_1;
    B20 = Var.*b4_2;
    B21 = Var.*b4_3;
    B22 = Var.*b4_4;
    B23 = Var.*b4_5;
    B24 = Var.*b4_6;

    B(1) = sum(B1(:));
    B(2) = sum(B2(:));
    B(3) = sum(B3(:));
    B(4) = sum(B4(:));
    B(5) = sum(B5(:));
    B(6) = sum(B6(:));
    B(7) = sum(B7(:));
    B(8) = sum(B8(:));
    B(9) = sum(B9(:));
    B(10) = sum(B10(:));
    B(11) = sum(B11(:));
    B(12) = sum(B12(:));
    B(13) = sum(B13(:));
    B(14) = sum(B14(:));
    B(15) = sum(B15(:));
    B(16) = sum(B16(:));
    B(17) = sum(B17(:));
    B(18) = sum(B18(:));
    B(19) = sum(B19(:));
    B(20) = sum(B20(:));
    B(21) = sum(B21(:));
    B(22) = sum(B22(:));
    B(23) = sum(B23(:));
    B(24) = sum(B24(:));

    P = M\B;

    dhri(y,x)   = 1/delta_t*((P(3)*sumI/Nx)+(P(6)*sumJ/Ny)+P(1));


    x = x + 1;

    if x == dimx-Nx+2
        y = y + 1;
        x = 1;
    end
end

x = 1;
y = 1;
t = 1;
dhr   = zeros(Totalt,dimy-Ny+1,dimx-Nx+1);
dcond = zeros(Totalt,dimy-Ny+1,dimx-Nx+1);
drad  = zeros(Totalt,dimy-Ny+1,dimx-Nx+1);

for n = 1:(Totalt)*(dimy-Ny+1)*(dimx-Nx+1)

    Var = VarName(t:t+Nt-1,y:y+Ny-1,x:x+Nx-1);

    B1 = Var.*b1_1;
    B2 = Var.*b1_2;
    B3 = Var.*b1_3;
```

```
B4 = Var.*b1_4;
B5 = Var.*b1_5;
B6 = Var.*b1_6;
B7 = Var.*b2_1;
B8 = Var.*b2_2;
B9 = Var.*b2_3;
B10 = Var.*b2_4;
B11 = Var.*b2_5;
B12 = Var.*b2_6;
B13 = Var.*b3_1;
B14 = Var.*b3_2;
B15 = Var.*b3_3;
B16 = Var.*b3_4;
B17 = Var.*b3_5;
B18 = Var.*b3_6;
B19 = Var.*b4_1;
B20 = Var.*b4_2;
B21 = Var.*b4_3;
B22 = Var.*b4_4;
B23 = Var.*b4_5;
B24 = Var.*b4_6;

B(1) = sum(B1(:));
B(2) = sum(B2(:));
B(3) = sum(B3(:));
B(4) = sum(B4(:));
B(5) = sum(B5(:));
B(6) = sum(B6(:));
B(7) = sum(B7(:));
B(8) = sum(B8(:));
B(9) = sum(B9(:));
B(10) = sum(B10(:));
B(11) = sum(B11(:));
B(12) = sum(B12(:));
B(13) = sum(B13(:));
B(14) = sum(B14(:));
B(15) = sum(B15(:));
B(16) = sum(B16(:));
B(17) = sum(B17(:));
B(18) = sum(B18(:));
B(19) = sum(B19(:));
B(20) = sum(B20(:));
B(21) = sum(B21(:));
B(22) = sum(B22(:));
B(23) = sum(B23(:));
B(24) = sum(B24(:));

P = M\B;

dhr(td,y,x)   = 1/delta_t*((P(3)*sumI/Nx)+(P(6)*sumJ/Ny)+P(1));
dcond(td,y,x) = ((-2*k)/(rho*C))*((P(9)/delx2)+(P(12)/dely2));
drad(td,y,x)  = ((P(9)*sumI/Nx)+(P(12)*sumJ/Ny)+P(7))*1/tau;

x = x + 1;

if x == dimx-Nx+2
    y = y + 1;
    x = 1;
end

if y == dimy-Ny+2
    t = t + Nt;
    td = td + 1;
```

```
        x = 1;
        y = 1;
    end


    if (n*100/((Totalt)*(dimy-Ny+1)*(dimx-Nx+1)) >= count)
        fprintf('%i %% \t',count);
        count = count + 10;
    end
end



dhrt   = zeros(Totalt,dimy-Ny+1,dimx-Nx+1);

for i = 1:size(dhr,1)
dhrt(i,:,:) = squeeze(dhr(i,:,:))-dhri;
end

df = dhrt+dcond+drad;
```

List of References

[1] J. M. Dulieu-Barton, "Thermoelastic stress analysis", in *Optical Methods for Solid Mechanics: A Full-Field Approach*, First ed New York: John Wiley & Sons, 2012, pp. 345-366.

[2] R. C. Tighe, G. P. Howell, J. P. Tyler, S. Lormor, and J. M. Dulieu-Barton, "Stress based non-destructive evaluation using thermographic approaches: From laboratory trials to on-site assessment", *NDT & E International,* vol. 84, pp. 76-88, 2016.

[3] G. Howell, "Identification of plastic strain using thermoelastic stress analysis", PhD Thesis, University of Southampton, 2017.

[4] E. Chevallier, "Assessment of welding induced plastic strain using the thermoelastic stress analysis technique", PhD Thesis, University of Southampton, 2018.

[5] N. Connesson, F. Maquin, and F. Pierron, "Dissipated energy measurements as a marker of microstructural evolution: 316L and DP600", *Acta Materialia,* vol. 59, pp. 4100-4115, 2011.

[6] N. Connesson, F. Maquin, and F. Pierron, "Experimental Energy Balance During the First Cycles of Cyclically Loaded Specimens Under the Conventional Yield Stress", *Experimental Mechanics,* vol. 51, pp. 23-44, 2010.

[7] W. Farren and G. I. Taylor, "The heat developed during plastic extension of metals", *Proceedings of the Royal Society of London. Series A, Containing Papers of a Mathematical and Physical Character,* vol. 107, pp. 422-451, 1925.

[8] J. Dulieu-Barton and P. Stanley, "Development and applications of thermoelastic stress analysis", *The Journal of Strain Analysis for Engineering Design,* vol. 33, pp. 93-104, 1998.

[9] A. Chrysochoos and J. C. Dupre, "An infrared set-up for continuum thermomechanics", presented at the QIRT, Château-Malabry, France, 1992.

[10] H. Louche and A. Chrysochoos, "Thermal and dissipative effects accompanying Lüders band propagation", *Materials Science and Engineering: A,* vol. 307, pp. 15-22, 2001.

[11] S. A. David, S. S. Babu, and J. M. Vitek, "Welding: Solidification and microstructure", *JOM,* vol. 55, pp. 14-20, June 01 2003.

[12] W. Guo, S. Dong, W. Guo, J. A. Francis, and L. Li, "Microstructure and mechanical characteristics of a laser welded joint in SA508 nuclear pressure vessel steel", *Materials Science and Engineering: A,* vol. 625, pp. 65-80, 2015.

[13] F. Maquin and F. Pierron, "Refined experimental methodology for assessing the heat dissipated in cyclically loaded materials at low stress levels", *Comptes Rendus Mécanique,* vol. 335, pp. 168-174, 2007.

[14] V. Crupi, E. Guglielmino, A. Risitano, and D. Taylor, "Different methods for fatigue assessment of T welded joints used in ship structures", *Journal of ship research,* vol. 51, pp. 150-159, 2007.

[15] H.-w. Yang, Z.-q. Cui, W.-x. Wang, B.-s. Xu, and H.-y. Xu, "Fatigue behavior of AZ31B magnesium alloy electron beam welded joint based on infrared thermography", *Transactions of Nonferrous Metals Society of China,* vol. 26, pp. 2595-2602, 2016.

[16] M. Facchinetti, P. Florin, C. Doudard, and S. Calloch, "Identification of Self-Heating Phenomena Under Cyclic Loadings Using Full-Field Thermal and Kinematic Measurements: Application to High-Cycle Fatigue of Seam Weld Joints", *Experimental Mechanics,* vol. 55, pp. 681-698, 2014.

[17] B. Berthel, A. Chrysochoos, B. Wattrisse, and A. Galtier, "Infrared Image Processing for the Calorimetric Analysis of Fatigue Phenomena", *Experimental Mechanics,* vol. 48, pp. 79-90, 2007.

[18] T. Ummenhofer and J. Medgenberg, "On the use of infrared thermography for the analysis of fatigue damage processes in welded joints", *International Journal of Fatigue,* vol. 31, pp. 130-137, 2009.

[19] P. Florin, M. Facchinetti, C. Doudard, and S. Calloch, "Fast Fatigue Properties Identification by “Self-heating” Method: Application to Automotive Welded Joints", *Procedia Engineering,* vol. 66, pp. 676-683, 2013.

[20] T. Boulanger, A. Chrysochoos, C. Mabru, and A. Galtier, "Calorimetric analysis of dissipative and thermoelastic effects associated with the fatigue behavior of steels", *International Journal of Fatigue,* vol. 26, pp. 221-229, 2004.

[21] J. Lemaitre and J.-L. Chaboche, *Mechanics of solid materials*, First ed. New York, USA: Cambridge University Press, 1994.

[22] W. Thomson, "XV.—On the Dynamical Theory of Heat, with numerical results deduced from Mr Joule's Equivalent of a Thermal Unit, and M. Regnault's Observations on Steam", *Transactions of the Royal Society of Edinburgh,* vol. 20, pp. 261-288, 1853.

[23] M. H. Belgen, "Structural stress measurements with an infrared radiometer", *ISA transactions,* vol. 6, pp. 49-53, 1967.

[24] A. Machin, J. Sparrow, and M. Stimson, "Mean stress dependence of the thermoelastic constant", *Strain,* vol. 23, pp. 27-30, 1987.

[25] A. K. Wong, J. G. Sparrow, and S. A. Dunn, "On the Revised Theory of Thermoelastic Effect", *Journal of Physics And Chemistry of Solids,* vol. 49, pp. 395-400, 1988.

[26] R. Tomlinson and E. Olden, "Thermoelasticity for the analysis of crack tip stress fields—a review", *Strain,* vol. 35, pp. 49-55, 1999.

[27] R. K. Fruehmann, J. M. Dulieu-Barton, and S. Quinn, "On the thermoelastic response of woven composite materials", *The Journal of Strain Analysis for Engineering Design,* vol. 43, pp. 435-450, 2008.

[28] T. Sakagami, Y. Izumi, N. Mori, and S. Kubo, "Development of self-reference lock-in thermography and its application to remote nondestructive inspection of fatigue cracks in steel bridges", *Quantitative InfraRed Thermography Journal,* vol. 7, pp. 73-84, 2010.

[29] D. Palumbo and U. Galietti, "Characterisation of steel welded joints by infrared thermographic methods", *Quantitative InfraRed Thermography Journal,* vol. 11, pp. 29-42, 2014.

[30] A. K. Wong, S. A. Dunn, and J. G. Sparrow, "Residual stress measurement by means of the thermoelastic effect", *Nature,* vol. 332, pp. 613-615, 1988.

[31] J. Eaton-Evans, J. M. Dulieu-Barton, E. G. Little, and I. A. Brown, "Thermoelastic studies on Nitinol stents", *The Journal of Strain Analysis for Engineering Design,* vol. 41, pp. 481-495, 2006.

[32] A. L. Gyekenyesi, "Thermoelastic stress analysis: an NDE tool for residual stress assessment of metallic alloys", *Journal of engineering for gas turbines and power,* vol. 124, pp. 383-387, 2002.

[33] A. F. Robinson, "Assessment of residual stress using thermoelastic stress analysis", PhD Thesis, University of Southampton, 2011.

[34] S. Quinn, J. Dulieu-Barton, and J. Langlands, "Progress in thermoelastic residual stress measurement", *Strain,* vol. 40, pp. 127-133, 2004.

[35] R. S. Lakes, *Viscoelastic materials*: Cambridge University Press, 2009.

[36] J. Snoek, "Effect of small quantities of carbon and nitrogen on the elastic and plastic properties of iron", *Physica,* vol. 8, pp. 711-733, 1941.

[37] T. i.-S. Kê, "Experimental Evidence of the Viscous Behavior of Grain Boundaries in Metals", *Physical Review,* vol. 71, pp. 533-546, 1947.

[38] S. Asano, "Theory of nonlinear damping due to dislocation hysteresis", *Journal of the Physical Society of Japan,* vol. 29, pp. 952-963, 1970.

[39] F. Maquin and F. Pierron, "Heat dissipation measurements in low stress cyclic loading of metallic materials: From internal friction to micro-plasticity", *Mechanics of Materials,* vol. 41, pp. 928-942, 2009.

[40] C. Mareau, V. Favier, B. Weber, A. Galtier, and M. Berveiller, "Micromechanical modeling of the interactions between the microstructure and the dissipative deformation mechanisms in steels under cyclic loading", *International Journal of Plasticity,* vol. 32-33, pp. 106-120, 2012.

[41] R. Peierls, "The size of a dislocation", *Proceedings of the Physical Society,* vol. 52, p. 34, 1940.

[42] F. Nabarro, "Dislocations in a simple cubic lattice", *Proceedings of the Physical Society,* vol. 59, p. 256, 1947.

[43] A. Granato and K. Lücke, "Theory of Mechanical Damping Due to Dislocations", *Journal of Applied Physics,* vol. 27, p. 583, 1956.

[44] F. C. Frank and W. T. Read, "Multiplication Processes for Slow Moving Dislocations", *Physical Review,* vol. 79, pp. 722-723, 1950.

[45] C. Stromeyer, "The determination of fatigue limits under alternating stress conditions", *Proc. R. Soc. Lond. A,* vol. 90, pp. 411-425, 1914.

[46] H. Moore and J. Kommers, "Fatigue of metals under repeated stress", *Chemical and Metallurgical Engineering,* vol. 25, pp. 1141-1144, 1921.

[47] J. Charles, F. Appl, and J. Francis, "Using the scanning infrared camera in experimental fatigue studies", *Experimental mechanics,* vol. 15, pp. 133-138, 1975.

[48] M. P. Luong, "Infrared thermography of fatigue in metals", in *Thermosense XIV*, 1992, pp. 222-233.

[49] M. P. Luong, "Fatigue limit evaluation of metals using an infrared thermographic technique", *Mechanics of materials,* vol. 28, pp. 155-163, 1998.

[50] G. Fargione, A. Geraci, G. La Rosa, and A. Risitano, "Rapid determination of the fatigue curve by the thermographic method", *International Journal of Fatigue,* vol. 24, pp. 11-19, 2002.

[51] F. Cura, G. Curti, and R. Sesana, "A new iteration method for the thermographic determination of fatigue limit in steels", *International Journal of Fatigue,* vol. 27, pp. 453-459, 2005.

[52] R. de Finis, D. Palumbo, M. M. da Silva, and U. Galietti, "Is the temperature plateau of a self-heating test a robust parameter to investigate the fatigue limit of steels with thermography?", *Fatigue & Fracture of Engineering Materials & Structures,* 2017.

[53] V. Crupi, E. Guglielmino, M. Maestro, and A. Marinò, "Fatigue analysis of butt welded AH36 steel joints: Thermographic Method and design S–N curve", *Marine Structures,* vol. 22, pp. 373-386, 2009.

[54] G. Meneghetti, "Analysis of the fatigue strength of a stainless steel based on the energy dissipation", *International Journal of Fatigue,* vol. 29, pp. 81-94, 2007.

[55] N. Torabian, V. Favier, S. Ziaei-Rad, J. Dirrenberger, F. Adamski, and N. Ranc, "Thermal response of DP600 dual-phase steel under ultrasonic fatigue loading", *Materials Science and Engineering: A,* vol. 677, pp. 97-105, 2016.

[56] A. E. Morabito, A. Chrysochoos, V. Dattoma, and U. Galietti, "Analysis of thermoelastic and dissipative effects related to the fatigue of 2024 T3 aluminium alloy", *Quantitative InfraRed Thermography Journal,* vol. 1, pp. 99-116, 2004.

[57] N. Connesson, "Contribution à l'étude du comportement thermomécanique de matériaux métalliques", PhD Thesis, Université de Technologie de Troyes, 2010.

[58] A. Chrysochoos and H. Louche, "An infrared image processing to analyse the calorific effects accompanying strain localisation", *International Journal of Engineering Science,* vol. 38, pp. 1759-1788, 2000.

[59] A. Benaarbia and A. Chrysochoos, "Proper orthogonal decomposition preprocessing of infrared images to rapidly assess stress-induced heat source fields", *Quantitative InfraRed Thermography Journal,* pp. 1-21, 2017.

[60] D. Delpueyo, X. Balandraud, and M. Grédiac, "Heat source reconstruction from noisy temperature fields using an optimised derivative Gaussian filter", *Infrared Physics & Technology,* vol. 60, pp. 312-322, 2013.

[61] T. Pottier, H. Louche, S. Samper, H. Favreliĕre, F. Toussaint, and P. Vacher, "Proposition of a modal filtering method to enhance heat source computation within heterogeneous thermomechanical problems", *International Journal of Engineering Science,* vol. 81, pp. 163-176, 2014.

[62] T. Pottier, M. P. Moutrille, J. B. Le Cam, X. Balandraud, and M. Grédiac, "Study on the Use of Motion Compensation Techniques to Determine Heat Sources. Application to Large Deformations on Cracked Rubber Specimens", *Experimental Mechanics,* vol. 49, pp. 561-574, 2008.

[63] M. L. Pastor, X. Balandraud, M. Grédiac, and J. L. Robert, "Applying infrared thermography to study the heating of 2024-T3 aluminium specimens under fatigue loading", *Infrared Physics & Technology,* vol. 51, pp. 505-515, 2008.

[64] H. Louche, P. Vacher, and R. Arrieux, "Thermal observations associated with the Portevin–Le Châtelier effect in an Al–Mg alloy", *Materials Science and Engineering: A,* vol. 404, pp. 188-196, 2005.

[65] D. Delpueyo, X. Balandraud, and M. Grédiac, "Applying infrared thermography to analyse martensitic microstructures in a Cu–Al–Be shape-memory alloy subjected to a cyclic loading", *Materials Science and Engineering: A,* vol. 528, pp. 8249-8258, 2011.

[66] M. Vollmer and K.-P. Möllmann, *Infrared thermal imaging: fundamentals, research and applications*, First ed. New York: John Wiley & Sons, 2010.

[67] M. Schulz and L. Caldwell, "Nonuniformity correction and correctability of infrared focal plane arrays", *Infrared Physics & Technology,* vol. 36, pp. 763-777, 1995.

[68] V. Honorat, S. Moreau, J. M. Muracciole, B. Wattrisse, and A. Chrysochoos, "Calorimetric analysis of polymer behaviour using a pixel calibration of an IRFPA camera", *Quantitative InfraRed Thermography Journal,* vol. 2, pp. 153-171, 2005.

[69] H. Pron and T. Bouache, "Alternative thermal calibrations of focal plane array infrared cameras", *Quantitative InfraRed Thermography Journal,* vol. 13, pp. 94-108, 2016.

[70] N. S. Kopeika, *A system engineering approach to imaging*: SPIE press, 1998.

[71] H. Pron and C. Bissieux, "Focal plane array infrared cameras as research tools", *Quantitative InfraRed Thermography Journal,* vol. 1, pp. 229-240, 2004.

[72] A. Robinson, J. Dulieu-Barton, S. Quinn, and R. Burguete, "Paint coating characterization for thermoelastic stress analysis of metallic materials", *Measurement Science and Technology,* vol. 21, p. 085502, 2010.

[73] P. Seelan, J. Dulieu-Barton, and F. Pierron, "The Effect of Microstructure on Energy Dissipation in 316L Stainless Steel", in *Residual Stress, Thermomechanics & Infrared Imaging, Hybrid Techniques and Inverse Problems, Volume 9*, ed: Springer, 2017, pp. 15-19.

[74] J. Fan, X. Guo, C. Wu, V. Crupi, and E. Guglielmino, "Influence of Heat Treatments on Mechanical Behavior of FV520B Steel", *Experimental Techniques,* vol. 39, pp. 55-64, 2015.

[75] W. F. Hosford, *Mechanical Behavior of Materials*, First ed. Cambridge: Cambridge University Press, 2005.

[76] J. Schijve, *Fatigue of structures and materials*, First ed. USA: Springer, 2001.

[77] C. Donadille, R. Valle, P. Dervin, and R. Penelle, "Development of texture and microstructure during cold-rolling and annealing of FCC alloys: Example of an austenitic stainless steel", *Acta metallurgica,* vol. 37, pp. 1547-1571, 1989.

[78] G. J. Hopkin, "Modelling Anisothermal Recrystallization in Austenitic Stainless Steels", PhD Thesis, University of Cambridge, 2002.

[79] A. E407-07, "Standard Practice for Microetching Metals and Alloys", ed: ASTM International West Conshohocken, PA, 2015.

[80] B. Berthel, "Mesures thermographiques de champs de dissipation accompagnant la fatigue à grand nombre de cycles des aciers", Université Montpellier II-Sciences et Techniques du Languedoc, 2007.

[81] R. Urbanek and J. Bär, "Influence of motion compensation on lock-In thermographic investigations of fatigue crack propagation", *Engineering Fracture Mechanics,* vol. 183, pp. 13-25, 2017.

[82] W. Wang, R. K. Fruehmann, and J. M. Dulieu-Barton, "Application of Digital Image Correlation to Address Complex Motions in Thermoelastic Stress Analysis", *Strain,* vol. 51, pp. 405-418, 2015.

[83] J. C. Lippold, *Welding metallurgy and weldability*, First ed. New Jersey, USA: John Wiley & Sons, 2014.

[84] W. Savage, E. Nippes, and E. Szekeres, "Study of weld interface phenomena in a low alloy steel", *Welding Journal,* vol. 55, pp. 260s–268s, 1976.

[85] S. Kalpakjian, *Manufacturing engineering and technology*: Pearson Education India, 2001.

[86] E. Folkhard, *Welding metallurgy of stainless steels*: Springer Science & Business Media, 2012.

[87] J. Foulds, J. Moteff, V. Sikka, and J. McEnerney, "Deformation behavior of a 16-8-2 GTA weld as influenced by its solidification substructure", *Metallurgical Transactions A,* vol. 14, pp. 1357-1366, 1983.

[88] J. Foulds and J. Moteff, "Substructure Characterization of a 16-8-2 GTA weld through transmission electron microscopy", *Welding Tournal Research Supplement,* vol. 61, pp. 189-196s, 1982.

[89] P. Molian, "Solidification behaviour of laser welded stainless steel", *Journal of Materials Science Letters,* vol. 4, pp. 281-283, 1985.

[90] B. Boyce, P. Reu, and C. Robino, "The constitutive behavior of laser welds in 304L stainless steel determined by digital image correlation", *Metallurgical and Materials Transactions A,* vol. 37, pp. 2481-2492, 2006.

[91] A.-M. El-Batahgy, "Effect of laser welding parameters on fusion zone shape and solidification structure of austenitic stainless steels", *Materials Letters,* vol. 32, pp. 155-163, 1997.

[92] E. Chevallier, "Private Communication", 2016.

[93] N. Ranc, A. Blanche, D. Ryckelynck, and A. Chrysochoos, "POD Preprocessing of IR Thermal Data to Assess Heat Source Distributions", *Experimental Mechanics,* 2014.